Polymer-Coated Iron Oxide Nanoparticles for Medical Imaging

By Suelin Chen

B.S., Biology
Minors in Biomedical Engineering and Music Theory and Composition
Massachusetts Institute of Technology, 2003

M.S., Materials Science and Engineering
Massachusetts Institute of Technology, 2007

Submitted to the Department of Materials Science and Engineering
in Partial Fulfillment of the Requirements for the Degree of

DOCTOR OF PHILOSOPHY IN MATERIALS SCIENCE AND ENGINEERING
at the
MASSACHUSETTS INSTITUTE OF TECHNOLOGY

June 2010

Signature of Author……...
Suelin Chen
May 10, 2010

Certified by……...
Ralph Weissleder, M.D., Ph.D.
Massachusetts General Hospital, Harvard Medical School
Director of the MGH Center for Systems Biology and the Center for Molecular Imaging Research
Thesis Supervisor

Certified by……...
Angela Belcher, Ph.D.
Massachusetts Institute of Technology
Germeshausen Professor of Materials Science and Engineering and Biological Engineering
Thesis Supervisor

Accepted by…….....
Christine Ortiz, Ph.D.
Massachusetts Institute of Technology
Associate Professor of Materials Science and Engineering
Chair, Departmental Committee on Graduate Students

POLYMER-COATED IRON OXIDE NANOPARTICLES FOR MEDICAL IMAGING

by

Suelin Chen

Submitted to the Department of Materials Science and Engineering on Friday, May 21, 2010
in Partial Fulfillment of the Requirements for the Degree of
Doctor of Philosophy in Materials Science and Medical Engineering

ABSTRACT

One of the most versatile and safe materials used in medicine are polymer-coated iron oxide nanoparticles. This dissertation describes several formulations for *in vivo* imaging applications. The paramagnetic polymer-coated iron oxide nanoparticle aminoSPARK is used as a fluorescence-mediated tomography (FMT) imaging agent for stratification of prostate cancer tumors. This is achieved by conjugating it to a peptide that targets SPARC (secreted protein acidic rich in cysteine), a biomarker protein associated with aggressive forms of prostate cancer. Several types of polymer coatings for iron oxide nanoparticles have been systematically explored using a novel high-throughput screening technique to optimize coating chemistries and synthetic conditions to produce nanoparticles with maximum stability and ability to lower T2 contrast for MR imaging (R2, or relaxivity). Carboxymethyl dextran emerged from the screen as an ideal coating for superparamagnetic iron oxide nanoparticles. A commercially available, FDA-approved nanoparticle with similar surface chemistry, Feraheme, was chosen as a platform nanoparticle for further development. This work presents the first instance of chemical modification of Feraheme, making it more amenable to bioconjugation by converting its free carboxy groups to free amine groups. This amine-functionalized Feraheme nanoparticle (amino-FH) is then used as a base nanoparticle to which various targeting and reporting functionalities can be added. A FH-based nanoparticle that can be used for cell loading is synthesized by covalently combining Feraheme with protamine, a pharmaceutical that also acts as a membrane translocating agent. A rhodamine-protamine conjugate is synthesized and then covalently bound to amino-FH using carbodiimide (CDI) chemistry. This results in a magnetofluorescent cell-labeling nanoparticle (ProRho-FH) that is readily taken up by mouse mesenchymal stem cells and U87 glioma cells. ProRho-FH can be used to non-invasively track cells for development and monitoring of cell-based therapies or for further investigation of biological mechanisms such as cell migration, tumor growth, and metastasis. This combination of two FDA-approved, commercially available materials to yield a superparamagnetic and fluorescent cell labeling nanoparticle is an excellent alternative to the recently discontinued Feridex. All polymer-coated iron oxide nanoparticles used in this dissertation were thoroughly characterized to fully understand their physicochemical and magnetic properties.

THESIS SUPERVISORS

Ralph Weissleder, MD, PhD
Massachusetts General Hospital, Harvard Medical School
Director of the MGH Center for Systems Biology and the Center for Molecular Imaging Research

Angela Belcher, PhD
Massachusetts Institute of Technology
Germeshausen Professor of Materials Science and Engineering and Biological Engineering

THESIS COMMITTEE

Ralph Weissleder, MD, PhD
Thesis Supervisor
Massachusetts General Hospital, Harvard Medical School
Director of the MGH Center for Systems Biology and the Center for Molecular Imaging Research

Angela Belcher, PhD
Thesis Supervisor
Massachusetts Institute of Technology
Germeshausen Professor of Materials Science and Engineering and Biological Engineering

Lee Josephson, PhD
Massachusetts General Hospital, Harvard Medical School
Director of Probe Chemistry. Center for Translational Nuclear Medicine and Molecular Imaging

Michael Cima, PhD
Massachusetts Institute of Technology
Sumitomo Electric Industries Professor of Engineering

Alexander Guimaraes, MD, PhD
Massachusetts General Hospital, Harvard Medical School
Assistant Professor of Radiology
Director - Abdominal Imaging, Martinos Center for Biomedical Imaging

Table of Contents

List of Figures

List of Tables

CHAPTER 1: THESIS OVERVIEW

1.1 Thesis Introduction

The blurring of the boundaries between the disciplines of engineering and the biological sciences has revolutionized medicine. Recent advances in domains such as nanotechnology and materials science and engineering have added many new tools for studying biological mechanisms and added many weapons for treatment of disease. Specifically, the development of nanoparticles, which reside at the scale of biological interactions, have allowed researchers to design new ways for materials to interact with the human body. The smallest dimension of nanoparticles is less than about 100 nm, which is comparable to the scale of interaction between cells and molecules in our bodies (Figure 1). Our growing understanding of and ability to manipulate molecules on the nanometer scale has introduced the possibility of interacting on the molecular level with our cells and our bodies with unprecedented control.

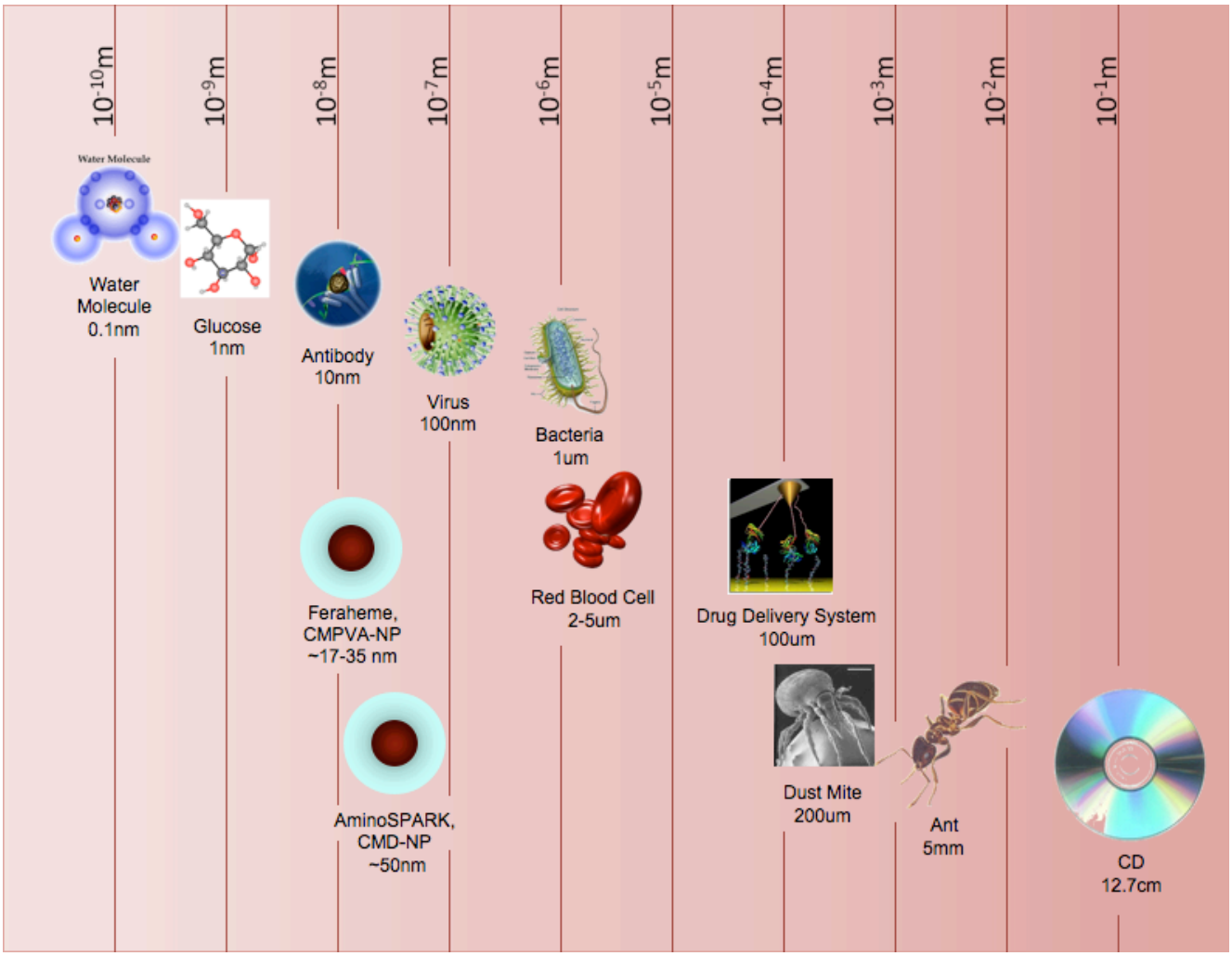

Figure 1. Scale of various nanoparticles and biological entities. The polymer-coated iron oxide nanoparticles discussed in this dissertation, Feraheme, CMPVA-NP, AminoSPARK, and CMD-NP, can range from around 10^{-8} to 10^{-7} nm in diameter.

The extremely small size of nanoparticles gives rise to a variety of properties that larger forms of the same materials would not have. For example, since volume scales as the radius cubed and surface area scales as the radius squared, as the radius shrinks the surface area-to-volume ratio becomes very large. Effects of the considerably augmented surface area include increased chemical reactivity, increased surface free energy, and a variety of other physical,

chemical, and mechanical effects. Additionally, various quantum effects arise at these small length scales since the size of nanomaterials becomes comparable to the de Broglie wavelength ($\lambda = h/p$, where h is Planck's constant and p is the momentum of the particle), effects that are negligible in more conventionally sized materials. Just as some forces become more significant at these length scales, other forces that are important in bulk materials (e.g., gravity) become less important at these scales. The different physical rules that govern nanomaterials give rise to properties that bulk materials do not have, and with our increased understanding we are now able to tune these different properties to achieve a desired effect for a particular application. Although many forms of nanomaterials have applications in medicine, including nanotubes, nanowires, and thin films, this work will focus on nanospheres of zero dimension, which will always be referred to in this dissertation simply as nanoparticles.

Until recently it was necessary to remove tissue for biopsies and probe samples using histology to investigate what was happening in the body, which is not only invasive but time consuming, expensive, labor-intensive, and limited by a finite degree of sampling error. The advent of noninvasive imaging was one of the most valuable technological advances in medicine. Not only can medical imaging provide a means to diagnose disease, it can also allow clinicians to monitor treatment and personalize therapies for each patient. Nanoparticles that are used to enhance and augment imaging technologies have been particularly beneficial and will be the focus of much of this work. Their size allows them to be injected systemically and circulate in the vasculature, as well as enter cells to label and track specific cell types. They can act almost as mobile instruments of seeing, interacting on a molecular level with the body and reporting back to the physician or researcher.

The majority of the material, engineering, and design decisions in this dissertation were based on the goal of creating materials with the possibility of clinical translation. The eventual destination of these materials is within the human body, thus it is necessary to use raw materials and chemical methods that are biocompatible. At times commercially available nanoparticles were used with surface modifications for the particular purpose we had in mind. This strategy allows us to use a material that has been researched, developed, and scaled up, and in the case of an FDA-approved material, rigorously well-characterized and controlled. Not only are these materials valuable because they have passed the high bar set by the FDA for safety, but they are also carefully quality controlled for purity and consistency, making the chemical approaches described here more amenable to reproduction by other researchers. Some nanoparticles used in this study are not suitable for human use, but are important research nanoparticles in that they can be used in vitro and in animal models to further our understanding of various pathologies. It is then a relatively easy jump to take these surface modifications and apply to them to clinically relevant nanoparticles with similar surface chemistries.

Although this work focuses on the applications of these nanoparticles to imaging, many of the new chemistries developed here have yielded nanoparticles that can be used for a variety of other types of applications including cell separation and sensing. In vitro applications of iron oxide nanoparticles such as purification, bioseparation, immunoassays, and sensing in medical devices, are large and active fields of research but are not specifically addressed here.

Below is a table summarizing the polymer-coated iron oxide nanoparticles that are used and/or synthesized in this dissertation, along with their source, their physicochemical properties, and where they appear in the document. General trends emerge which will be discussed later in the dissertation.

Table of Polymer-Coated Iron Oxide Nanoparticles and their Physicochemical Properties

Formu-lation	Source	Hydro-dynamic diameter (nm)	Core diameter (nm)	Core # Fe	R1 ($mmol^{-1} sec^{-1}$)	R2 ($mmol^{-1} sec^{-1}$)	Mag. Sat. (emu/ g Fe)	Zeta Poten-tial (mV)	Type, # Functional Groups/NP	Comment	Chap-ter
aminoSPARK	Visen	54	8.8 ± 2.5	~8,000	n/a	n/a	n/a	-7.15	VT680/VT 750, NH_2	Para-magnetic	Ch. 4
CMD-NP	Synth-esized [1]	47 ± 4.6	18.9 ± 3.8	62,000	16.8 ± 5.8	271 ± 26.3	68	-22 ± 1.1	OH, COOH	Result of screen	Ch. 5
CMPVA-NP	Synth-esized[1]	37.1 ± 1.4	7.2 ± 1.9	8,900	47.3 ± 2.6	119.2 ± 2.4	59	-14 ± 3.3	OH	Result of screen	Ch. 5
Feraheme (feru-moxytol, AMI 228)	AMAG Pharma-ceuticals	17-31^	6.4 ± 0.4*	5,874^	32.4	62.7	23.6[2]	-37.8 ± 3.7	8 COOH	FDA approved 2009	Ch. 6, 7
Amino-FH	Synth-esized	15	6.4 ± 0.4[3]	5,874^	26.2	44.9	nd	-29.6 ± 0.85	8 NH_2	Platform NP	Ch. 6, 7
FH-Cy5.5	Synth-esized	16.6	6.4 ± 0.4[3]	5,874^	23.2	47.8	nd	-16.8 ± 1.3	2.5 Cy5.5	Magneto-fluorescent	Ch. 6
FH-Rho	Synth-esized	16.9	6.4 ± 0.4[3]	5,874^	24.7	55.1	nd	-14.5 ± 1.08	5 Rho	Magneto-fluorescent	Ch. 6, 7
ProRho-FH	Synth-esized	34.3	6.4 ± 0.4[3]	5,874^	20.6	65.2	nd	-0.037 ± 0.84	5 ProRho	Magneto-fluorescent cell labeling NP	Ch. 6, 7
DTPA-CyAl5.5-FH	Synth-esized	14.8	6.4 ± 0.4[3]	5,874^	21.4	35	nd	-21.9 ± 1.65	3.5 DTPA-CyAl5.5	Trifunc-tional NP	Ch. 6
Feridex	AMAG Pharma-ceuticals, (discon-tinued)	120-180	15.2 ± 8.9[4]	~50,000	23.7 ± 1.2[4]	107 ± 11[4]	93.6 ± 1.6[4]	-18.4	OH	No longer available	Ch. 7
Combidex (Sinerem, feru-moxtran, USPIO, AMI-227)	AMAG Pharma-ceuticals	15-30	4.9 ± 1.5[4]	2500–5000	22.7 ± 0.2[4]	53.1 ± 3.3[4]	94.8 ± 0.7[4]	-2	OH	Poly-disperse	n/a
Amino-CLIO	Synth-esized[5]	29.8	4.6 ± 1.0	8,000	23.1	54.9	62	-16	30 NH_2	crosslinked coating	Ch. 5
MION-47	Synth-esized[6]	36.4	4.6 ± 1.2	8,000	22.2	44.5	70	-13.6	OH	non-crosslinked coating	Ch. 5

+aminoSPARK product insert
^Feraheme product insert

Table 1. A list of the polymer-coated iron oxide nanoparticles used in this work, along with reference nanoparticles for comparison. Key physicochemical properties are also listed.

1.2 Thesis Motivations

Iron oxide nanoparticles are one of the few materials injected into the body that are easily incorporated into the body's natural metabolic pathways. They can be synthesized to bind to biocompatible polymers like dextran, allowing them to be coated with various materials that can control their targeting and trafficking in the body. Furthermore, their magnetic properties make them ideal magnetic resonance (MR) contrast agents. There exist other materials that may have stronger magnetic properties or more robust surface properties, but iron oxide nanoparticles have the most desirable combination of safety, biocompatibility, stability, and imaging capabilities combined with a flexible platform for a variety of applications.

This dissertation seeks to investigate several applications of polymer-coated iron oxide nanoparticles, as well as develop new nanoparticle formulations. The application of the nanoparticles range from using them to target specific tumor types to using them to label and track cells. A new type of screening paradigm is also introduced to demonstrate a way to quickly develop new polymer-coated iron oxide nanoparticles that fulfill a variety of design criteria.

The specific goals of this Ph.D. thesis are as follows:

1. Use iron oxide nanoparticles as non – invasive imaging agents for staging prostate cancer
2. Develop a screening method for determining the optimal coating chemistry and synthetic protocol for iron oxide nanoparticles
3. Chemically modify Feraheme so that it is more amenable to bioconjugation and use it as a platform nanoparticle for a variety of imaging applications
4. Develop iron oxide nanoparticles for cell labeling and tracking by MR, using as safe and biocompatible materials as possible

5. Characterize all the nanoparticles used in this dissertation to fully understand their physicochemical properties

1.3 Thesis Organization

The dissertation first gives background on polymer-coated iron oxide nanoparticles, both on how they have historically been used in medical imaging (Chapter 2) and on their material properties (Chapter 3). Considerable attention is paid to the use of these nanoparticles as MR contrast agents and the magnetic properties that make this possible. Prostate cancer and the current clinical challenges surrounding the disease are outlined in section 4.2 and gliomas (a type of brain cancer) are described in section 7.2. The state of the art of medical imaging technologies, including the drawbacks of current technologies and what is needed in future technologies, is described in section 2.2.

Several different polymer-coated iron oxide nanoparticles are used in a optical and magnetic imaging modalities. Two of the nanoparticles are commercially available (aminoSPARK and Feraheme), but have been chemically modified to achieve a specific function. The other polymer-coated iron oxide nanoparticle (CMD-NP) is a novel material developed with specific parameters for clinical translation in mind.

The projects described in this dissertation also have different goals and focuses. The project in Chapter 4 describes an injectable imaging agent developed for diagnosis and prognosis of cancer. Next, in Chapter 5, a clinically relevant polymer-coated iron oxide nanoparticle is developed based on a screening paradigm that seeks to maximize stability and potency. Chapter 6 describes a chemical strategy for modifying the commercially available FDA-approved

nanoparticle Feraheme, transforming it into a versatile platform nanoparticle, after which it is modified for use as a cell tracking agent. Finally, Feraheme was combined with the commercially available drug protamine to label cells, an important function for the development of therapies that use cells and for deeper investigations of the biological mechanisms of various phenomena involving cell migration (e.g., metastasis).

Chapter 4 describes a project using polymer-coated iron oxide nanoparticles to image a prostate cancer biomarker called secreted protein acidic rich in cysteine (SPARC). The nanoparticle is called aminoSPARK and is commercially available.

Chapter 5 describes a new screening paradigm for developing polymer-coated iron oxide nanoparticles. Techniques were developed for screening a large number of polymer coatings and synthetic strategies to optimize specific parameters for the nanoparticles. Two new nanoparticle platforms were developed from this work, one coated with carboxymethyl dextran (CMD) and one coated with carboxymethyl polyvinyl alcohol (CMPVA). The optimal coating CMD is similar in surface chemistry to Feraheme, a commercially available, FDA-approved pharmaceutical. The benefits of using an approved drug for further work were evident and further research was continued using Feraheme.

Chapter 6 describes the chemical modification of Feraheme, the carboxymethyl dextran-coated nanoparticle similar to the one developed in Chapter 5. This project begins by describing a way to make an amino-functionalized version of Feraheme, useful for a variety of bioconjugation strategies. One possible application of a modified Feraheme is described in Chapter 7, where a protamine-functionalized version of Feraheme is developed for use as a cell labeling agent. The protamine has first been conjugated to rhodamine, greatly facilitating in vitro characterization of this material. This cell labeling agent readily enters cells and allows

cells to be tracked and imaged *in vivo* and *in vitro* by fluorescence, iron content, and MR imaging.

Recommendations for a continuation of this line of work along with potential drawbacks are described in Chapter 8 and the dissertation is summarized in Chapter 9. Chapter 10 contains the references for this work, followed by the acknowledgments to all the people that made this work possible.

CHAPTER 2: INTRODUCTION TO THE ROLE OF POLYMER-COATED IRON OXIDE NANOPARTICLES IN MEDICAL IMAGING

2.1 Iron Oxide Nanoparticles in Medicine

Magnetic materials have been used in biology for a variety of applications such as cell sorting and tracking,[7] drug delivery,[8] sensing[9] and imaging.[10] Metals such as cobalt and nickel are highly magnetic but also toxic,[11, 12] limiting their use in biomedical applications. Iron oxides, on the other hand, have a long history of safe clinical use.

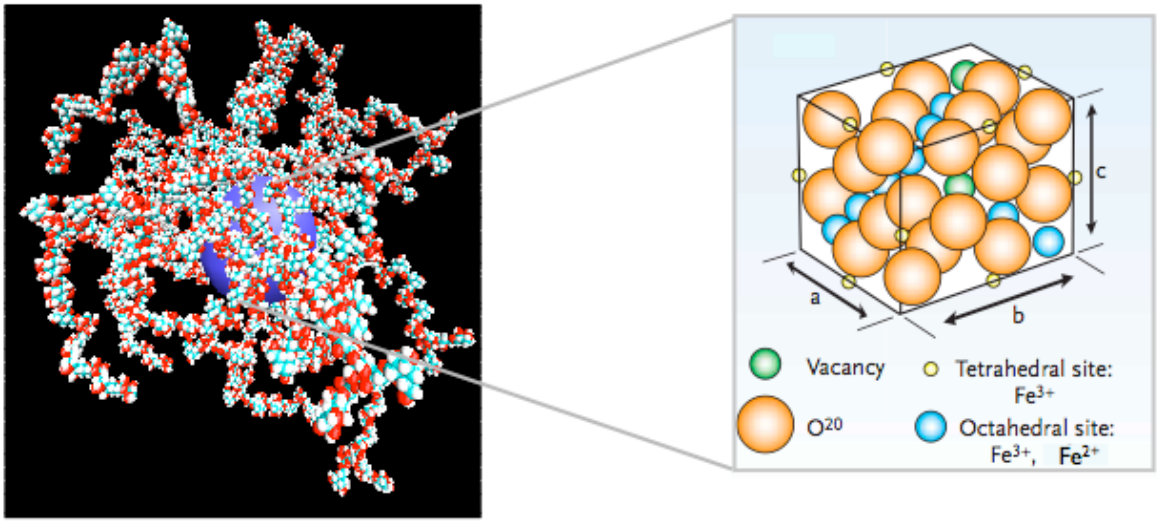

Figure 2. Schematic of polymer-coated iron oxide nanoparticles. Left: polymer-coated iron oxide nanoparticle. The polymer coating is generally significantly larger than the iron core (blue). Right: crystal structure of iron oxide core generally consists of magnetite Fe_3O_4 and maghemite Fe_2O_3. Adapted from reference 13.

Polymer-coated iron oxide nanoparticles (Figure 2) have long been used in an injectable form to treat iron anemia, a relatively common deficiency that can be caused by a variety of factors including blood loss, nutritional deficiencies, and difficulties with iron absorption. Iron is needed by the body to produce hemoglobin, the protein that carries oxygen in the blood. Some examples of paramagnetic dextran-coated iron oxide nanoparticles used to treat anemia are INFeD (Watson Pharmaceuticals) and Dexferrum (Luitpold Pharmaceuticals). Recently Feraheme (a.k.a. ferumoxytol, AMAG pharmaceuticals) was approved to treat anemia, although this nanoparticle is superparamagnetic and thus can be used as an MR contrast agent as well (see Chapters 6 and 7).

Another important medical application of polymer-coated iron oxide nanoparticles is as imaging agents in a variety of contexts. Their coating allows for conjugation of functional ligands, including fluorophores for fluorescent imaging and radioactive ions for PET imaging.

Superparamagnetic iron oxide nanoparticles have the ability to lower the T2 contrast signal for MR imaging and have been used to target phagocytic cells as well as molecular targets *in vivo*. They can also be used to load cells for tracking in order to develop cell-based therapies. One of the most effective ways to follow migration of the cells *in vivo* is using MR imaging, which is noninvasive and has no significant toxic effects. (The use of the iron oxide nanoparticle Feraheme to label and track cells is described in Chapter 7). Some examples of FDA-approved iron oxide nanoparticle MR imaging agents are Feridex IV (formerly supplied by AMAG Pharmaceuticals, recently discontinued) and Resovist (a.k.a. ferucarbotran, Bayer Schering Pharma AG).

Imaging agents are successful if enough of them accumulate at their intended target to provide a robust signal. The emphasis on imaging agents is on their non-toxicity and lack of interaction with regions of the body other than their intended target. On the other hand, therapeutic agents in general must either deliver a load of therapeutic agent or must themselves have therapeutic effects. More often than not these effects are toxic to normal tissue as well, so it is essential to fall within the optimal therapeutic window: low enough in toxicity to result in minimal damage to surrounding tissue, yet toxic enough to eradicate the intended target. With these design parameters in mind, a therapeutic iron oxide nanoparticle can be created.

Superparamagnetic nanoparticles themselves can be used as therapeutic agents by using their hyperthermic qualities to kill cells. They can be heated by an external alternating magnetic field, yielding cell death at temperatures above 41-42˚C. Hyperthermia has been used to target nanoparticles to tumor cells and kill them,[14, 15] an attractive option since many types of cancer cells are more sensitive to high temperatures than normal cells. Another therapeutic strategy using polymer-coated iron oxide nanoparticles was developed by McCarthy et al.; these

researchers created theranostic (therapeutic and diagnostic) nanoparticles that are conjugated to potent photosensitizers for photodynamic therapy.[16] Magnetic nanoparticles can also be used as vehicles for delivering therapeutic agents.[17] Often the nanoparticle will be multifunctional, containing ligands for targeting as well as therapeutic drugs. Targeting allows for more focused delivery of the payload, resulting in less drug needed to fall into the therapeutic window, and thus to less toxic side effects. It is important to note that unlike for imaging agents, when designing a therapeutic agent, biomarkers for a specific pathology that also happen to be expressed in other tissues or organs should be avoided as a target molecule since the toxicity would then reach those parts of the body.

The use of magnetic nanoparticles in biology and medicine will improve our understanding of biological processes at the nanoscale, and will also improve our ability to diagnose and treat disease. Although iron oxide nanoparticles have a long history of different types of uses in medicine and are actively being developed for a variety of applications today, this dissertation will focus on their development for use in the field of medical imaging.

2.2 Background on Medical Imaging Technologies

The ability to non-invasively investigate what is happening in the body is extremely useful for diagnosing pathologies, monitoring treatments, and providing guidance to more invasive treatments like surgery. As mentioned in the previous section, iron oxide nanoparticles have been used to augment many of the imaging modalities described below. This section is not meant to be an exhaustive review of medical imaging, only to give an idea of some of the different imaging technologies that can benefit from nanoparticle contrast agents.

2.2.1 Radionuclide Imaging

Single photon emission computed tomography (SPECT) uses a gamma camera to capture gamma rays emitting from radionuclides that have been injected into the body. Multiple 2-D images are acquired and then stitched together by a computer to form a 3-D image. Positron emission tomography (PET) is a similar imaging technique in that it detects radioactive tracer isotopes that have been injected into the body, but unlike SPECT, which measures gamma ray radiation directly, PET measures the two gamma photons emitted when an emitted positron annihilates with an electron. As there are two coincident emissions, PET is able to construct higher spatial resolution images (as low as $\sim 3^3$ mm^3) than SPECT, with a sensitivity of about 10^{-11}–10^{-12} mole/L whereas SPECT has a sensitivity about an order of magnitude below that. However, SPECT is less expensive than PET, partly because the radioisotopes used are less expensive and have longer half-lives.

The use of PET is limited by its tracers, which are expensive not only due to the high costs associated with the cyclotrons required to make them, but their generally short half-lives require them to be made close to the site of administration and restrict the window of time in which a scan can be made. For this reason it is common to use tracers with relatively longer half lives such as fluorine-18 (F-18), which has a half-life of 118 minutes. One of the most common molecules used for PET imaging is fluorodeoxyglucose (FDG), an analogue of glucose that the body can use as an energy source, allowing visualization of metabolic activity. PET scanning using FDG is widely used in oncological applications to diagnose and monitor treatment of tumors, since tumors often metabolize FDG differently than normal tissue. PET is also used extensively for a variety of other applications, including in pharmacology to determine the

biodistribution of new drugs. One major drawback to the use of PET is the risk associated with the use of the radioactive tracers, which exposes the subject to ionizing radiation. This risk limits the possibility of performing longitudinal studies.

2.2.2 Computed Tomography (CT) Imaging

Computed tomography (CT), which has also been known as body section röntenography and the computed axial tomography (CAT) scan, uses digital processing to construct a three-dimensional image from many two-dimensional X-ray images that have been taken around one axis of rotation. This type of imaging is used in all areas of the body to assess and diagnose a variety of pathologies, including cancer, physical injuries and trauma, bood clots and other obstructions, and inflammation. Resolution of standard medical CT instruments is on the order of 1-2 mm. The recent popularity of full-body CT has associated risks, including exposure to radiation, and there have been many studies linking exposure to CT radiation with cancer. Contrast agents such as intravenous iodine are sometimes used to highlight the vasculature, but there are documented risks from these types of contrast agents as well.

2.2.3 Optical Imaging

Bioluminescence imaging (BLI) capitalizes on the inherent capabilities of certain organisms to bioluminesce by taking the portion of the DNA encoding the luminescent protein and inserting it into the DNA of the test subject. Several reporters have been used including firefly and renilla luciferases, both of which require an injection of substrate (D-luciferin and coelenterazine, respectively) prior to imaging. The small amount of light emitted is detected by a CCD camera which is extremely sensitive but which is still limited to just several centimeters of tissue due to attenuation, making this technique most applicable to small animal imaging.

Mammalian tissues have a low background of intrinsic bioluminescence, advantageous for achieving decent signal-to-noise ratios with BLI.

Fluorescence-Mediated Tomography (FMT) is a proprietary imaging system of VisEn that can detect near-infrared probes *in vivo* in deep tissues using its tomographic reconstruction and sophisticated algorithmic models, an improvement over traditional optical imaging techniques. Although FMT is not a clinically relevant imaging modality, it is an extremely valuable, relatively low-cost research tool for imaging small animals. Despite the limitations of optical imaging methods for humans due to the small path length of light, there is much to be gained from using these imaging methods in the study of small animal models.

2.2.4 Magnetic Resonance Imaging (MRI)

Magnetic Resonance Imaging, also known as nuclear magnetic resonance imaging, is the most powerful imaging technique for visualizing soft tissue detail in the body and provides the highest resolution (sub micron) of any other imaging modality. Compared with optical imaging techniques, it has excellent tissue penetration depth, which is important when visualizing a human being as opposed to a small animal. A powerful magnet, usually a superconducting magnet, is used to generate extremely high magnetic fields in the imaging subject. In the clinic magnets between 0.5-2 tesla are used, though magnets as strong as 60 tesla are used in research. Living tissue is largely comprised of water molecules, each of which contain two hydrogen nuclei that have large magnetic moments. Normally the magnetic moments are randomly aligned and cancel each other out, but in the homogenous magnetic field of the MR scanner some of the magnetic moments align, producing a net magnetic moment. A radiofrequency (RF) pulse is initiated by the scanner and absorbed by the hydrogen protons, causing them to precess

in a different direction at a frequency known as the Larmor frequency, which is proportional to the magnetic field. Once the magnetic field is turned off the proton spins relax to their unexcited state and release a photon, which is detected and transformed into an image. The physics of this relaxation process is described in more detail in Section 2.3.

MRI has comparable resolution to CT and much better contrast, but the major advantage of MRI is its safety. Excluding metal implants in the body, MRI is an extremely safe procedure as there are no known negative effects to being exposed to a high magnetic field. Unlike PET and CT, there is no need to expose the subject to ionizing radiation and thus there is not an increased risk associated with multiple scans.

Since each imaging modality has its advantages and disadvantages, naturally there is a significant amount of effort to combine one or more of these medical imaging modalities, capitalizing on the strengths of each and complementing the weaknesses. The combinations of SPECT-CT, PET-CT and PET-MRI are being increasingly used and refined. One of the difficulties of achieving a successful combination is the different time scales of acquisition for each modality and the co-registration of the images. Nevertheless, it is a promising area of research where iron oxide nanoparticles could greatly contribute, in part because of their potential for multifunctionality.

The imaging modalities described above have drastically improved our ability to non-invasively gain an understanding of what is happening inside the body. Until recently, these imaging technologies were only able to show reveal physiological information such as tumor size and anatomical location. The advent of molecular imaging has made it possible to probe more specific parameters of disease, including the presence of growth factors, molecular

abnormalities and tumor biomarkers. Molecular imaging is also revolutionizing how drugs and other treatments are evaluated, as well as facilitating basic research on the biological mechanisms of disease. Nanoparticles are often the platform material for these targeted imaging agents and in doing this they have given us unprecedented access to the molecular life of the body. Nanoparticles can also be used to label materials that are transplanted into the body, such as cells, so that they can be tracked non-invasively.

2.3 Iron Oxide Nanoparticles used as Imaging Contrast Agents

Polymer-coated iron oxide nanoparticles can be used as imaging contrast agents for many of the different imaging modalities presented above either by conjugating imaging moieties to the surface of the particle or using the inherent properties of the nanoparticle. For example, various optically active molecules can be conjugated to iron oxide nanoparticles for use in optical imaging. AminoSPARK nanoparticles have near-infrared fluorochrome tags VT680 or VT750 covalently bound to their coating, allowing them to be visualized by FMT. PET-imageable radioisotopes can be conjugated to iron oxide nanoparticles via chelation agents such as DOTA (1,4,7,10-tetraazacyclododecane-1,4,7,10-tetraacetic acid) and DTPA (Diethylene triamine pentaacetic acid).

However, the most common use of iron oxide nanoparticles in medical imaging is as MR contrast agents because the iron oxide core can have a structure that is superparamagnetic, allowing them to be visualized using MRI. Without contrast agents MR imaging can already discern between different types of soft tissue and provide a great deal of information, and indeed the majority of MRI scans are completed without contrast agents. However, an increasing number of scans are enhanced by the use of contrast agents, which can greatly improve the

visualization of various tissues as well as highlight specific areas, such as a tumor or other pathology.

MR contrast agents can be categorized into agents that alter the T1 relaxation time and agents that alter the T2 relaxation time. Both of these types of agents change the MR signal but the have different physical mechanisms of action. When an external field B is applied along the z axis, the nuclear spin magnetization vector M recovers towards its equilibrium value M_{eq}. The decay constant of M_z (the parallel component of M) is known as T1, and describes the energy transfer from the proton to other materials (e.g., the 'lattice' or dispersant), while the decay constant of M_{xy} (the perpendicular component of M) is known as T2, which describes the dephasing of the spin due to the magnetic field inhomogeneities. The equations below show that the T1 is the time it takes for the signal to recover approximately 63% (1-1/e) of its original value while the T2 is the time it takes for the signal to recover approximately 37% (1/e) of its initial value:

$$M_z(t) = M_{z,eq}(1\text{-}e^{-T/T1})$$

$$M_{xy}(t) = M_{xy,eq}(0)e^{-T/T2}$$

The T1 relaxation time is also known as the spin-lattice or longitudinal relaxation time, and the T2 relaxation time is also known as the spin-spin or transverse relaxation time.

Contrast agents that affect the T1 generally cause an increased amount of T1 signal and thus are known as positive contrast agents (regions with these agents become hyperintense). The most commonly used T1 agent is based on gadolinium (Gd), a paramagnetic element that is injected as an IV contrast agent. There are several FDA-approved gadolinium-based agents including Magnevist (Bayer Schering Pharma) which is Gd complexed with DTPA. Although

gadolinium is considered toxic as a free ion, when it is chelated it is considered to be safe. Nevertheless, some gadolinium manages to be liberated, causing many significant safety concerns, including nephrogenic systemic fibrosis/nephrogenic fibrosing dermopathy (NSF/NFD), which affects connective tissues throughout the body. Many iron oxide nanoparticles can also affect the T1 signal, but generally to a lesser degree than the T2 signal.[18, 19]

Contrast agents that affect the T2 reduce the T2 and T2* signal and are known as negative contrast agents (regions with these agents become hypointense). Superparamagnetic iron oxide nanoparticles are the most common class of contrast agents that affect the T2. FDA-approved superparamagnetic iron oxide contrast agents include Combidex and Feridex (Endorem) by Advanced Magnetics (Feridex was recently discontinued). Unlike gadolinium, iron oxide nanoparticles have little known toxic effects. The physical basis behind T2 MR contrast agents will be discussed in more detail in Chapter 3.

2.4 Biocompatibility and Toxicology of Iron Oxide Nanoparticles

One of the key advantages of using iron oxide nanoparticles as imaging agents and in other biomedical applications is their relative lack of toxicity.[20, 21] Although different iron oxide nanoparticles have different fates in the body depending on the particular chemical composition of their coating and core, standard toxicological and pharmacological tests have shown iron oxides to be one of the safest materials used in human beings.

The immune system employs a series of methods to clear foreign entities from the circulation, which can be problematic when trying to engineer a long-circulating nanoparticle.

The reticulo-endothelial system (RES, also known as the mononuclear phagocyte system or MPS) is an entire family of cells that work together and include tissue macrophages, blood monocytes, and bone marrow progenitors. When the system recognizes a material as foreign the first thing that happens is that opsonins, plasma proteins in the circulation known as complement proteins, spontaneously adsorb to the surface of the foreign body, marking it as foreign. These opsonins have essentially tagged the foreign material for phagocytic cells like monocytes and macrophages to recognize as something that needs to be cleared. The pattern of opsonin adsorption, which is dependent on factors like nanoparticle size and surface chemistry, [22, 23] determines the pattern of clearance of the nanoparticle. Eventually the phagocytic cells accumulate in organs such as the liver (e.g. in Küpffer cells) and other macrophage-rich organs, ultimately determining the biodistribution of iron oxides injected into the body.

In the case of dextran-coated iron oxide nanoparticles, the dextran is degraded by intracellular dextranases and then eliminated in the urine.[24] Other biodegradable polymer coatings have similar fates. The iron from the nanoparticles enters the body's natural iron metabolic system, is sequestered in the iron storage protein ferritin and eventually ends up in the hemoglobin in red blood cells.[25] Although iron is an essential nutrient, it can be toxic in some situations, but generally only when very large amounts of elemental iron have been ingested.[26] It is also possible for some individuals to have an adverse immune reaction to the coating. Some people possess anti-dextran antibodies that can cause severe allergic reactions to dextran injections, which have historically been used in the clinic as a plasma expander. It is thus possible that nanoparticles coated with these types of polymers could thus potentially induce a similar reaction.

Although it is not always straightforward to engineer the perfect coating for the particular function of the nanoparticle, some trends do emerge. Charged dextrans such as carboxymethyl dextrans tend to have shorter blood half-lives.[10] Other factors such as nanoparticle size are also important in determining the fate of the nanoparticles in the body, but the coating choice is a major determinant of trafficking *in vivo*. If the target location of the nanoparticle is not within a phagocytic cell, a different type of coating must be devised to essentially camouflage the nanoparticle from the RES system. There are many strategies to avoiding the complement activation system and there are many complex factors interacting with each other that effect clearance time, but in general, long-circulating nanoparticles tend to be small in size, less charged, and more hydrophilic. Aspect ratio may also play a role, and some researchers have altered trafficking by using high aspect ratio shapes like tubes, but this parameter is not explored here.

CHAPTER 3: MATERIAL PROPERTIES AND CHARACTERIZATION OF IRON OXIDE NANOPARTICLES

3.1 Structure and Forms

Iron oxide nanoparticles are generally one or both of magnetite (also known as iron(II,III) oxide, Fe_3O_4) and maghemite (also known as iron(III) oxide, γ-Fe_2O_3). Although the magnetic properties of these two forms are different the crystal structures are very similar, basically consisting of a cubic inverse spinel structure with oxygen atoms in an fcc lattice and Fe cations occupying interstitial tetrahedral and octahedral sties.[6] Maghemite is essentially a Fe(II)-deficient magnetite and is formed by oxidation of magnetite. The equations for these two forms of iron oxide are given by:

$$Fe_3O_4:\ [Fe^{3+}]_{Th}[Fe^{3+}Fe^{2+}]_{Oh}O_4$$

$$\gamma\text{-}Fe_2O_3:\ 0.75[Fe^{3+}]_{Th}[Fe^{3+}{}_{5/3}\ V_{1/3}]_{Oh}O_4$$

where Th denotes the tetrahedral sites of the spinel structure and Oh denotes the octahedral sites.

Although the addition of other types of metal ions (e.g. Co, Ni) to iron oxides (i.e., doping) can increase the potency of the nanoparticle in terms of its ability to lower the T2, both Co and Ni are susceptible to oxidation and have exhibited toxic properties. Only iron oxide alone has a proven history of safe and non-toxic use in vivo, thus this dissertation will focus on the possibilities of iron oxides without additives.

Some reviews choose to categorize the different formulations of nanoparticles by hydrodynamic size:[10] nanoparticles that fall between 50-180 nm are the known as superparamagnetic iron oxide nanoparticles (SPIOs), nanoparticles that are 10-50 nm in diameter are known as ultrasmall superparamagnetic iron oxide nanoparticles (USPIOs), and nanoparticles smaller than 10nm in diameter are known as very small superparamagnetic iron oxide nanoparticles (VSPIOs). In this work we will not make this kind of distinction because although size is a an important characteristic of nanoparticles, many other properties such as core structure and coating chemistry are equally if not more important, thus categorizing iron oxide nanoparticles by hydrodynamic size is considered by the author to be a somewhat arbitrary distinction. Instead nanoparticles will be considered individually in this dissertation, based primarily on core composition and coating type.

3.2 Synthesis

There are several synthetic strategies to making polymer-coated iron oxide nanoparticles including thermal decomposition and/or reduction, micelle synthesis, hydrothermal synthesis, and biosynthesis.[27-30] In general it is desirable for the synthetic process to be scaleable to an

industrial size, be reproducible from batch to batch, and result in relatively monodisperse nanoparticles. The synthesis and preparation of these nanoparticles in large part determine the size, shape, and the degree of impurities and structural defects. All of these factors can affect the magnetic behavior, which for MR contrast agents determines their potency and sensitivity. The monodispersity of a nanoparticle preparation is also important, as monodisperse preparations are easier to characterize, are more likely to win FDA approval, and have more easily controllable properties. The use of a surfactant during synthesis can improve the monodispersity of the nanoparticles, but the difficulty in fully removing the surfactant and the problems arising from potential toxicity have yet to be fully investigated.

The nanoparticles used in this dissertation have been synthesized using a coprecipitation method whether they were synthesized in-house or purchased from a supplier, so this relatively simple and scaleable synthetic reaction will be described here in more detail. In a general coprecipitation reaction, stoichiometric amounts of ferric and ferrous chlorides are mixed in aqueous media in the presence of ammonia and the coating polymer, yielding homogenous spherical magnetite particles. Homogenous nucleation occurs when there is a critical supersaturation of nanoparticle starting material, which is achieved by slowly increasing the pH of the solution. The nanoparticles grow when solutes in the solution diffuse to their surface, with complete precipitation of Fe_3O_4 occuring between pH 9 and 14. During this period of growth it is best to avoid nucleation to achieve monodispersity. The polymer used to coat the nanoparticles can be a starch-derivative such as dextran or carboxymethyl dextran (CMD) or another kind of polymer such as carboxymethyl polyvinyl alcohol (CMPVA). Many of the coating options are investigated in Chapter 5. During synthesis the polymer forms a swollen three-dimensional scaffold, preventing aggregation of the nucleated iron particles.

Two forces compete to determine the size of the resulting nanoparticle: the surface energy and entropy. The polymer that is added to the reaction vessel chelates the iron, lowering the surface tension and allowing smaller nanoparticles to stabilize. The reaction can be written as

$$Fe^{2+} + 2\,Fe^{3+} + 8\,OH^- \rightarrow Fe_3O_4 + 4H_2O$$

Some of the magnetite (Fe_3O_4) tends to oxidize and form maghemite (y-Fe_2O_3):

$$Fe_3O_4 + 2\,H^+ \rightarrow y\text{-}Fe_2O_3 + Fe^{2+} + H_2O$$

This process of oxidation is sensitive to the pH of the suspension. Various other parameters of the reaction can be tuned to control size, crystallinity, and composition including the ferric/ferrous ratio, the polymer/Fe ratio, the ionic strength of the solution, the temperature, and the addition of salts.

The resulting nanoparticles have a core made of a combination of magnetite (Fe_3O_4) and maghemite (y-Fe_2O_3). The dextran or other polymer coating has a hydrogen bonding interaction with the iron which keeps the nanoparticle fairly stable due to the length of the polymer and the large number of hydrogen bonds formed; however, dextran coatings can at times become dissociated from the nanoparticle. For this reason cross-linking has been used to stabilize the polymer coating to yield a cross-linked iron oxide (CLIO) nanoparticle. Carboxylating the dextran can also improve stability without crosslinking by strengthening the association between the polymer and the iron oxide core. Nanoparticle coatings are discussed in more detail in section 3.4.

3.3 Physical and Chemical Properties

It is important to understand the physicochemical properties of the nanoparticles not only because these properties determine their stability, quality and reproducibility of production, and efficacy as MR contrast agents, but because fully characterizing these nanoparticles is the best way to understand how they will behave in the body. Both the size and surface chemistry of the nanoparticle will affect the pharmacokinetics and in vivo trafficking of the nanoparticle and being able to control these parameters is critical for developing an effective imaging agent. Many characterization techniques can be used and each of these can give a variety of types of information. This section is ordered around the types of properties that can be investigated, and will mainly focus on techniques employed in this dissertation.

3.3.1 Size (Core and Hydrodynamic)

The size of nanoparticles is crucial to their function. The balance of forces determining colloidal stability is dependent on the dimensions of the nanoparticle, since smaller sizes prevent gravitation forces from being significant enough to cause precipitation. Also, the high surface area-to-volume ratio of nanomaterials enhances the effect of ligands attached to the nanoparticle surface. The small size of nanoparticles also tends to increase diffusion in the body and increase blood half-life. Importantly, nanoparticles are on the same size scale as the biological interactions that govern our bodies, making them ideal candidates as probes of biological function. Their magnetic properties are also size-dependent: magnetization relaxation goes as KV/kT, where K is the particle anisotropy constant, k is Boltzmann's constant, T is temperature, and V is the volume of the particle.[31] The magnetic phenomenon of superparamagnetism,

essential for T2 contrast agents (see section 2.3), occurs when KV becomes comparable to thermal energy *k*T.

One way to determine the size of the iron core of the nanoparticles, is by using transmission electron microscopy (TEM) since the polymer coating is more transparent to the electron beam.[32] TEM can give information on the size of the core, the polydispersity of the nanoparticle population, as well as an idea of the type of shapes formed by the nanoparticles. This microscopy technique functions by recording the interaction of an electron beam through a material with a CCD camera. TEM has much improved resolution compared with optical methods because of the small de Broglie wavelength of electrons as compared with the wavelength of light, allowing even atomic structure to be discerned. Core size can also be measured using small-angle X-ray scattering (SAXS),[33,34] laser-desorption ionization mass spectroscopy,[35] and X-ray diffraction (XRD), where core diameter is inversely proportional to crystalline peak width.[36]

Dynamic Light Scattering (DLS) is a technique used to determine the hydrodynamic size of particles in solution. A light source, generally a laser in the case of DLS, shines on the particle solution and as long as the particles are smaller than the wavelength of light (< ~250 nm) they will scatter light in all directions uniformly, a phenomenon called Rayleigh scattering. Thermal energy causes the particles to constantly undergo Brownian motion so that with a monochromatic and coherent light source like a laser there is a time-dependent fluctuation in the distance between particles. Various mathematical approaches can then be used to arrive at the diffusion coefficient of the particles. Knowing the diffusion coefficient D and the viscosity of the dispersant η, it is possible to determine the size (r, for radius) of the particles using the Stokes-Einstein equation:

$$D = \frac{k_B T}{8\pi\eta r}$$

where k_B is Boltzmann's constant and T is temperature. Scanning tunneling microscopy (STM) and atomic force microscopy (AFM) can also be used to determine the size of the nanoparticle.[37,38]

A method of determining the nanoparticle core weight or number of iron atoms per core by using the viscosity of a nanoparticle suspension has been described previously (referred to as the viscosity/light scattering method or VLS).[39] In this approach viscosity measurements of a nanoparticle suspension are used to determine the nanoparticle volume fraction, which is then divided by the average volume of a nanoparticle obtained by DLS. The weight of one nanoparticle can then be calculated by dividing the iron concentration by the number of nanoparticles per volume. Once the weight and composition of the core are known, it is possible to estimate the number of atoms in the core.

3.3.2 Surface Properties

Atomic force microscopy (AFM) is a scanning probe microscopy technique that uses a cantilevered probe with a nanoscale radius of curvature to raster across a surface, drawing a map of the surface. Nanoparticles can be immobilized to an atomically flat surface like flame-annealed gold and their surface morphology can be determined. Depending on the sample and the functionality of the tip, the AFM can be used to determine mechanical forces, van der Waals forces, and electrochemical forces, of the sample. Scanning Tunneling Microscopy (STM) can be used to image materials with atomic resolution and map electrical properties.

Nanoparticles in solution are colloidal suspensions and thus their surface zeta potential is one of the main determinants of stability in solution. The balance between the van der Waals attractive force and the electrical double layer repulsive force governs whether the nanoparticles will flocculate or remain dispersed. The steric repulsion of the polymer coatings of the nanoparticles discussed in this work is one major factor in keeping the van der Waals attractive forces low, but surface charge is also an important parameter. The potential at the electrical double layer can be measured using the electrophoretic mobility of the nanoparticles, which essentially measures the velocity of the nanoparticles as they move between two electrodes in response to an applied electrical potential. Naturally zeta potential is extremely sensitive to the pH and ionic strength of the dispersant so great care must be made to keep those parameters consistent across measurements. The zeta potential can give an idea of stability as well as a qualitative idea of surface functional groups.

3.3.3 Composition

One way to investigate the arrangement and type of atoms in a crystal is to use X-ray diffraction. When bombarded by X-rays, the atoms in a crystal scatter the electromagnetic radiation in a way that is characteristic of the arrangement and type of atoms. The conditions required for diffraction are described by Bragg's Law

$$\lambda = 2d_{hkl}\sin\theta$$

where λ is the wavelength of the X-rays, d_{hkl} denotes the space between planes (this parameter determines peak positions), and θ indicates the angle that the diffracted and incident beams make with the (*hkl*) planes. The position, intensity, width, and shape of the diffraction peaks are

characteristic of the material of the sample, and can be determined by comparing the sample's profile with reference patterns in known databases. XRD can also be used to determine the unit cell lattice parameters, the phase composition, the amount of residual strain or macrostrain, the amount of microstrain, and the crystallite size (see section 3.3.1) of a given sample.

Energy dispersive X-ray spectroscopy (EDS or EDX) can be used for elemental analysis of a sample, and it is often coupled with an electron microscope. A high-energy beam of charged particles (not necessarily X-rays) bombards the sample and number and energy of the emitted X-rays, which are characteristic of the energy difference between the electron shells around the nucleus, can be used to determine the elemental composition of the sample.

Mass spectrometry can also be used to assess nanoparticle composition, but is used in this dissertation to confirm the synthetic product of a conjugation reaction for a nanoparticle ligand (Chapter 7). In this technique the sample is ionized by an energy source such as an electron beam. The ions are then accelerated in an electric field and the mass-to-charge ratio is determined from their motion to the other side. The mass spectrometric signature of the sample can then be used to determine the composition.

3.4 Iron Oxide Nanoparticle Coatings

The surface of the nanoparticle is what the body interacts with first and is thus crucial in determining the fate of the nanoparticle. Bare iron oxide nanoparticles tend to be problematic because they are insoluble in water, causing agglomeration and precipitation. In order to stabilize the nanoparticles a coating that uses electrostatic and/or steric repulsion to limit nanoparticles' attraction to each other either is necessary. Another issue with uncoated iron oxide nanoparticles is their immunoreactivity, causing activation of the complement system as

described in section 2.5 and leading to the nanoparticles being prematurely cleared from circulation. For these reasons most nanoparticles injected in vivo have some sort of coating that serves to avoid premature clearance, render the nanoparticles water-soluble, protect particle surfaces from oxidation, and improve biocompatibility. A diverse range of materials have been used for coatings, including lipids,[40] dendrimers,[41] proteins,[42] carbohydrates such as starch,[43] and various other polymers such as polyethylene glycol (PEG)[44] and polyacrylamide.[45] Clinical preparations of iron oxide nanoparticles have almost exclusively used dextran and its derivitatives because they have already been used clinically as plasma expanders (their attachment to drugs can increase a drug's circulation time) and because they have an intrinsic affinity for iron oxides.[46] Coatings can also provide chemical entrance points for conjugation of imaging, targeting, and other functional modalities. The magnetic properties that allow nanoparticles to serve as effective MRI contrast agents are still due to the iron oxide core, while targeting, optical imaging, and most of the interactions with biological systems are functions of the nanoparticle coating.

Many iron oxide nanoparticles take advantage of the fact that macrophages and monocytes are designated to engulf foreign bodies, and are likely to take them up. Ferumoxides (Endorem®, Feridex) and ferucarbotran (Resovist®) are two types of dextran-coated iron oxide nanoparticle preparations that have been approved for intravenous use, mainly for imaging of liver lesions and tumors. However, these "blood pool" (as opposed to targeted) nanoparticles only accumulate due to differences in endocytotic uptake and/or tissue composition, and are not molecularly targeted in any way.[47] Furthermore, their synthetic protocol yields polydisperse populations, making them more difficult to characterize and giving them shorter half lives.

The monodisperse iron oxide nanoparticle (MION) class of nanoparticles, which includes Combidex, has been shown to improve the ability of MRI to detect lymph node metastases.[13] Other applications of these nanoparticles include the imaging of angiogenesis,[48] inflammatory cells in atherosclerotic plaques,[49] and primary tumors for better border definition.[50] However, MIONs are not easily functionalized and the polymer coating is not very stable in physiological conditions. One way to improve stability is to cage the dextran coating using epichlorohydrin to yield a cross-linked iron oxide nanoparticle (CLIO). This cross-linked polymer coating works well for adding functional groups and for stability, and CLIO has enjoyed great success as an experimental platform. However, it cannot biodegrade and thus is not clinically translatable.

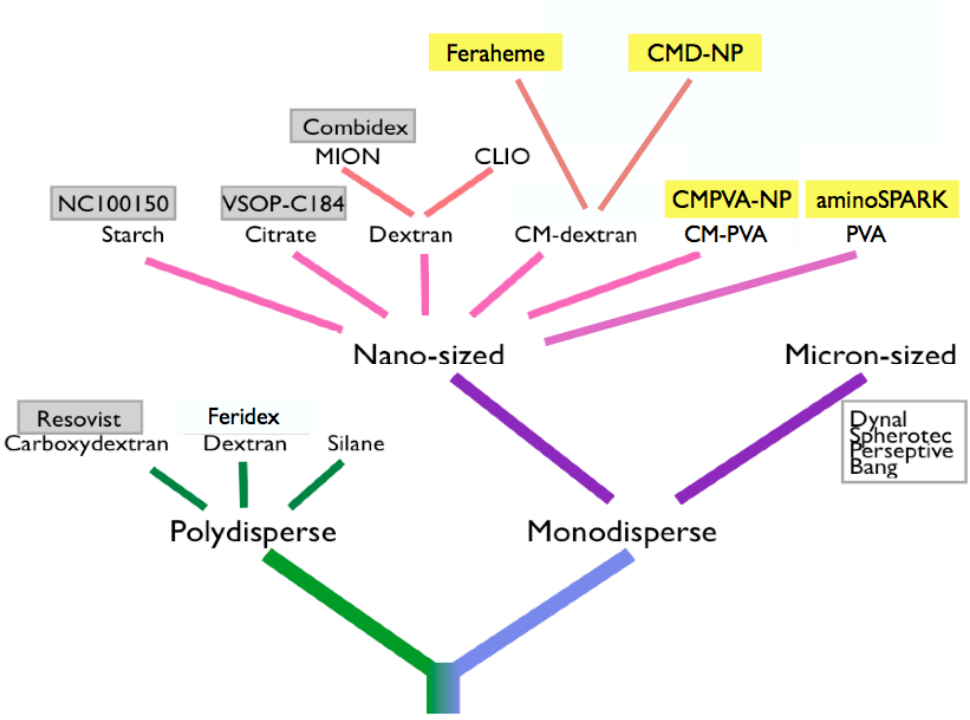

Figure 3. Evolution of magnetic nanoparticles. Boxes shaded grey indicate preparations in clinical trials in the United States. Boxes shaded yellow indicate preparations used in this dissertation.

The newest class of iron oxide nanoparticles are molecularly targeted, long-circulating preparations that have stable polymer coatings that are not cross-linked. An ideal imaging agent

has high affinity (sub-nanomolar to nanomolar) for its target, has low levels of nonspecific binding/uptake, has low toxicity, has a detection method with high resolution, avoids clearance before it reaches its target, and yet is eventually cleared to allow longitudinal study of the subject. A molecularly targeted imaging agent for an aggressive subtype of prostate cancer is discussed in Chapter 4. Ferumoxytol (Feraheme®) is one of the most recently FDA-approved iron oxide nanoparticle agents, and has excellent stability without crosslinking. Modification of the coating of Feraheme will be discussed in Chapter 6 and the use of a modified Feraheme for cell labeling will be discussed in Chapter 7

3.5 Magnetic Properties

Iron oxide nanoparticles' magnetic properties are determined by a variety of factors including their composition, the chemical phases present, their microstructure, and their size and shape. The ability to tune these properties and dictate the potency of a nanoparticle is an important component of nanoparticle design.

3.5.1 Background on Magnetism

There are several different types of magnetism that can be exhibited in materials depending on the arrangement and composition of atoms. It is the special structure of some iron oxides that give rise to the magnetic properties that make them useful as MR contrast agents. Many factors can influence a material's magnetic state, including size and crystal structure, as well as environmental factors such as temperature and pressure.

Diamagnetism occurs in all materials but is often overwhelmed by more prominent paramagnetic and ferromagnetic effects. All materials will experience a dipole moment in

opposition to an externally applied magnetic field due to the change in orbital velocity of paired electrons around atomic nuclei. However, this effect is not dominant in most materials and only a few known materials (e.g., water, bismuth, superconductors) exhibit observable diamagnetic behavior.

Materials such as iron that have unpaired electrons, i.e., they possess orbitals with one electron in them, can exhibit paramagnetic behavior. When there are two electrons in an orbital the Pauli Exclusion Principle dictates that the two electrons must have opposite spins; in these situations their magnetic fields cancel each other out. However, unpaired electrons are free to align in a direction that will yield a net magnetic dipole moment in response to an externally applied magnetic field, and if they align parallel to the field these materials are considered paramagnetic. In the absence of an external field entropic effects due to thermal motion cause the spins of the electrons to align randomly, yielding a net magnetic dipole moment of zero. The temperature at which this thermal motion becomes a weak and negligible effect is a transition temperature known as the Curie temperature.

When a material contains atoms in different sublattices pointing in different directions to yield a net magnetic moment of zero they are known as anti-ferromagnetic. This ordering disappears at the Néel temperature, above which the material is generally paramagnetic. If the magnetic moments of the different sublattices do not cancel each other out the material is considered to be ferrimagnetic, a type of magnetism described below.

Materials that have a permanent magnetic dipole even in the absence of a magnetic field are described as ferromagnetic or ferrimagnetic. Materials that contain only spins going in the same direction, all contributing to the net magnetization, are referred to as ferromagnetic. Ferrimagnetic materials like iron oxides contain a number of anti-aligned ions that are not

canceled out by ions aligned with the field. The ability of unpaired electrons in ferrimagnetic materials to spontaneously align is due to quantum mechanical effects. Again, there exists a critical temperature known as the Curie temperature (or Néel temperature for anti-ferromagnetic materials) above which these materials are no longer ferromagnetic and exhibit paramagnetic behavior.

Superparamagnetism occurs in ferrimagnetic nanoparticles that are small enough that the affect of thermal energy becomes significant even when the material is below its Curie temperature. The Néel-Arrhenius equation describes this phenomenon by showing the effect of thermal fluctuations on the average length of time between random flips in the direction of the magnetization moment:

$$\tau_N = \tau_0 \exp(KV/(k_B T))$$

where τ_N is the mean time between flips, τ_0 is the material property of the attempt time (typically between 10^{-9}-10^{-10} seconds), K is the magnetic anisotropy of the nanoparticle, V is the volume of the nanoparticle, k_B is the Boltzmann constant, and T is the temperature. If the measurement time is much shorter than τ_N, the nanoparticle will appear to have ferrimagnetic qualities even if the material is below its Curie temperature. It is clear from the presence of V in the equation that the nanopartice dimensions are an important factor in determining the superparamagnetic qualities. For iron, the critical diameter for spherical particles to become a single domain is 14 nm, and for Fe_3O_4 the critical diameter is 128 nm.[51] Superparamagnetic nanoparticles only exhibit net magnetic dipoles when an external magnetic field is applied, relaxing to their initial state once the field is removed.

In general, a material will experience a magnetic induction B when an external field of strength H is applied as defined by the following equation:

$$B = \mu_0(H + M)$$

where μ_0 is the permeability of free space and M is the magnetization of the material. M is defined as the magnetic moment per unit volume m/V. Another important parameter of magnetic materials is their volumetric magnetic susceptibility χ, a dimensionless number that is defined by:

$$M = \chi H$$

The different classes of magnetic materials discussed above will have different values of χ, with ferro/ferrimagnets having larger values and paramagnets and diamagnets having smaller values.

3.5.2 Characterization of Magnetic Properties

A superconducting quantum interference device (SQUID) is a type of sensitive magnetometer that can measure very weak magnetic fields, even fields as low as 10^{-14} T. The device consists of two parallel Josephson junctions, which are two superconductors separated by a non-conducting barrier thin enough to allow electrons through; this flow of electrons is referred to as a Josephson current. A magnetization (M) versus field (H) hysteresis loop can be drawn to determine the magnetic properties of the nanoparticle (Figure 4). If an externally applied magnetic field is large, some of the spins in a magnetic material will align with the field. The maximum value of this magnetization is known as the saturation magnetization M_s. When the value of the external magnetic field goes down, the number of aligned spins will also tend to go down. If a material is ferro/ferrimagnetic, the magnetization at zero field does not return to zero

and that residual magnetic moment is known as the remanent magnetization M_r. The magnitude of the field required to bring the material back to zero magnetization is known as the coercive field H_c. The ratio of the remanent magnetization to the saturation magnetization is known as the remanence ratio M_r/M_s, which is a value from 0 to 1.

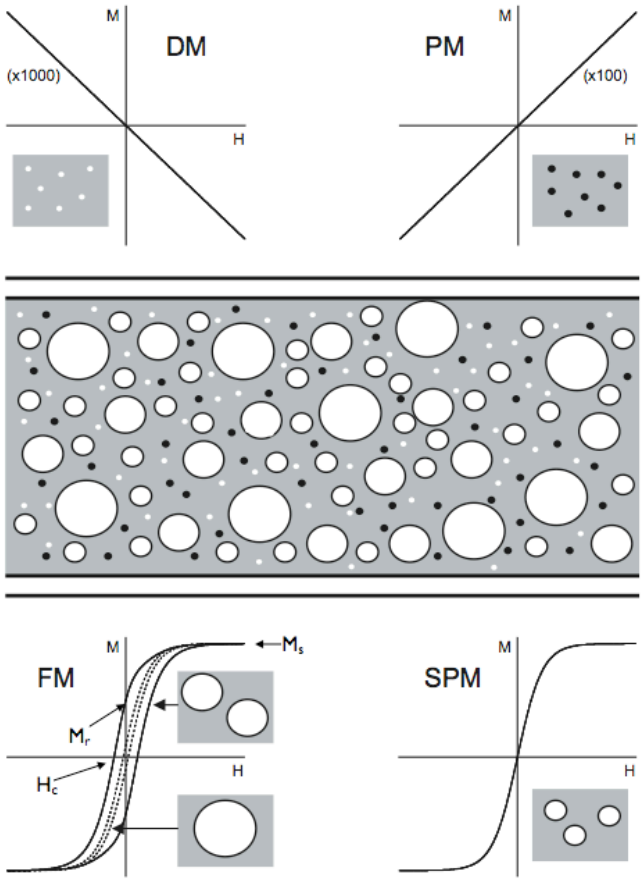

Figure 4. Hypthetical M-H curves of a particles exhibiting different types of magnetism injected into a blood vessel. Top left: diamagnetic material (DM), top right: paramagnetic material (PM), bottom left: ferromagnetic material (FM), bottom right: superparamagnetic material (SPM). Key magnetic parameters are highlighted in the FM case: Remanent Magnetization M_r, Saturation Magnetization M_s, and the Coercivity H_c, and multi-domain ferromagnetic materials (------) versus single-domain materials (——) are shown. The SPM case is the FM case smaller than a critical diameter where the spins in the particle are affected by thermal fluctuations. Adapted from reference 52.

In this dissertation, the SQUID is used to draw M-H loops at constant temperature to assess magnetic behavior and determine the saturation magnetization (Chapters 4, 5). In general the saturation magnetization of nanoparticles decreases with particle size and increases with crystallinity.[53,54]

NMR relaxometry another technique for determining how nanoparticles will behave in the MR scanner. In the presence of a magnetic field, e.g. one produced by a relaxometer or an MR imager, the magnetic moments of superparamagnetic nanoparticles align and exhibit a net magnetization. A radiofrequency pulse then perturbs the alignment of the moments and causes the spins to precess. After the energy from the pulse is removed the susbsequent relaxation can be measured. The relaxation times R1 and R2 can be calculated from the slopes of 1/T1 and 1/T2 versus concentration, respectively. High relaxivities are desired since (in most situations) less nanoparticle will be needed to achieve high resolution and sensitivity. The relaxivity of an MR contrast agent describes its effectiveness to lower the T1 and T2 relaxation times of the signal, and is given by:

$$\frac{1}{T_{1,2}} = \frac{1}{T_{1,2}^{0}} + r_{1,2}C$$

where C is the concentration of contrast agent. Many factors can influence the potency of a nanoparticle, including the method of synthesis of the nanoparticle, the size and crystal structure of the core,[55] and the surface chemistry and thickness of the coating.[56] The coating can affect how water protons interact with the magnetic field created by the superparamagnetic core.[57]

Although the spin-spin relaxation time (T2) is reduced by the presence of superparamagnetic nanoparticles, the extent to which this occurs in vivo is the result of a rather complex combination of factors including the chemical environment around the nanoparticle and

how the nanoparticle is compartmentalized in the tissue. Even if it is possible to determine the R2 of the nanoparticle in vitro it is not always straightforward to predict the extent to which it will lower the T2 in vivo, although it is an excellent first approximation for preclinical characterization. Contrast agents for MR were described in more detail in Section 2.3.

CHAPTER 4: THE USE OF A TARGETED FLUORESCENT IRON OXIDE NANOPARTICLE TO NON-INVASIVELY IMAGE AND STRATIFY PROSTATE CANCER

4.1 Summary

This chapter will explore how an iron oxide nanoparticle conjugated to a ligand that targets a specific subtype of cancer can be used to stratify cancer patients. Prostate cancer is the most commonly diagnosed non-skin malignancy in the United States and presents with a wide range of aggressiveness, from extremely slow-growing to highly aggressive. There is a clinical need to determine the metastatic potential of a cancer in order to design the most appropriate treatment plan. In this chapter we describe the development of an iron oxide nanoparticle-based imaging agent that targets SPARC (secreted protein acidic rich in cysteine), a molecular marker of prostate cancer metastatic potential. Previous studies by this group used phage display to find

a peptide with high binding affinity for the protein SPARC. Here the SPARC-targeted peptide is conjugated to a biocompatible iron oxide nanoparticle that is also coupled to a fluorophore for optical imaging. Prostate cancer cell lines with varying degrees of SPARC expression were used to show the ability of this imaging agent to bind specifically to SPARC in vitro and in vivo. We have developed an optical imaging agent that can non-invasively access molecular information that correlates with the metastatic potential of the prostate tumor. This prognostic information could enable clinicians to stratify patients and design appropriate treatment strategies.

4.2 Background on Prostate Cancer

A man living in the United States has a 50% chance of developing some type of cancer in his lifetime, and prostate cancer is the second most commonly diagnosed cancer in this group.[58] The incidence of prostate cancer increases with age more than for any other cancer; at 60-79 years of age the chances for a man in the United States to be diagnosed with prostate cancer is 1:8. As the population ages, the number of cases of prostate cancer is only expected to increase.[59]

Early detection is essential for local therapies such as surgery or radiation to be effective, and surgery has been shown to reduce deaths from prostate cancer as compared to a regimen of watchful waiting.[60] After local therapy, prostate cancer recurs in up to 40% of men, which is likely a result of the cancer spreading before a diagnosis was made.[61] On the other hand, there is also a risk of over detection due to systematic screening, leading to unnecessary treatment.[62]

Current methods for diagnosing prostate cancer are neither specific nor sensitive. A digital rectal exam (DRE) can only detect tumors of a certain size and position, causing many tumors to go undetected. The gold standard for prostate cancer detection is blood tests for serum

prostate specific antigen (PSA), a protein that is also produced by both normal and hypertrophied prostate. Thus some men may have a high circulating PSA caused only by benign prostatic hypertrophy (BPH), infection, or other factors, and would have to endure unnecessary biopsies and emotional distress. Autopsy findings[63-65] and the recent results of the Prostate Cancer Prevention Trial[66] indicate the prevalence of prostate cancer is much higher than anticipated in men with PSA levels considered to be in the normal range (<4 ng/ml). Conversely, some men may have low circulating PSA due to a smaller prostate gland, but still have prostate cancer; in these cases the prostate cancer would be missed. Although there have been some improvements in how PSA is used as a diagnostic tool, such as considering the rate of PSA increase (i.e. the PSA velocity) instead of the absolute concentration, and taking into account effects due to age, ethnicity, and prostate size, relying on PSA for prostate cancer diagnosis is still educated guesswork at best.[67]

Recent attempts to improve sensitivity for prostate cancer diagnosis have included more invasive procedures such as transrectal ultrasound-guided biopsies. Generally six to eight biopsies are taken, and sometimes many more, from various locations in the prostate. A pathologist evaluates the biopsies and gives a prognosis that will determine the course of treatment. Biopsies are invasive and time-consuming, and it is entirely possible that they could miss the tumor location, or miss the presence of a higher-grade cancer. Furthermore, histologic analysis is time- and labor-intensive and can be prohibitive in a research setting in terms of economics, time, and survival of the research animal during longitudinal studies.

Clearly new biomarkers for prostate cancer detection and new ways to image prostate cancer are needed. In addition, prostate cancer is a heterogeneous disease, so knowledge of prostate cancer at the molecular level can help determine an appropriate course of treatment.

Finally, it would be helpful to accurately define the tumor volume to guide the surgeon during a prostatectomy, which current modes of detection cannot provide.

Many disciplines come together in an attempt to design new molecularly-targeted diagnostic tools for prostate cancer. Research on the etiology of prostate cancer has given us a wealth of new information and has revealed potential new biomarkers for the presence of prostate cancer and for accurate staging. High-throughput screening methods can be used to find affinity ligands to these new biomarkers. Advances in our ability to engineer materials at the nanoscale have allowed us to tailor nanoparticles to interact with biological systems with unprecedented specificity. Crucially, these nanoparticles interact on the scale at which cell signaling and other biological processes interact, so that the attachment of molecules of different functionalities, e.g., imaging moieties and targeting moieties, can direct the nanoparticle to a molecularly specific location and then report where it has been readdressed.

Molecularly targeted imaging agents are important for several reasons. Firstly, they can be used as probes of the biological mechanisms of human disease. Secondly, since they can be more sensitive than current means of detection, making them ideal for early detection of tumors. Thirdly, imaging is a non-invasive way of gathering information about the tumor, allowing the researcher to stratify patients and design treatment plans without any of the possible side effects from more invasive methods. Finally, they can be used to monitor a treatment plan and quickly determine whether a course of treatment is working.

In order to find new biomarkers for prostate cancer, researchers must investigate prostate cancer at the molecular level. Microarray studies have been particularly beneficial in determining the differential expression of genes in normal prostate tissue versus cancerous prostate tissue and have implicated several genes as playing a role in the progression of this cancer.[68] An ideal

target biomarker would be on the cell surface for optimal accessibility, be present in high numbers, and have a significantly different expression profile than the other types of cells in their milieu, be they normal cells or more benign tumor cells if the goal is to stratify subtypes of prostate cancer within a heterogeneous tumor. One of the biomarkers used to distinguish more aggressive subtypes of prostate cancer is described in the next section.

4.3 Background on Secreted Protein, Acidic, Rich in Cysteine (a.k.a. SPARC, osteonectin, BM-40)

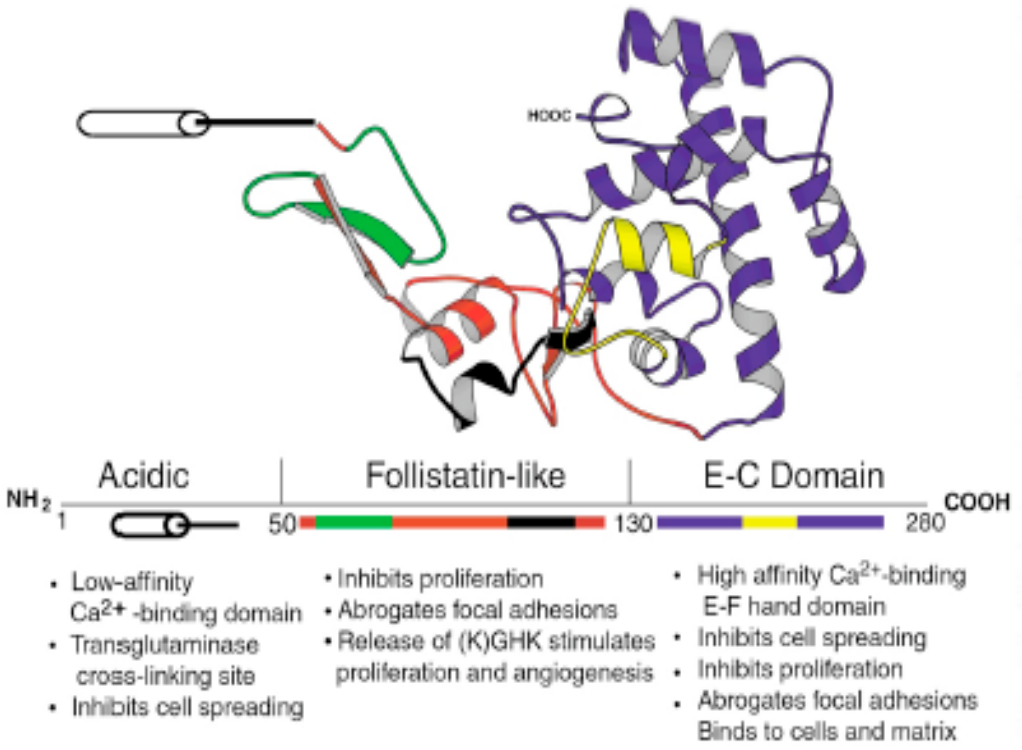

Figure 5. Structure of SPARC as derived from crystallographic data. Adapted from reference 69.

SPARC is a 32 kDa glycoprotein involved in a variety of mechanisms including development, cell turnover, angiogenesis, and tissue remodeling and repair. SPARC consists of a Ca^{+2}-binding extracellular domain, a follistatin-like bioactive domain, and an acidic domain on the NH_2 terminus (Figure 3).

Classification	Description	Reference
Glioma	Expression in tumor cells associated with invasion and growth inhibition	Schultz et al. [2002]
	Expression enhances invasion	Rich et al. [2003]
Neuroblastoma	Expression by Schwannian stroma inhibits angiogenesis and impairs tumor growth	Chlenski et al. [2002]
Melanoma	Enhanced expression in tumor cells promotes metastasis	Ledda et al. [1997]
Adenocarcinoma (pancreas)	Aberrant methylation in tumor; expression in stroma	Sato et al. [2003]
Carcinoma (pancreas)	Part of invasion-specific cluster	Ryu et al. [2001]
Carcinoma (breast)	Part of invasion-specific cluster, expressed in juxtatumoral stromal cells	Iacobuzio-Donahue et al. [2002b]
	Fold change: 65↑ in highly-invasive lines, and 2↓ in weakly invasive lines	Zajchowski et al. [2001]
Carcinoma (colorectal)	Expressed preferentially in tumor-associated blood vessels	St Croix et al. [2000]
Non-small-cell carcinoma (lung)	Increased expression in tumor cells after coculture with normal fibroblasts	Fromigue et al. [2003]
	Downregulated with tumor growth	Bendik et al. [1998]
Carcinoma (ovary)	High levels produced by tumor cells promote their apoptosis	Yiu et al. [2001]

Figure 6. SPARC is expressed in a variety of forms of human cancer, and is part of the invasion-specific cluster for several tumor types. Adapted from reference 70**.**

SPARC has been associated with many types of human cancers, including pancreatic, breast, ovarian, and small-cell lung carcinoma, and gene profiling has identified SPARC as part of an invasion-specific cluster of genes in pancreatic and breast carcinoma (Figure 6). In fact, SPARC is often expressed by metastatic tumors and has been called the "proinvasive" protein.[71] It has been shown that SPARC disrupts cell adhesion,[72] promotes changes in cell shape,[73] plays a role in wound healing, and is active in angiogenesis and tumorigenesis.[74] The expression of SPARC produces intercellular gaps, which promote vessel permeability, thus facilitating leukocyte extravasation;[75] this mechanism is due to the binding of SPARC with VCAM-1.[76] SPARC is also a component of the bone matrix and has a promigratory, anti-adhesive effect on

cells.[69] SPARC has also been shown to play a role in cancer immunity: SPARC-null mice exhibited decreased macrophage infiltration of tumors, and it has been shown that SPARC inhibits antitumor polymorphonuclear leukocyte (PMN) activity, aiding in tumor avoidance of immune surveillance.[77]

There seems to be a correlation between SPARC expression and prostate cancer invasiveness to bone, although its exact role has been debated. Thomas et al. demonstrated that SPARC mRNA expression was higher in bone-metastasizing prostate cancer cell lines, and also showed intense SPARC staining in metastatic lesions in bone.[78] Exogenously added SPARC has been shown to contribute to the osteotropism of adenocarcinoma cells.[79] SPARC has also been shown to interact with members of the matrix metalloproteinase (MMP) family, known players in proteolysis of the ECM, leading to tumor invasion and metastasis. Complicating the picture is a study by De et al. which demonstrated that SPARC supports the migration of highly metastatic cell lines to bone, but that it is the bone-derived (and not tumor cell-derived) SPARC that determines this behavior.[80] This study was performed using SPARC-null mice, but unfortunately the researchers did not take into account tumor cell–derived SPARC so it is difficult to interpret the results. It is possible that both sources of SPARC are necessary for prostate cancer bone metastasis. One theory is that in order for the prostate cancer cells to thrive in bone they must be "osteomimetic," which would include expression of proteins such as SPARC. These studies seem to support Fidler's 2003 "seed and soil" hypothesis of cancer metastasis, where the tumor cell (the "seed") must be mobile and able to deadhere from the primary tumor site, and additionally the bone (the "soil") must be conditioned for tumor growth.[81]

Interestingly, SPARC over-expression has also been shown to inhibit tumor cell proliferation in vitro and in vivo.[82, 83] There are many possible explanations for this seemingly

contradictory finding, but one is that the regulation of SPARC expression must be timely to result in an invasive phenotype. It has been shown that certain factors that can inhibit early stage tumors can then switch and become mitogens for more advanced tumors, i.e. ones that could imminently metastasize.[84]

Despite controversies over whether SPARC is tumor or stroma-derived, there is a clear indication that its presence denotes an aggressive form of prostate cancer, making it an excellent biomarker for diagnostic imaging. How this biomarker can be targeted is described in the following section.

4.3.1 Phage Display for Identification of Affinity Peptides to SPARC

There are many methods for identifying affinity ligands to target molecules. High-throughput screening methods have been used as a brute force method to test a large number of different molecules as the most efficient and effective way to design affinity ligands. In general we do not have a complete enough understanding of molecular interactions to design the structure of a molecule to bind to a target biomarker; instead, we can use a process of trial-and-error, testing a large number of molecules to determine which molecule binds the best. Targeting moieties can consist of many different types of molecules including peptides, oligonucleotides, small molecules, and antibodies. Antibodies have been shown to successfully target nanoparticles to specific tissues of interest.[85-87] Peptides and small molecules can have similar affinities as antibodies but are much less expensive, easier to synthesize, and easier to purify and handle. They are also less likely to be immunogenic, have less steric hindrance of binding, and are much more likely to be FDA-approved.

Phage display is one of the most powerful methods for finding a peptide sequence that can bind to a target of interest. In this high-throughput screening approach, bacteriophage that have been genetically modified to display a library on their protein coat are used to test binding to a target. When the molecular structure of the target is not known it is sometimes possible to use this method to isolate and characterize the target and determine its identity after the fact. Random peptide sequences are the most commonly used library because they are diverse, commercially available, and are the easiest method for high throughput screening.

Screens can be performed directly on target molecules (e.g., as proteins immobilized on plates), although complications can sometimes arise from the fact that the target molecule is not in its native environment and the required interaction in vivo may be more complex. Furthermore, since generally one peptide binds to one target in this type of screen, there is no amplification of signal. A potential improvement is to screen on live cells expressing the target molecule, a technique which can be used when targeting a cell type without any prior knowledge of a potential biomarker. Amplification of signal is possible in this type of screen because phage clones can become internalized and then trapped within the cell, concentrating the imaging moiety and essentially eliminating K_{off}, thereby making the affinity effectively infinite. Binding under physiological flow conditions is a further refinement that can increase the chances that the molecule found in the screen will actually bind in vivo, and is particularly important when the target cells are endothelial. The most complex system for carrying out a phage display screen is *in vivo* for the targeting of specific organs or disease. Obviously the clones chosen from this type of screen have already overcome *in vivo* delivery barriers to be selected so these clones are even more easily translatable for use as an *in vivo* targeting agent. However, the complexity and cost of this type of in vivo screen may be prohibitive.

There are many advantages to using phage display. It is much more rapid and economical than traditional chemical re-synthesis, it provides a large peptide diversity, and it benefits from the many types of phage clones and libraries. Furthermore, bacteriophage only have a single copy of each gene, therefore protein expression is not dependent on the expression and interaction of multiple genes. In other words, genotype equals phenotype since one gene leads to one protein and vice versa. Thus when a clone is chosen based on its phenotypic characteristics it is identifiable by the appropriate portion of its genome.

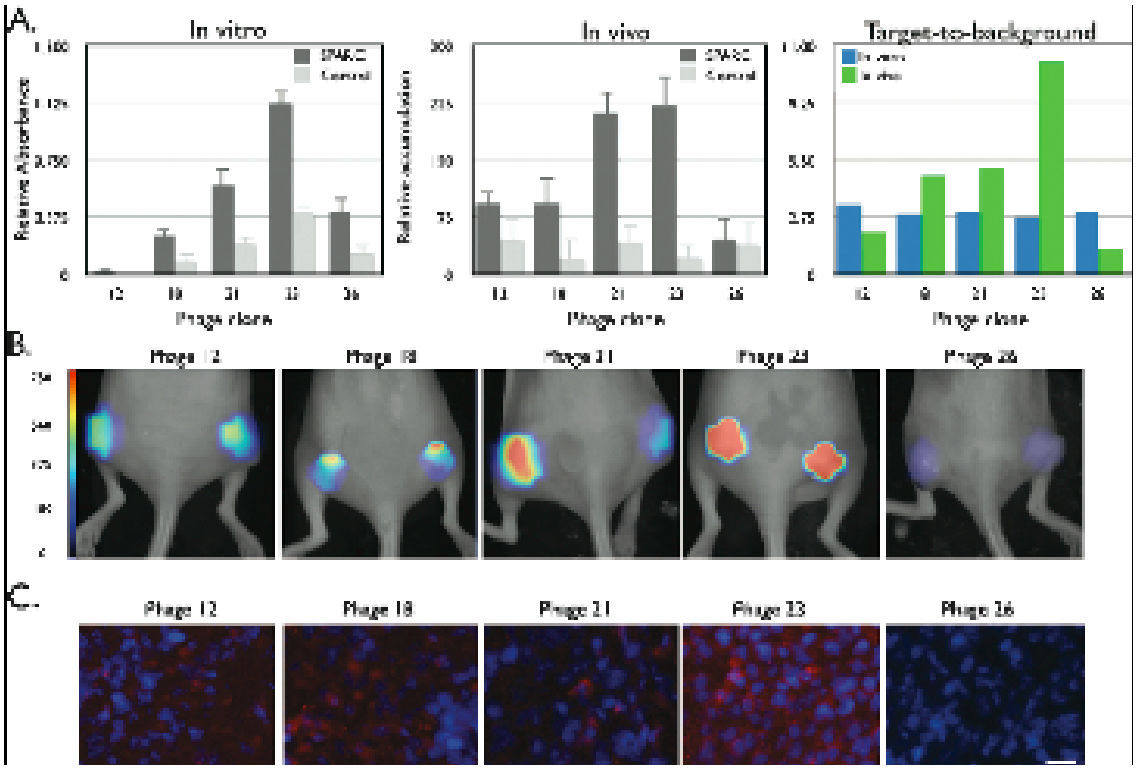

Figure 7. Comparison of SPARC-targeted phage clones. A) Comparison of target affinity B) In vivo imaging of Lewis lung carcinoma tumors using FMT. C) Comparative immunofluorescence of tumor accumulation for each phage clone. Nuclei have been counterstained with DAPI (blue). Scale bar = 10 nm. Adapted from reference 88.

In order to find an affinity peptide to SPARC Kelly et al. used phage display to screen a linear 7mer peptide library against purified SPARC in vitro.[88] There were several hits but only one, SPPTGIN (henceforth referred to as SPP), targeted well in vivo. SPP is Phage 23 in Figure 6.

Each affinity peptide sequence is then modified to include a C-terminal extension for fluorescent labeling with FITC as well as providing a cysteine handle for nanoparticle conjugation. Conjugation of a targeting moiety to a nanoparticle has been shown to improve pharmacokinetics, improve stability, and can improve affinity and/or avidity of the targeting molecule via multivalency effects. In this study we will use the commercially available nanoparticle aminoSPARK as the imaging agent that will be conjugated to SPP.

4.4 Aims

Approximately one out of every six men will be diagnosed with prostate cancer in the United States. Treatment options for localized disease vary considerably, and range from "watchful waiting" (no active treatment) to radical prostatectomy. However, it is difficult to ascertain which treatment option is appropriate because the ability of the treating physician to accurately predict the tumor's metastatic potential is limited. Prostatic biopsies are crucial both for diagnosing prostate cancer and for deriving prognostic information. However, prostate biopsies are invasive, time consuming, and are limited by a high degree of sampling error.[89] In part due to the problems with prostate biopsies, it is not uncommon for treatment of prostate cancer to be incorrectly paired with the underlying disease aggressiveness, commonly resulting in patients with slow-growing tumors enduring unnecessary surgery and conversely, patients

with more aggressive tumors relegated to watchful waiting.[90] Here we have synthesized a non-invasive imaging agent that provides insight into the metastatic potential of prostate cancer, an important tool that could aid clinicians in recommending the most appropriate treatment for their patients.

4.5 Introduction

Secreted Protein Acidic and Rich in Cysteine (SPARC), also known as osteonectin or BM-40, is a ~32kDa matricellular glycoprotein that modulates cell-matrix interactions and is expressed in a variety of tissues during development and during tissue repair and remodeling.[71] It is involved in a diverse range of mechanisms and has been shown to disrupt cell spreading and adhesion,[91] disassemble focal adhesions,[72, 91] mediate leukocyte diapedesis,[76] induce cell rounding and changes in cellular morphology[73, 75, 92], regulate cell proliferation [93, 94], and it has demonstrated activities in angiogenesis,[95] extracellular matrix remodeling,[96, 97] and tumorigenesis.[74] Furthermore, SPARC has been shown to be involved in the endothelial to mesenchymal transition (EMT), a hallmark of tumor invasiveness[98] and prostate cancer progression,[99] by repressing E-cadherin.[100]

Recently, analysis of human tumor samples has indicated the presence of high levels of SPARC expression correlating with clinical prognosis and outcome. Indeed, in breast, lung, pancreas, and prostate cancer, high levels of SPARC indicates a worse prognosis.[101] Gene expression profiling has shown that SPARC is expressed more highly in prostate cancer of higher Gleason grades.[102] Studies showing differential expression of SPARC in prostate cancer revealed that SPARC is expressed most highly in bone-metastasizing prostate cancer cell lines and metastatic lesions in bone demonstrated intense SPARC staining.[78] It has also been shown

that endogenous SPARC expression in the bone itself can contribute to prostate cancer metastasizing to bone.[80] In certain prostate cancer cell lines SPARC has been shown to increase activity of the matrix metalloproteinases,[79] a class of molecules strongly associated with tumor invasion and metastasis.[103]

SPARC is expressed in various other human cancers as well, and its presence is often correlated with high metastatic potential. Gene profiling has found SPARC to be part of the invasion-specific cluster in both pancreatic and breast carcinoma,[70] and SPARC expression is associated with invasiveness and metastasis in gastric cancer.[104] These findings of SPARC expression correlating with a worse prognosis is not surprising given that SPARC has been shown to mediate many of the steps in the metastatic pathway, such as cell rounding, disruption of focal adhesions, and degradation of the extracellular matrix. In fact, its promigratory, anti-adhesive effect on cells has led to SPARC being referred to as the "proinvasive" protein.[69]

Given the role of SPARC in invasion and metastasis and that SPARC expression has been shown in various studies to be correlated with increased metastatic potential and poor clinical outcome of patients with prostate cancer, it is an ideal target for imaging agents seeking to stratify prostate cancer patients. In this work we have developed and thoroughly characterized an imaging agent that can detect a metastatic subpopulation of SPARC-expressing cells, enabling a non-invasive, molecular-based approach to prostate cancer prognostication and treatment selection.

4.6 Experimental

Cell Lines

LNCaP and DU145 cell lines were obtained from the American Type Tissue Culture Collection (ATCC), and LNCaP-C42 and LNCaP-C42b cell lines were a generous gift from Dr. Michael Weber, University of Virginia Cancer Center. LNCaPs were grown in RPMI 1640 media supplemented with 10% fetal bovine serum, C42s and C42bs were grown in T-Media supplemented with 5% fetal bovine serum, and DU145s were grown in MEM supplemented with 10% fetal bovine serum. All cultures were maintained in a CO_2 humidified incubator at 37°C.

Western Blot

LNCaP, LNCaP-C42, LNCaP-C42b, and DU145 cells were grown in 24 well plates to confluence then harvested via scraping with 500 uL of 1 % Triton X-100 in PBS with mammalian protease inhibitor cocktail added (Sigma, St. Louis, MO). Protein concentrations of lysates were quantified via Bininchoninic Acid (BCA) protein assay (Pierce, Rockford, IL) and equal amounts of protein from each fraction were size-fractionated by SDS-PAGE. All fractions were analyzed for SPARC expression via Western blotting.

Static Transwell Assay

Cells were grown to 80% confluence in the upper chamber of Boyden chamber inserts (Millipore, Billerica MA) and the number that invaded the lower chamber was determined using a Coulter Counter.

Histology and Immunohistochemistry

Prostate disease spectrum (prostatic cancer progression) arrays were purchased from US Biomax, Inc. (Rockville, MD) and probed with anti-SPARC antibody (NCL-O-NECTIN from Novocastra, Newcastle upon Tyne, UK) at a dilution of 1:20, with standard citrate retrieval. Statistics were performed to compare metastatic to non-metastatic tumor samples using an unpaired t-test. P values of less than 0.05 were considered statistically significant.

Materials Characterization

AminoSPARK 680 and AminoSPARK 750 nanoparticles were purchased from VisEn (Woburn, MA). Information obtained from a phage display screen previously shown to bind to SPARC with high affinity[88] was used to create a peptide sequence, SPPTGINGGSK(FITC)C, which was conjugated to the targeting nanoparticle. To determine iron concentration, aminoSPARK powder was weighed then dissolved in 1 ml 6N hydrochloric acid (HCl) plus 3 μL of 30% hydrogen peroxide for one hour. Percent iron was then deduced by comparing the absorbance of the nanoparticle sample at 435 nm to the absorbance of iron standards. Iron oxide core size was determined by transmission electron microscopy (TEM) on a JEOL 200CX instrument at 200 kV. Dilute nanoparticle solution was spotted onto a copper carbon film TEM grid (Electron Microscopy Sciences, Hatfield PA). Core size distribution was calculated using ImageJ software and manually. Surface morphology and the three-dimensional shape of the nanoparticles was imaged by tapping mode Atomic Force Microscopy (AFM) on a Dimension 3000 Scanning Probe Microscope (Veeco Instruments, Plainview, NY) and analyzed using Veeco's Nanoscope software. Nanoparticles were reacted with N-succinimidyl S-acetylthioacetate (SATA, Molecular Biosciences, Boulder CO), deprotected with hydroxylamine, and then dropcast on Au(111) on mica. Hydrodynamic size of the nanoparticles was determined

by dynamic light scattering (DLS) using a Zetasizer (Malvern Instruments, Marlboro, MA). Magnetic characteristics were determined using an AC and DC Superconducting Quantum Interference Device (AC/DC SQUID, Quantum Design, San Diego, CA) with a field scan range of ± 50,000 gauss at 298K. Chemical makeup and structure of the core was investigated by X-ray diffraction (XRD) on a Rigaku RU300 diffractometer (Tokyo, Japan)

Specificity of SPARC-NP

LNCaP (SPARC positive) and DU145 cells (SPARC negative) were incubated with increasing log concentrations of SPARC-NP and Control-NP for one hour at 37°C, washed three times with DPBS, then harvested by incubation with trypsin, centrifuged and analyzed (10,000 cells/sample) by flow cytometry on a Becton Dickinson FACSCalibur cytometer (Becton Dickinson, Franklin Lakes, NJ). EC_{50}s were determined by fitting a sigmoidal dose response curve. All samples had a single narrow peak (example Fig. 3D). Mean fluorescence was plotted to describe relative uptake. In vivo imaging was performed using FMT-CT in mice with DU145, C42, and C42b xenograft tumors. SPARC-NP and Control-NP were coinjected.

4.7 Results and Discussion

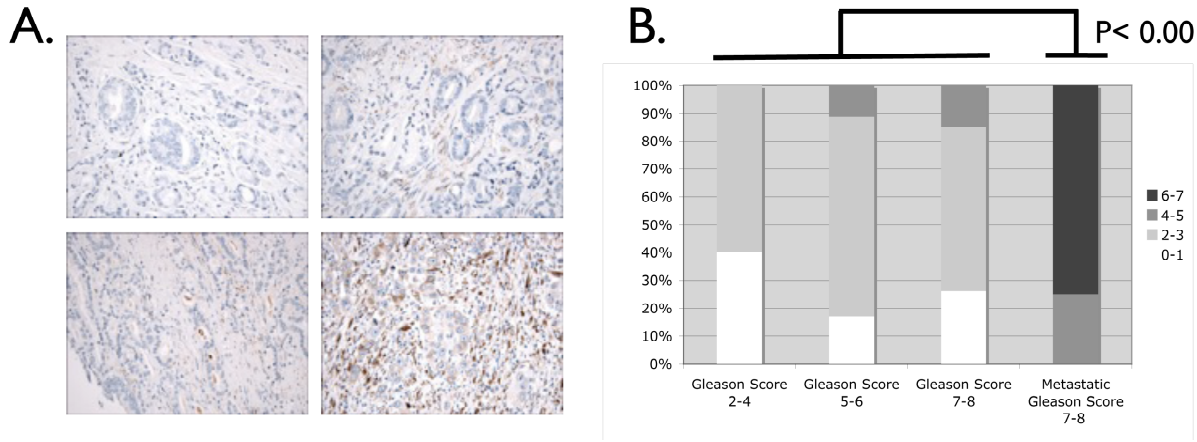

Figure 8. Tissue microarray analysis of SPARC expression shows that it is correlated with prostate cancer progression and metastasis. A. Immunohistochemical analysis of SPARC expression in a prostate cancer tissue microarray of a range of Gleason patterns. Representative staining of cores of Gleason Score 2-4 (upper left), Gleason Score 5-6 (upper right), Gleason Score 7-8 (lower left), and Gleason Score 7-8 (lower right). B. A summary of the expression quantitation in tumoral, stromal, and epithelial compartments scored in intensity from 0-3 and shown here as a single summed score from 0-7.

SPARC Expression Correlates with Prostate Cancer Grade

SPARC expression in 53 human prostate cancer samples was measured by imunnohistochemical analysis of tissue microarrays consisting of cores of various cancer grades (Figure 8A). As prostate cancer becomes advanced, SPARC expression increased with metastatic cancer samples expressing the highest levels of SPARC (Figure 8B). SPARC expression was most prominent in the epithelial and stromal compartments of the tumors analyzed. These immunohistochemical results are supported by data reanalyzed using Oncomine[105] from Lapointe et al.[102] (Figure 9), which also show increasing SPARC expression with prostate cancer progression.

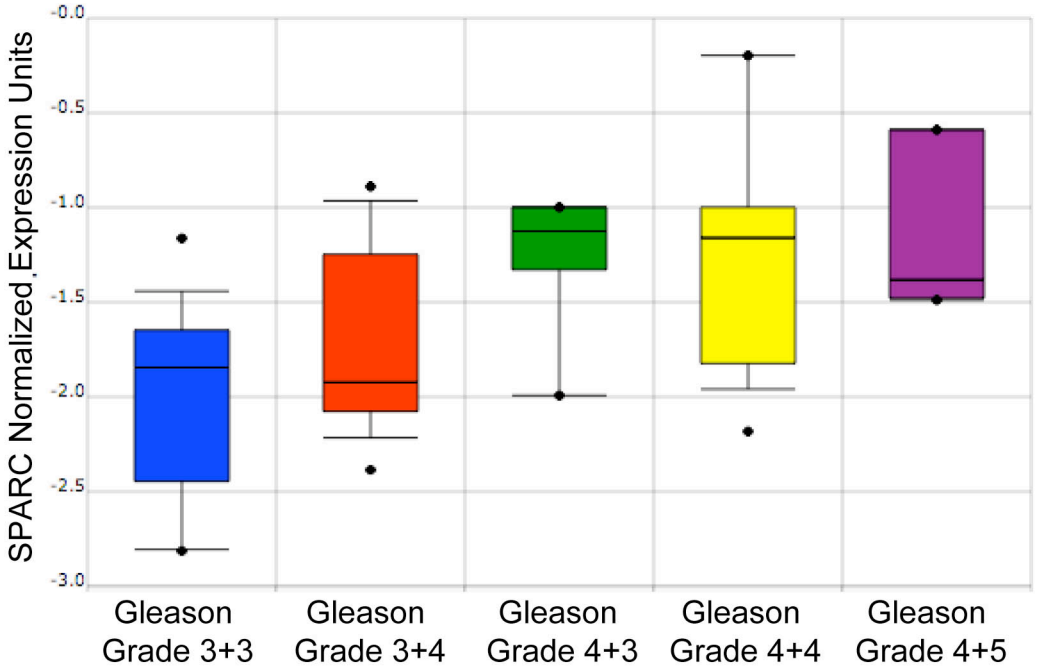

Figure 9. Microarray gene expression data shows SPARC expression is correlated with prostate cancer progression and metastasis. Oncomine[105] analysis of gene expression data originally obtained by Lapointe et al. illustrates that increasing SPARC expression correlates with increasing Gleason Grade.

SPARC Expression Correlates with Cell Migratory Capacity

Cell motility plays a key role in prostate cancer progression and metastasis,[106] and we thus sought to quantitate a correlation between cell motility and SPARC expression. We have chosen to work with LNCaPs, LNCaP-C42s, LNcaP-C42Bs, and DU145s, four cell lines that display a range of SPARC expression.[78] C42s and C42Bs are in vivo-derived sublineages of LNCaPs that mark cancer progression milestones: C42s mark androgen independence and C42Bs mark bone metastasis. Expression of the protein SPARC in each of the four cell lines was confirmed using immunoblotting (results not shown). LNCaP, C42, and C42b cell lines exhibit increasing levels of SPARC expression respectively, while DU145s exhibit little to no SPARC expression and serve as an important negative control in this study.

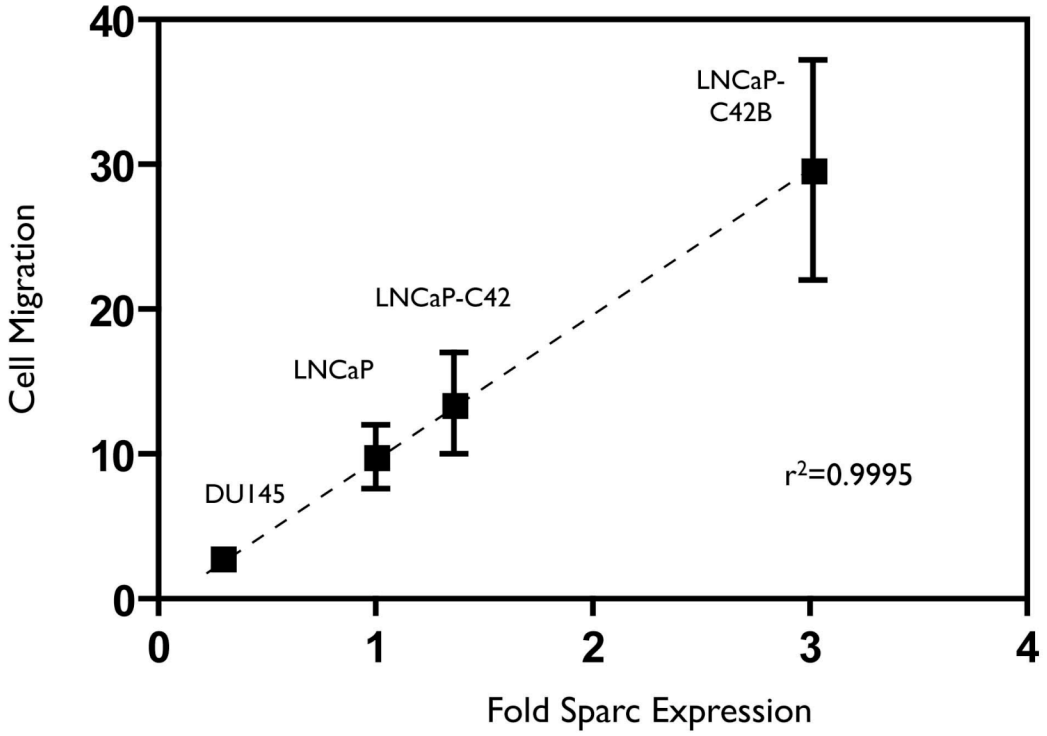

Figure 10. SPARC expression in prostate cancer cell lines is correlated with migratory potential. Results from a static transwell assay plotted against SPARC expression (determined by immunoblotting) shows a correlation between cell motility and expression of SPARC for LNCaP, LNCaP-C42, LNCaP-C42B, and DU145 cell lines. A linear fit of the data had an r^2 value of 0.9995.

Each cell line's transmigration potential was studied using a static transwell assay (Figure 10). Transwell migration correlated closely with SPARC expression as determined by Western blot (results not shown); the linear fit shown in the graph in Figure 10 has an R^2 of 0.995.

Materials Characterization of the Imaging Agent

In order to successfully translate imaging agents to the clinic it is important to have an understanding of the material properties of the agent. We have thus characterized the

nanoparticle-based agent that we have developed for SPARC imaging. A schematic of the two types of nanoparticles used in this study is shown in Figure 11.

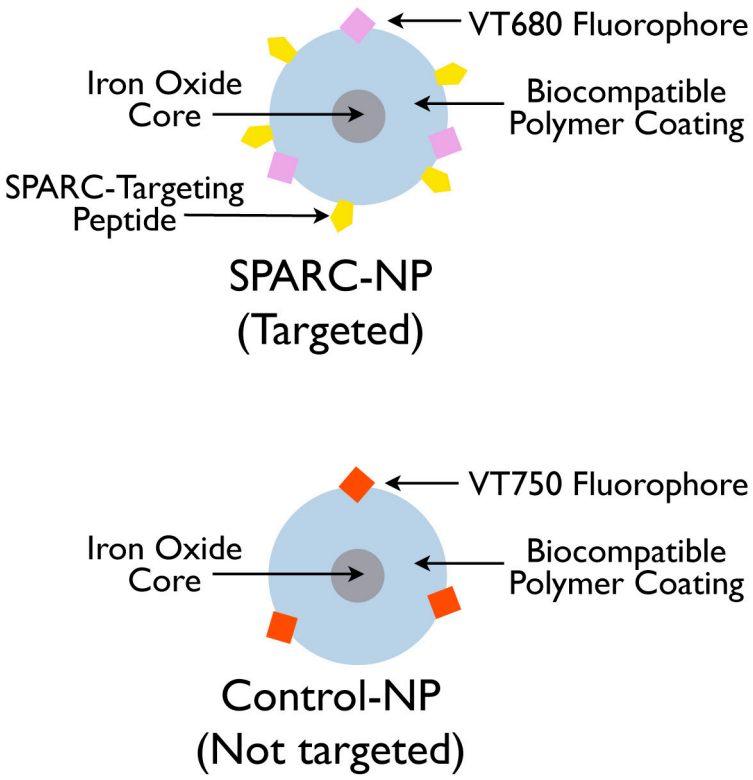

Figure 11. Schematic of the targeted and control nanoparticles.

The SPARC targeted nanoparticle (SPARC-NP) is conjugated to a SPARC-targeting peptide,[88] as well as a fluorophore at a wavelength of 680 nm for in vivo imaging. The control nanoparticle (Control-NP) does not contain a targeting moiety and is conjugated to a fluorophore at a wavelength of 750 nm, allowing for ratiometric imaging of both control and targeted nanoparticles in the same animal and tumor in vivo. The absorbance, fluorescence, and emission spectra of the two nanoparticles are shown in Figure 12.

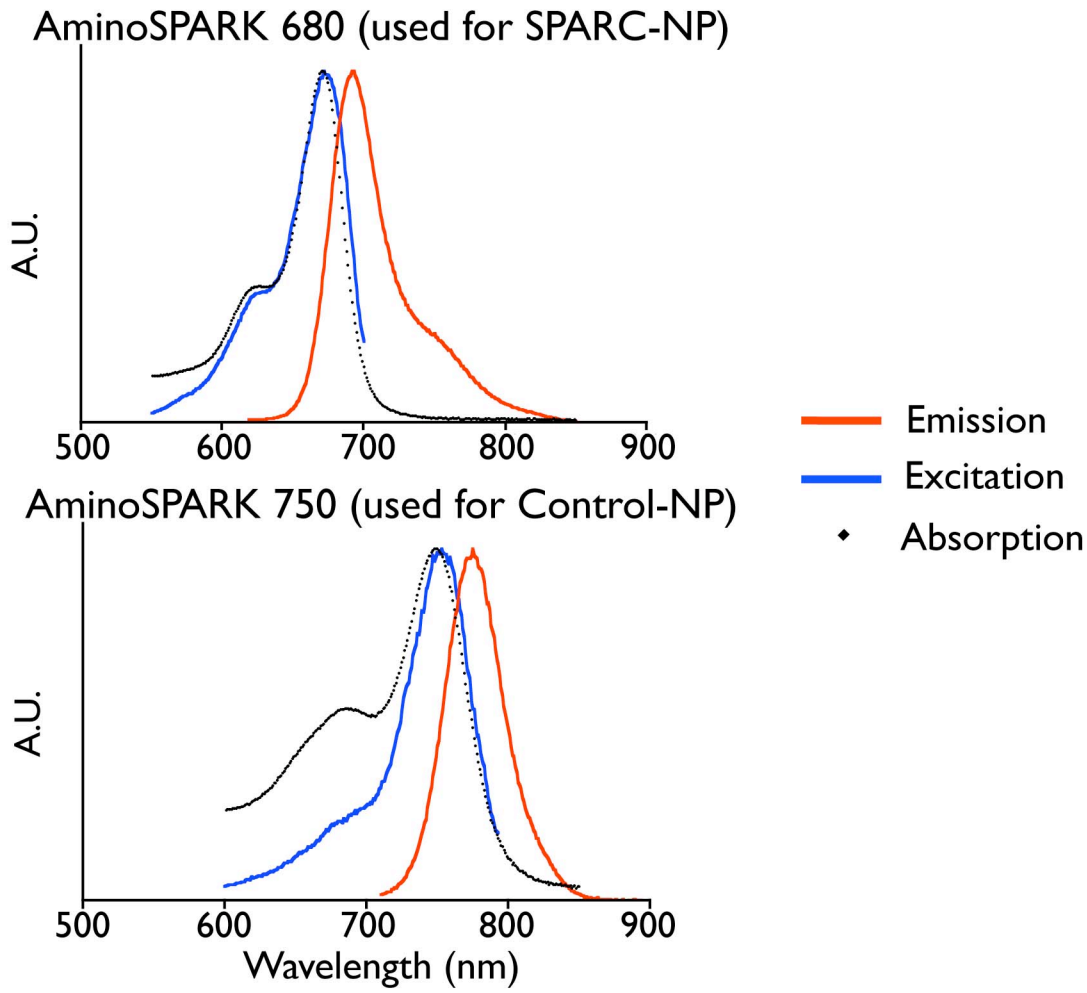

Figure 12. Emission, excitation, and absorption spectra of aminoSPARK 680 (top) and aminoSPARK 750 (bottom) nanoparticles.

One of the main determinants of how a nanoparticle is trafficked in vivo is its size and shape.[10] TEM of the aminoSPARK nanoparticles was used to examine the core size (Figure 13), and both dynamic light scattering and tapping mode AFM was used to examine the size and shape of the polymer coating (Figure 13).

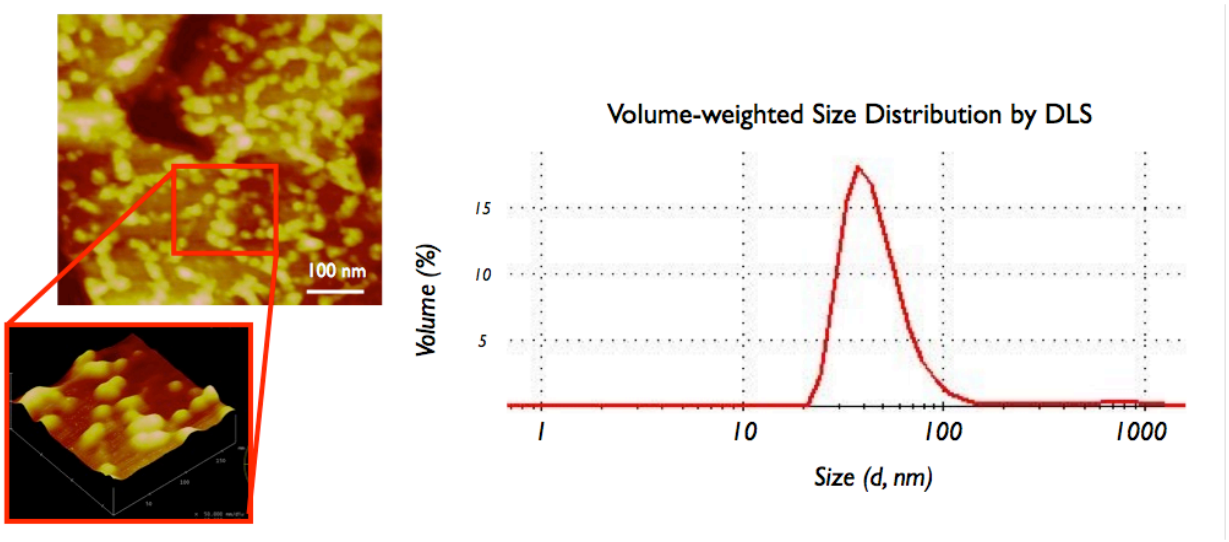

Figure 13. Hydrodynamic size and morphological characterization of the aminoSPARK nanoparticles. Left: Tapping AFM image of aminoSPARK nanoparticles on Au on mica. Right: Volume-weighted hydrodynamic size is determined to be 54 nm by dynamic light scattering of aminoSPARK nanoparticles.

TEM images of the nanoparticles reveal a mean core diameter of 8.75 nm with a standard deviation of 2.49 nm, and the AFM height images show spherical nanoparticles of about 20-30 nm in size. Light scattering assesses the size of the polymer-coated nanoparticle in solution, which were determined to be 54 nm in diameter. The difference in diameters between the AFM measurement and the light scattering measurement could be due to a combination of swelling of the polymer coating in solution during the light scattering measurement, and compression of the polymer coating during the tapping mode AFM measurement.

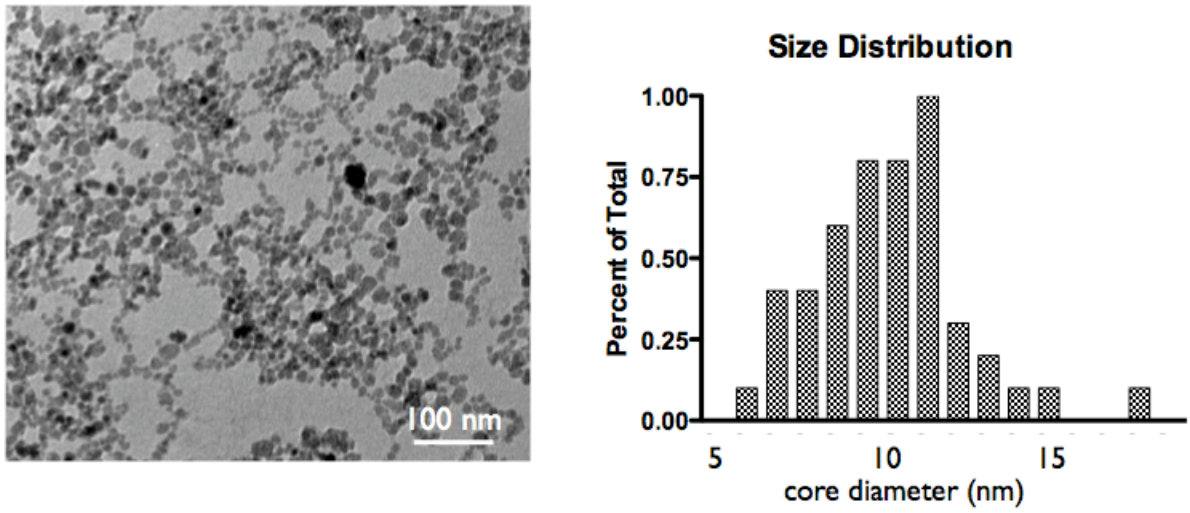

Figure 14. TEM of aminoSPARK nanoparticles. Left: TEM micrograph of aminoSPARK nanoparticles revealing the iron core of the nanoparticles to be approximately 9 nm. Right: Size distribution of nanoparticle cores (long diameter) as measured by ImageJ and by hand.

The field-dependent magnetic behavior of the nanoparticles was assessed using a superconducting quantum interference device (SQUID) magnetometer (Figure 15) and compared with the reference nanoparticle CLIO. The weight percent of iron in the solid aminoSPARK sample was determined to be 10.5% by a colorimetric iron assay, and using this information the magnetic response of the nanoparticles has been normalized to grams of iron. When no field is applied the iron oxide crystallites that act as magnetic domains are randomly aligned, resulting in a net magnetization of zero. At the relatively high magnetic fields used in this study there is no evidence of saturation, hysteresis or remanence in the aminoSPARK nanoparticles, meaning that the magnetic domains do not remain aligned after the field is removed. The linear dependence of the aminoSPARK nanoparticles' magnetization on the magnetic field and the low magnetization values indicate that a few domains align with the applied field but the majority of the domains do not. The aminoSPARK nanoparticles are thus paramagnetic, unlike the highly superparamagnetic CLIO, and would not have high enough contrast to use for magnetic

resonance imaging (MRI). However, they are still well-suited for fluorescence imaging applications.

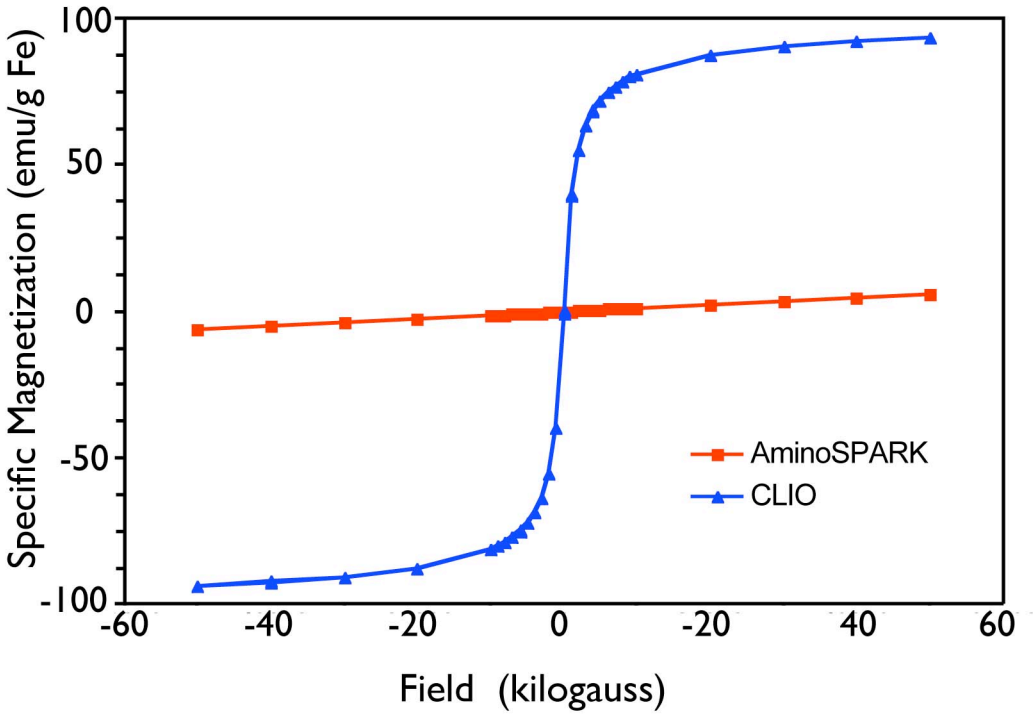

Figure 15. Magnetic characterization of AminoSPARK nanoparticles at 298K reveals their paramagnetic behavior. Magnetization measured on a SQUID magnetometer of reference superparamagnetic CLIO nanoparticles (blue) and paramagnetic aminoSPARK nanoparticles (red).

X-ray Diffraction (XRD) was performed to investigate the chemical makeup and organization of the core of the nanoparticle (Figure 16). The broad hump in the XRD spectrum indicates that the nanoparticles consist of either amorphous material or a coalescence of extremely small crystallites, which is in contrast with the other nanoparticles described in this work (see Table 1). The lack of crystallinity displayed in the XRD spectrum of aminoSPARK explains that lack of coupling of magnetic moments as shown in the M-H curve in Figure 15.

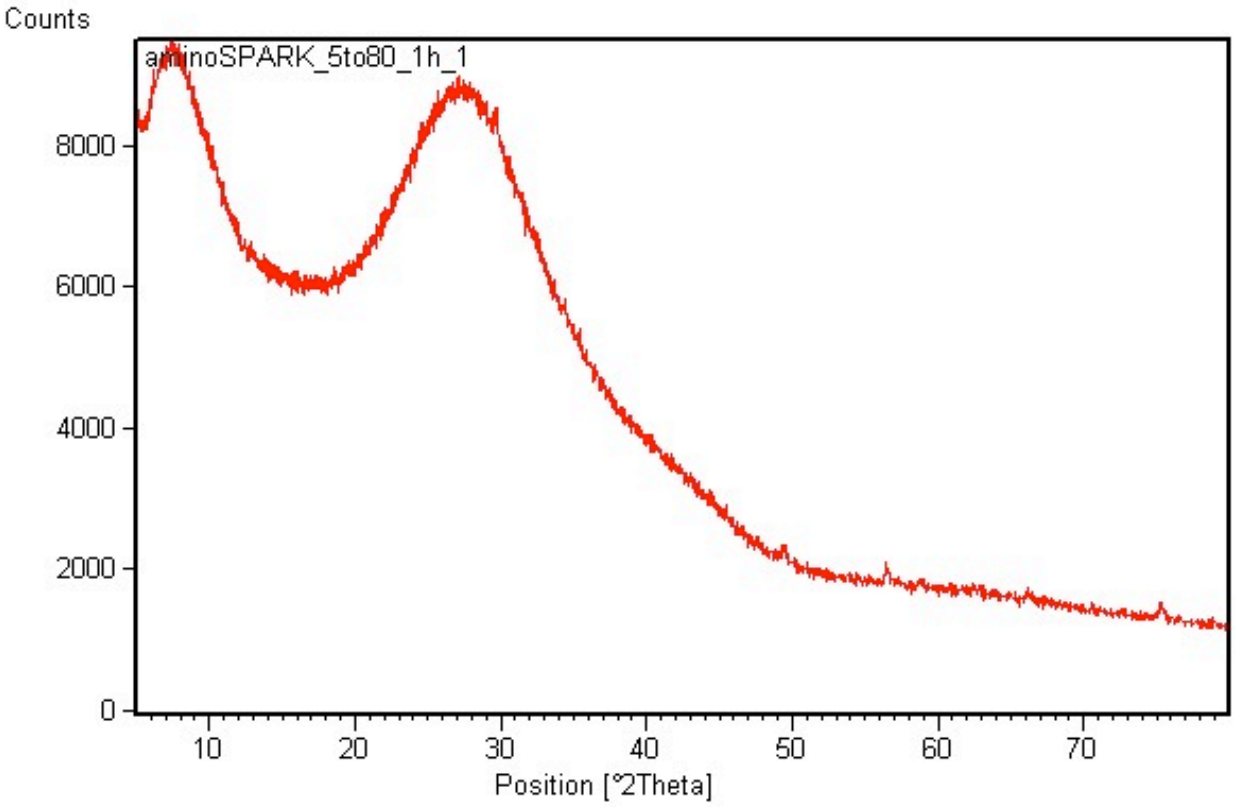

Figure 16. Powder XRD pattern of aminoSPARK nanoparticle shows lack of crystalline structure of the iron oxide core.

In vitro cell uptake assays were used to determine specificity of the imaging agent for SPARC expression (Figure 17, left). The EC_{50} of the SPARC-NP to SPARC expressing cell lines was in the hundred nanomolar range, while the EC_{50} of the SPARC-NP to SPARC-negative cell lines was extremely high. By contrast, the Control-NP exhibited negligible binding to both cell types. Flow cytometry data for SPARC-expressing and SPARC-negative cell lines incubated in 1 μM of SPARC-NP is shown in Figure 17 (right) and indicate that conjugation of the SPARC targeted peptide to the nanoparticle did not affect the peptide's specificity.

Cell Line	Compound	EC50 (nM)	Specificity
SPARC +	SPARC-NP	321.7	NA
SPARC +	Control NP	103,936	322.8
SPARC -	SPARC-NP	12,966	40.4
SPARC -	Control NP	8,446	26.2

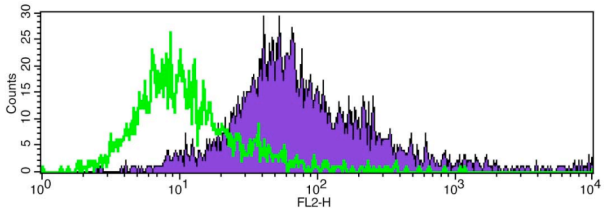

Figure 17. Flow cytometric analysis of SPARC-targeted aminoSPARK nanoparticle incubated with SPARC-expressing and non-SPARC expressing cell lines shows specificity of SPARC-NP for SPARC-expressing cell lines. EC50 values of SPARC-targeted (SPARC-NP) and non-targeted nanoparticles (Control NP) (left). Histogram showing cell data of targeted (purple) and non-targeted nanoparticles (green) (right).

In Vivo Studies

Tumor xenografts were grown in the flanks of Scid mice and SPARC-NP was injected to visualize the tumors using FMT and CT. Control-NP was co-injected to control for differences in tumor volume, vascularity, and other differences. The preliminary data in Figure 18 shows increased uptake of the SPARC-NP in SPARC-expressing tumors.

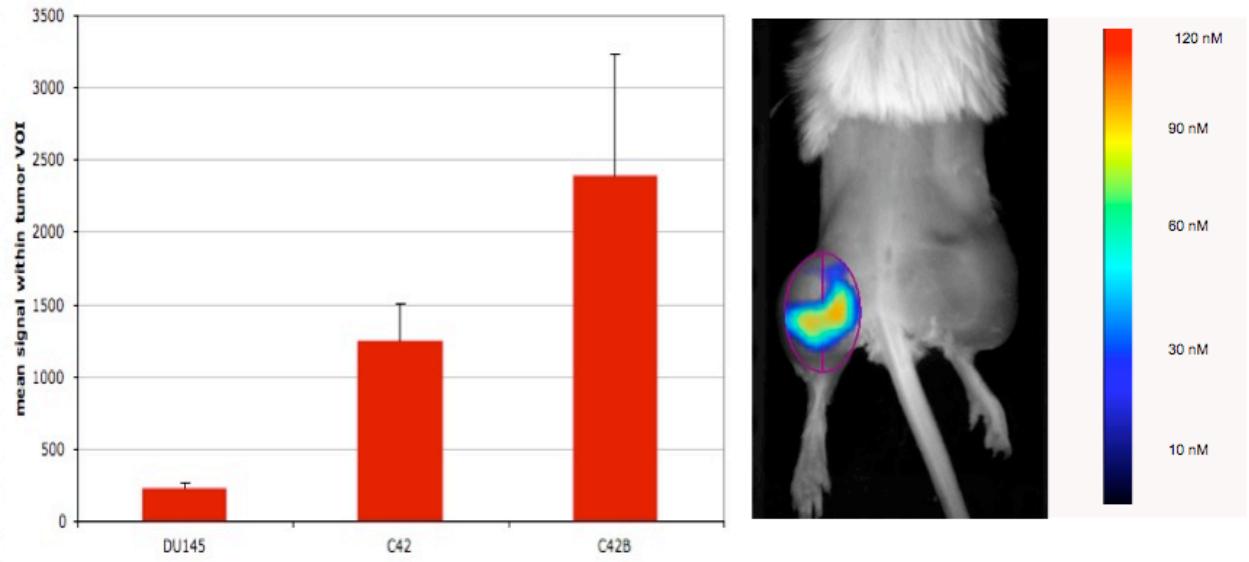

Figure 18. Imaging of SPARC in tumors using SPARC-NP. Left: tumors expressing SPARC preferentially take up the SPARC-NP over tumors that do not express SPARC. Right: example image of a visualized SPARC-expressing tumor. Imaging and injections performed by Peter Waterman.

4.8 Conclusion

Prostate cancer affects millions of men worldwide and the current methods of prognostication are inaccurate. Because physicians are unable to rely on the biopsy specimen to accurately reveal the tumor's underlying aggressiveness, many men undergo the most invasive form of treament, radical prostatectomy, which is often unnecessary.[107] In order to solve this clinical dilemma, we successfully developed a multimodal nanoparticle that has the ability to stage prostate cancer non-invasively using imaging methods. Critically, this nanoparticle is able to both identify areas of prostate tumor and provide important biologic information; namely, the degree of SPARC expression.

The immunohistochemical results from the tissue microarrays show that SPARC expression in prostate cancer is present not only in the tumoral compartment but also in the

stromal and epithelial compartments surrounding the tumor. This result was expected as SPARC is a secreted matricellular protein and a known regulator of tumor-stromal interactions. Indeed this finding has been corroborated in several other tissue microarray studies as well.[108-112] Increased SPARC expression in tissue microarrays has been correlated with increased tumor metastasis,[113] and malignant prostate cancer has been shown to be induced by the stroma itself.[114]

The overall goal of this imaging nanoparticle is to reduce the number of unnecessary radical prostatectomies and, conversely, to ensure that highly invasive tumors are treated aggressively. Importantly, SPARC expression imparts prognostic information in other solid tumors as well and may become the target of future molecular therapeutics. Thus, the potential clinical applications of this novel imaging agent extends beyond prostate cancer to a variety of tumor types and therapeutic indications.

CHAPTER 5: A SCREENING PARADIGM FOR THE OPTIMIZATION OF POLYMER-COATED SUPERPARAMAGNETIC IRON OXIDE NANOPARTICLES

5.1 Summary

Polymer-coated superparamagnetic iron oxide nanoparticles have been used for a variety of biomedical applications, including as MRI contrast agents, for the treatment of iron anemia, and for ex-vivo cell labeling of cells used in cell-based therapies so that they can be tracked by MRI. In this project we describe a three-stage screening paradigm to develop high potency (i.e., high relaxivity), stable, polymer-coated superparamagnetic iron oxide nanoparticles. Each

screen examined different facets of the interaction between iron oxides and polymers. Polymers were first tested for their ability to iron oxide nanoparticles. The synthetic procedure was then optimized for each potential coating. Finally, nanoparticles were subjected to high temperatures as a final test of stability. A carboxymethyl dextran-coated superparamagnetic iron oxide nanoparticle (CMD-NP) with a transverse relaxivity (R_2) of 271 $mM^{-1}sec^{-1}$ and a diameter of 47 nm by dynamic light scattering was obtained. The CMD-NP is a polymer coated superparamagnetic iron oxide nanoparticle with improved relaxivity and high stability achieved without the crosslinking procedure used in the CLIO nanoparticle. The coating of this nanoparticle is similar to the Feraheme nanoparticle, which is used in Chapters 6 and 7.

5.2 Aims

The aim of this project was to design a screening paradigm for the optimization of polymer-coated iron oxide nanoparticles and use it to synthesize a stable, high relaxivity nanoparticle. The ultimate destination of the resulting nanoparticle would be the clinic, so efforts were made to use biocompatible methods and materials.

5.3 Introduction

The use of polymer-coated iron oxide nanoparticles as MRI contrast agents[13] for the treatment of iron anemia[115,116] and for ex-vivo cell loading and tracking by MRI[117, 118] suggests that the continued development and optimization of these materials could impact some or all of the various areas in which they have been used. Composed solely of iron oxide and a polymeric coating, polymer-coated iron oxide nanoparticles are currently the only magnetic NPs with a

well-understood and satisfactory toxicity, metabolism and elimination after injection into humans.

The association of dextran with iron oxide has led to its use as a coating for iron oxide nanoparticles for many decades.[116, 119, 120] However, dextran or nanoparticles made with dextran can cause anaphylactic reactions.[121, 122] A second limitation of dextran-coated iron oxides is the stability of the dextran coating, which may decrease when dextran is modified so that biomolecules can be attached. To achieve better stability, the dextran coating of iron oxide nanoparticles has been crosslinked with epichlorohydrin, to yield cross-linked iron oxide (CLIO). However, the cross-linking complicates nanoparticle synthesis and may impede the metabolism of the polymeric coating. Nevertheless, the stability and use in diverse applications makes the CLIO nanoparticle a useful reference material for these studies. A third limitation of dextran-coated iron oxides is their limited potency as MR contrast agents, where potency is expressed as their R_2 or transverse relaxivity. Newer nanoparticles have higher R_2s than the older formulations of dextran iron oxide nanoparticles.[45, 123]

The goals of the current research were to obtain non-dextran based, polymer coated iron oxide nanoparticles which had a high potency (high R_2) and which were highly stable. To accomplish these goals, three screening methods were used in series. First, an ion challenge stability method (Ion Challenge Screen) was used to assess the interaction between a polymer and surface of a non-polymer coated iron oxide. Second, a Synthesis Optimization Screen was employed. Using polymers selected from the Ion Challenge Screen, the ferric/ferrous ion ratios and the amounts of polymer per iron were varied. Finally, a heat stress test was performed to assess nanoparticle stability (Heat Stress Screen). Here, stability was challenged by heating NPs to 90°C for 30 minutes. Using these screens we obtained a highly stable carboxymethyl dextran-

coated nanoparticle (CMD-NP) with an R_2 of 271 $mM^{-1}sec^{-1}$, a diameter of 47 nm. A carboxymethyl polyvinyl alcohol-coated nanoparticle (CMPVA-NP) was also obtained, another useful nanoparticle for a variety of applications.

5.4 Experimental

Materials

All reagents were from Sigma-Aldrich (St. Louis, MO) except T-10 dextran, which was from GE Healthcare (Newark, NJ).

Syntheses

Carboxymethyl polyvinyl alcohol

To obtain carboxymethyl polyvinyl alcohol (CMPVA), 60g of polyvinyl alcohol (PVA, 6 kDa, Aldrich) was dissolved in 280 mL water with heating. After cooling to room temperature, 200 mL 50% (w/w) NaOH was added. Then 200 g bromoacetic acid in 100 mL water was added dropwise, keeping the temp below 35°C. After standing overnight, the solution was neutralized with 6N HCl. CMPVA was purified by precipitation from ethanol. The final CMPVA had 6.5 carboxyl groups per mole by titration.

Superparamagnetic iron oxide nanoparticles

Ion-stabilized superparamagnetic iron oxide nanoparticles were synthesized as described previously.[124] Briefly, 40 mL of 1M ferric chloride in 2M HCl was mixed with 10 mL of 2M ferrous chloride also dissolved in 2M HCl. This mixture was added to 500 mL of a 0.7M

ammonium hydroxide solution, and the gelatinous precipitate was isolated by centrifugation. This precipitate was then resuspended in aqueous 1M tetramethyl ammonium hydroxide. The resulting iron oxide particles were roughly 40 nm.

Carboxymethyl dextran nanoparticle (CMD-NP) synthesis

Based on our Ion Challenge and Matrix Optimization Screens, the following synthetic method was derived. 6.3 g of carboxymethyl dextran (10kDa, Sigma-Aldrich) was dissolved in 10 mL water, and the pH was adjusted to 3 using HCl. Ferric chloride (243 mg, 0.9 mmole) dissolved in 500 µL water was added to the CMD solution and cooled to 4°C. A freshly made ferrous chloride solution (180 mg, 0.9 mmole in 1.2 mL water) was added dropwise while stirring. Ammonium hydroxide (30%, 5 mL, 79 mmole) was added rapidly, and the resulting solution was heated to 75°C for 2 hrs. The resulting material was passed though a 0.22 µm filter and then ultrafiltered using a 300 kDa MW hollow fiber cartridge to remove unbound CMD.

Carboxymethyl polyvinyl alcohol nanoparticle (CMPVA-NP) synthesis

To obtain CMPVA coated nanoparticles, 37 g of CMPVA was dissolved in 750 mL water, filtered using a 0.7 µm glass fiber filter and cooled under nitrogen. Ferric chloride (1.86 mL, 7.6 mmole Fe) was added to the polymer solution while stirring and cooled to 4°C. Ferrous chloride tetrahydrate (1.02 g, 5.2 mmol) dissolved in 1 mL of degassed water was added to the cold mixture while stirring. Cold ammonium hydroxide (30%, 15 mL, 295 mmole) was then added dropwise while stirring, and the resulting solution was heated to 80°C over 20 minutes and then held at 80°C for one hour. The resulting material was filtered through successively smaller

filters (3 μm, 0.7 μm, 0.22 μm) and ultrafiltered using a 300 kDa MW hollow fiber cartridge to remove unbound CMD.

Screening methods

Ion Challenge Screen (Screen 1)

Ion-stabilized nanoparticles (100 μg Fe/mL, 200 μL) were added to a 96-well plate. Polymer (200 μg/mL) was added in varying volumes to the nanoparticles, followed by addition of 20μL of 4M NaCl. The plate was placed on a 96-well plate magnetic separator (Spherotech, Libertyville, IL) and the absorbance of each well was read at 405 nm with an EMax plate reader from Molecular Devices (Sunnyvale, CA).

Synthesis Optimization Screen (Screen 2)

Sixteen 1 mL solutions of 100 mg polymer were chilled down to 4°C with ice. Appropriate amounts of ferric chloride solution were added, and the solutions were degassed by bubbling nitrogen though them, while keeping the solutions chilled. Freshly made ferrous chloride solutions were added, followed by 0.75 mL of 30% ammonium hydroxide (4°C) added in a dropwise fashion. The solutions were then heated to 65°C while mixing for 2 hours, after which they were analyzed.

Heat Stress/Stability Screen (Screen 3)

Heat stress stability was determined by heating NPs (2 mg Fe/mL) at 90°C for 30 minutes. Stressed and non-stressed solutions were diluted to approximately 1-20 μg Fe/mL to

determine their size by dynamic light scattering and T2. Stability was defined by the constancy of size and T2, where changes of more than 10% were considered significant.

Characterization

Iron concentration was determined by dissolving 10 μL of the nanoparticle solution in 990 μL of 6N HCl with 3 μL of 30% hydrogen peroxide for one hour using ferumoxides as an iron oxide standard. R_1 and R_2 were measured at 0.47 T at 40 °C using a Bruker MiniSpec (Billerica, MA). The number of iron atoms per nanoparticle was determined by the viscosity/light scattering (VLS) method.[39] Size in solution was determined by dynamic light scattering (DLS) using a Zetasizer (Malvern Instruments, Marlboro, MA). Transmission electron microscopy (TEM) was conducted on a JEOL 2011 instrument at 200 kV. A dilute nanoparticle solution (in solutions of 1:1 water:ethanol or 1:1 water:100mg/ml dextran) was spotted onto a copper carbon film TEM grid (Electron Microscopy Sciences, Hatfield PA). Magnetization was determined using an AC and DC Superconducting Quantum Interference Device (AC/DC SQUID, Quantum Design, San Diego, CA) with a field scan range of ± 50,000 Oe at 298K. X-ray diffraction (XRD) studies used a Rigaku RU300 diffractometer (Tokyo, Japan). Crystallite size was determined from peak full width at half maximum (FWHM) using the Scherrer equation and a William-Hall plot. All analyses were performed in Jade software (Materials Data Inc., Livermore, CA).

5.5 Results and Discussion

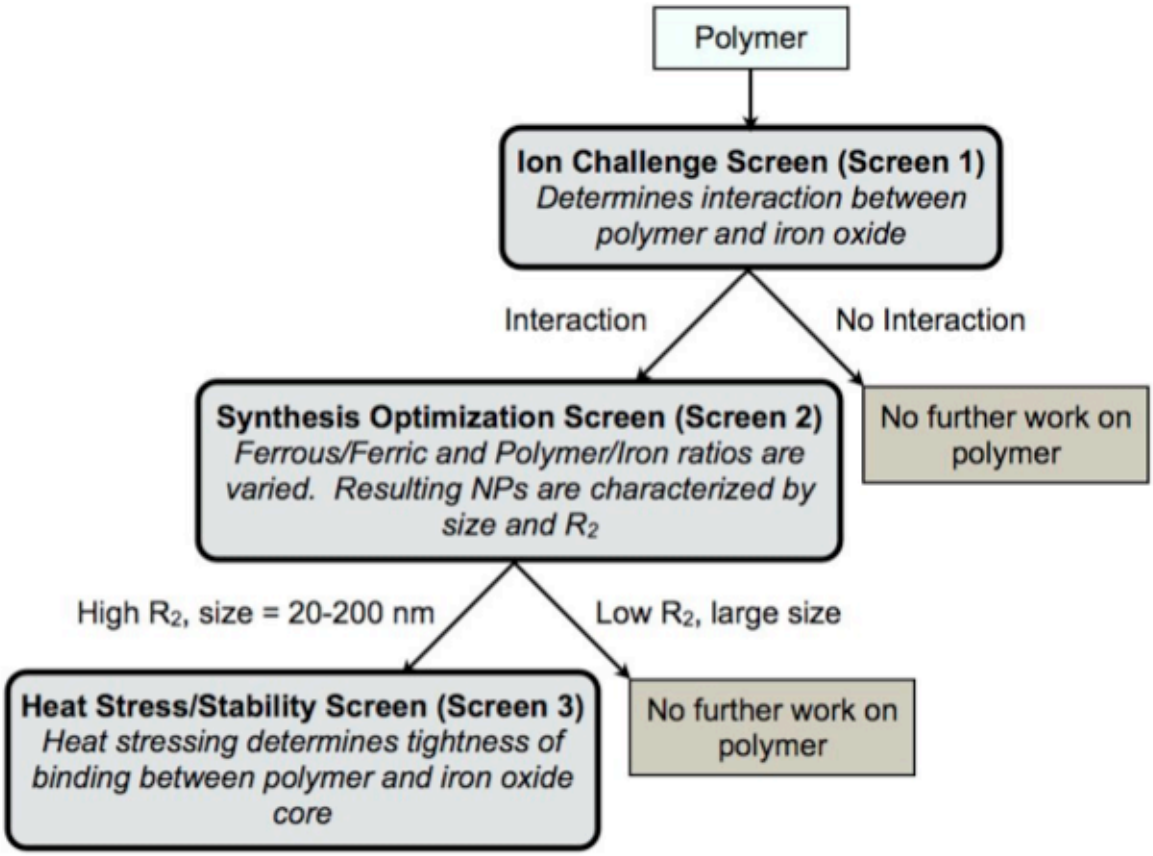

Figure 19. Flow scheme for polymer evaluation as coatings of iron oxides. The three screens employed were the Ion Challenge Screen (Screen 1), the Synthesis Optimization Screen (Screen 2), and the Heat Stress/Stability Screen (Screen 3).

The three-stage screening strategy to obtain a high potency, polymer-coated superparamagnetic iron oxide nanoparticle is summarized in Figure 19. A summary of the data obtained with the Ion Challenge Screen, the Synthesis Optimization Screen, and the Heat Stress/Stability Screen is provided in Table 2, where results from each screen are denoted as either negative (No) or positive (Yes).

Polymer	Screen 1: Ion Challenge	Screen 2: Synthesis Optimization	Screen 3: Heat Stress/ Stability
Cellulose acetate	No		
Carboxymethyl cellulose	No		
Chitosan	Yes		
Dextrin	Yes	No	
Dextran (T10)	Yes	Yes	No
Carboxymethyl dextran	Yes	Yes	Yes
Carboxymethyl guar gum	No		
Heparin	Yes	No	
Starch (soluble)	Yes	Yes	No
Starch	No		
Carboxymethyl starch	No		
Hydroxyethyl starch	Yes	Yes	No
Poly(acrylic acid)	Yes	No	
Poly(acrylic acid–maleic acid) copolymer	No		
Poly(methacrylic acid)	No		
Poly(butadience–maleic acid) copolymer	Yes		
Poly(ethylene glycol)	No		
Poly(ethylenimine)	No		
Poly(lactic acid)	No		
Poly(styrene sulfonic acid–maleic acid) copolymer	No		
Poly(vinyl alcohol)	No		
Carboxymethyl poly(vinyl alcohol)	Yes	Yes	No
Poly(vinylpyrrolidone)	No		
CLIO	Not applicable	Not applicable	Yes

Table 2. Summary of screening paradigm used to obtain high relaxivity, stable polymer-coated iron oxide nanoparticles.

Ion Challenge Screen (Screen 1)

This screen determines whether there is a strong or weak interaction between a polymer and an uncoated superparamagnetic iron oxide. The Ion Challenge Screen was based on the observations that (i) an ion-stabilized superparamagnetic iron oxide NP (diameter = 40 nm) precipitated when its charge-induced stability was challenged by the addition of NaCl, (ii) the addition of the polymer dextran resulted in stabilization of the ion-stabilized NP as shown in Figure 20A, and (iii) dextran-coated iron oxide NPs like MION or CLIO did not aggregate upon NaCl addition. Figure 20B shows the increase in size due to the formation of NP aggregates after addition of NaCl, where size was measured by laser light scattering. Increasing

concentrations of T10 dextran are also shown to antagonize the NaCl-induced size increase of the ion-stabilized NP (Figure 20B). We reasoned that it would be possible to develop a high-throughput screening version of the ion challenge method if NP size could be measured by absorbance rather than light scattering, since absorbance measurements can be readily performed in a microtiter plate format. We also reasoned that a side-pull magnet would attract large aggregates of NPs to the side of a vessel container, leaving dispersed NPs in solution (Figure 20C). As shown in Figure 20D, we employed a side pull magnetic separator to remove aggregated magnetic nanoparticles from 96-well microtiter plates, a situation which permitted 405 nm light to traverse the solution from the bottom of the well to the top. Increasing concentrations of T10 dextran, the positive control polymer, prevented NaCl-induced aggregation, maintained the dispersed state of the nanoparticle, and resulted in brown, light-absorbing solutions that reduced light transmission. The ability of the polymer to associate with and thus stabilize NPs was measured as absorbance after magnetic separation of aggregates. The microtiter plate format allows for the screening of large numbers of polymers in a parallel, high-throughput fashion.

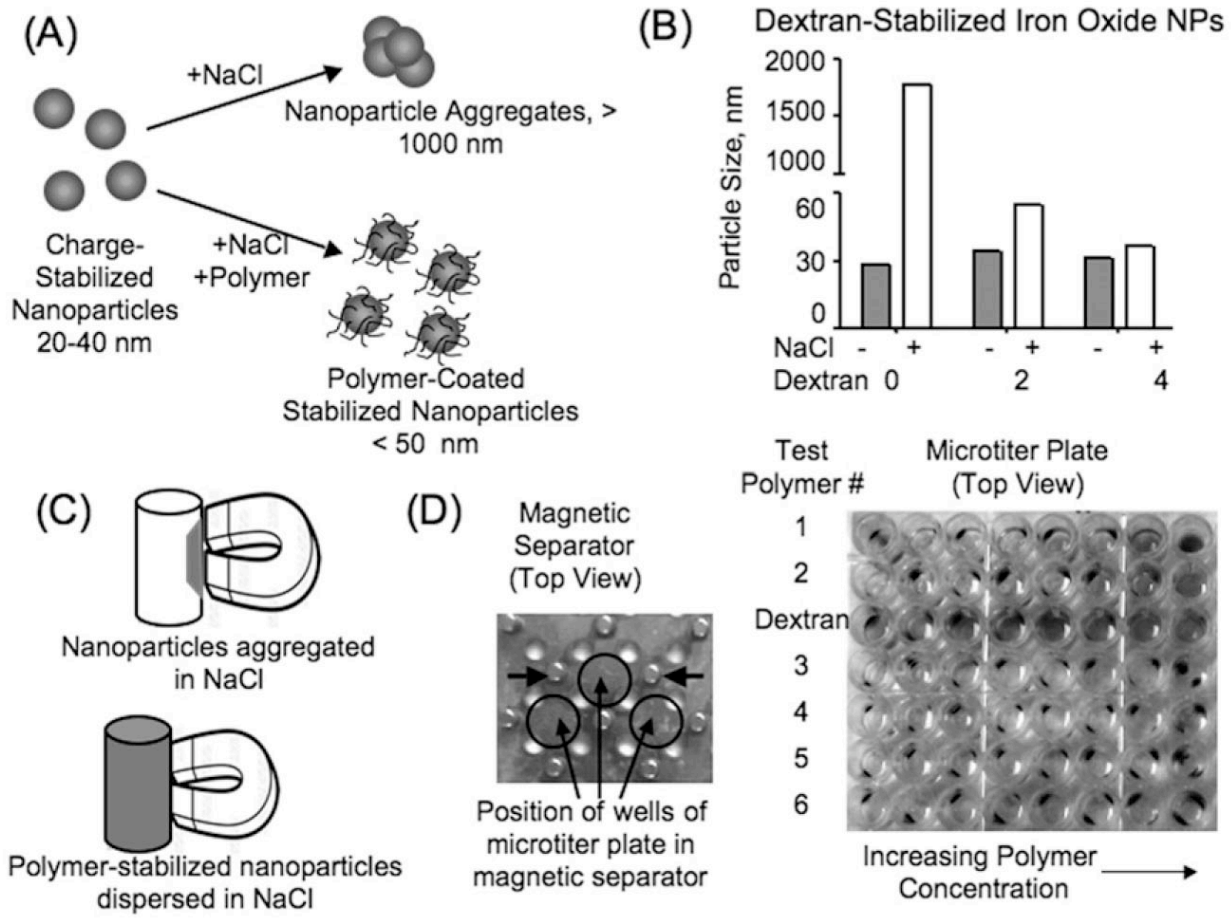

Figure 20. Description of Ion Challenge Screen (Screen 1). (A) A charge-stabilized iron oxide NP was prepared. Upon addition of NaCl it promptly aggregated. However, if a polymer that coats the surface of the NPs was also added, NaCl failed to aggregate the NPs. (B) Size increase seen upon addition of NaCl when no polymer was present and inhibition of aggregation (i.e., stabilization) upon addition of increasing concentrations of dextran. (C) Application of a magnetic field caused separation of the large, NaCl-induced nanoparticle aggregates. Smaller, polymer-coated, stabilized NPs were not separated out of solution by the magnetic field. (D) Adaptation of the method shown in (A)-(C) to a high-throughput, microtiter plate screening format. Charge-stabilized NPs and NaCl were added to wells with increasing concentrations of six different test polymers. A side pull magnetic separator was employed to move NaCl induced aggregates, with results were read visually or on plate reader. Horizontal arrows on the magnetic separator denote the positions of the magnets.

Synthesis Optimization Screen (Screen 2)

This screen determines whether those polymers that associated with superparamagnetic iron oxides in the Ion Challenge Screen (described above) can be used in a synthesis of polymer-coated superparamagnetic iron oxides. The need to create a matrix of varying synthetic reactions reflects the fact that there is no single procedure for synthesizing polymer-coated iron oxides that

can be used to evaluate chemically diverse polymers. The general synthetic method used was based on our synthesis of MION; here polymers and iron salts were mixed and cooled to less than 10°C, base was added, and the mixture was heated to 60-80°C. The R_2 and size of the NPs were then determined without the removal of excess polymers, since both R2 and dynamic light scattering (DLS) measurements are performed at low concentrations of iron and polymer. Polymers and syntheses giving high R_2s (greater than 100 $mM^{-1}sec^{-1}$) and small particle size (20-100 nm) had excess polymers removed by ultrafiltration, and the syntheses with optimal conditions for a given polymer were repeated three times (Figure 21).

Several polymers that passed the Ion Challenge Screen (thus showing that they interacted with iron oxides) formed insoluble mixtures during acidic or basic conditions of the Synthesis Optimization Screen and were rejected (e.g., dextrin, polyacrylic acid and heparin). Polymers that produced NPs with sizes (by DLS) between 20 to 200 nm and R_2s greater than 50 mM^{-1} sec^{-1} were starch, carboxymethylpolyvinyl alcohol (CMPVA), hydroxyethylstarch (HES) and carboxymethyl dextran (CMD) (Table 2).

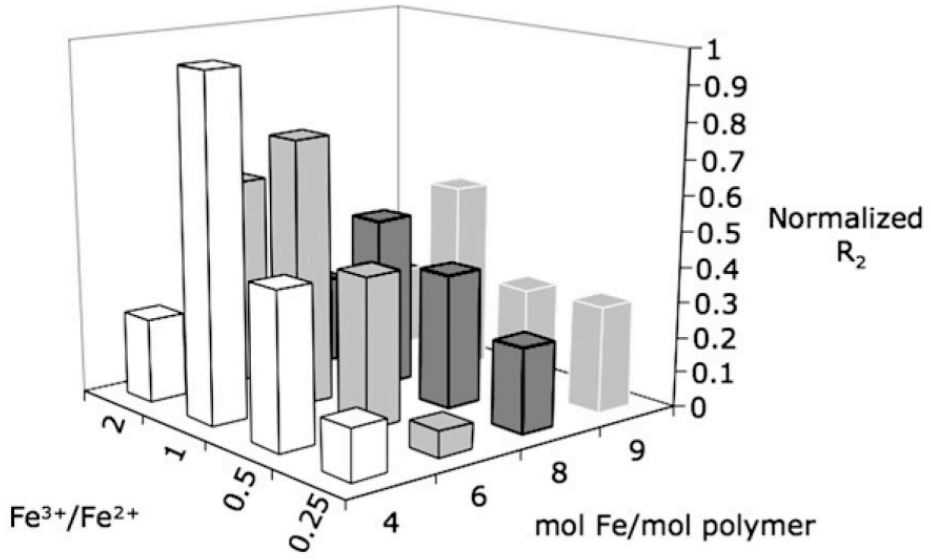

Figure 21. A typical Synthesis Optimization Screen (Screen 2) for determining whether polymers can yield high R_2 nanoparticles. The ratio of ferrous to ferric iron and ratio of polymer to iron were varied to determine the combination yielding the highest R_2.

Heat Stress/Stability Screen (Screen 3)

Nanoparticles that passed the Synthesis Optimization Screen were then tested for stability using a heat stress method, which provided a measure of tightness of binding between the polymer and the surface of an iron oxide. The attachment of biomolecules to the polymer coating, a necessity for many of the intended applications of these polymer-coated nanoparticles, requires very tight binding. Of all the NPs assessed in this study, only the CMD-NP displayed a satisfactory stability upon heat stress. The heat stress employed (90°C for 30 minutes) was extreme, though the crosslinked dextran-coated CLIO, which served as our positive control nanoparticle, had been shown to pass this test. Although the CLIO nanoparticle, widely used for biomolecule-based targeting applications,[125-128] possesses the required heat stress stability, it achieves that stability by crosslinking the polymeric dextran, which complicates the

manufacturing process and may affect the elimination of the dextran after injection *in vivo*. Based on our screens, the carboxymethyl dextran-coated nanoparticle CMD-NP was the best choice for future studies using polymer-coated iron oxide nanoparticles. The carboxymethyl polyvinylalcohol-coated nanoparticle, CMPVA-NP, was also a good choice due to its small size and high relaxivity, for although it failed the extreme conditions of our Heat Stress Screen it might prove satisfactory in many applications where sustained exposure to high temperatures is not required.

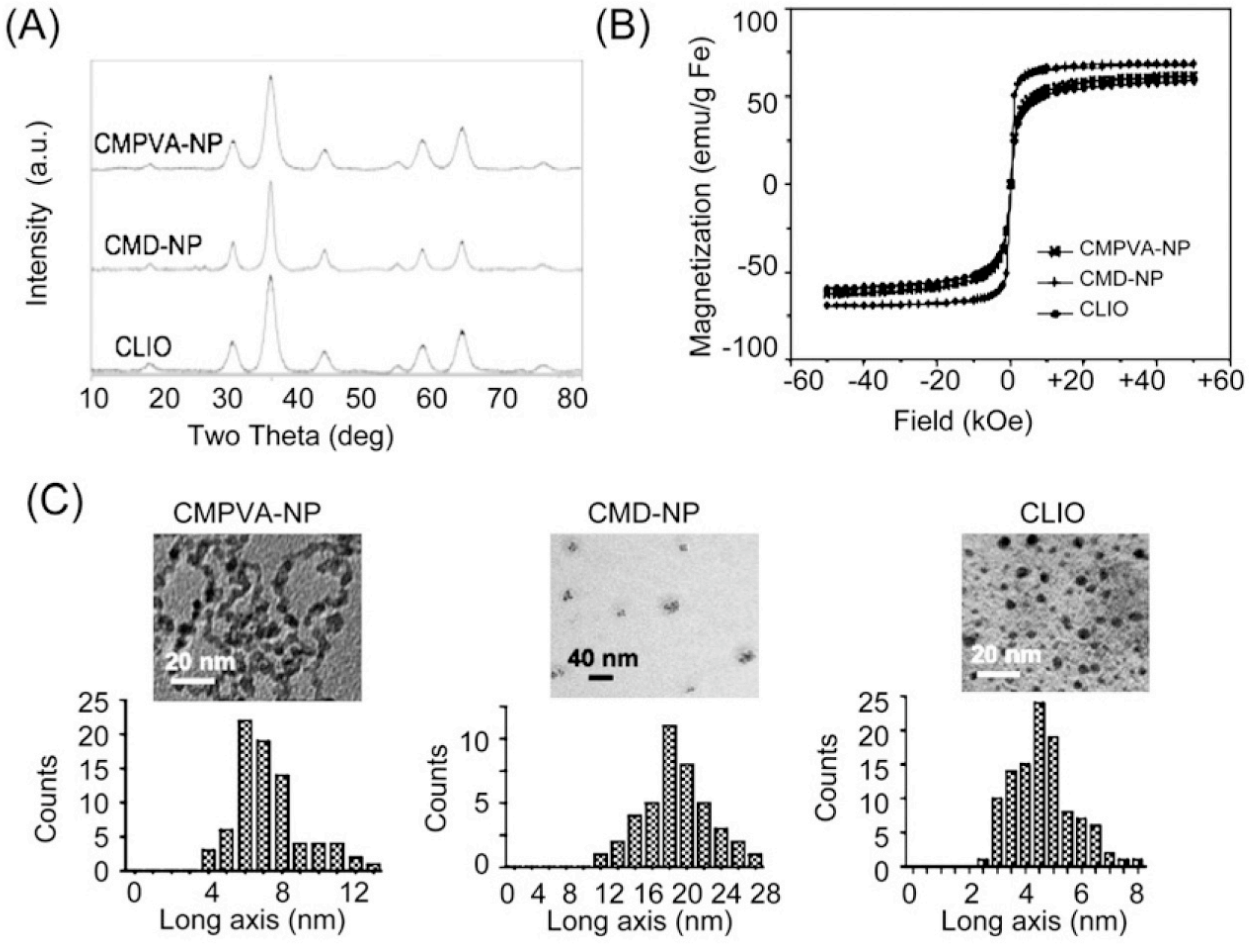

Figure 22. Characterization of nanoparticles. (A) Diffraction patterns for CLIO, CMPVA-NP and the CMD-NP. All were composed of magnetite and/or maghemite. (B) Magnetization of the CMPVA-NP, CMD-NP, and CLIO NPs. Saturation magnetizations of CMPVA-NP, CMD-NP, and CLIO were 62, 68, and 59 emu/g Fe respectively. (C) TEM micrographs of NPs and histograms for the CMPVA-NP, CMD-NP and CLIO, Mean sizes were 7.2 ± 1.9 nm, 18.9 ± 3.8 nm, and 4.6 ± 1.0 nm (±1 SD), respectively.

The magnetic properties and sizes of CMD-NP and CMPVA-NP, along with a CLIO reference, were characterized in Figure 22 with values summarized in Table 3. Notable is the fact that CMD-NP had a higher R_2 than CLIO or CMPVA-NPs, consistent with its substantially larger size by all sizing methods. Outer relaxation sphere theory predicts that as NP size increases R_2 increases; for a discussion see Hong et al.[129]

Table 3: Physical Properties of Polymer Coated Superparamagnetic Iron Oxide Nanoparticles

NP	Polymer coating	Diameter, DLS, (nm)	R1 (mmole /sec)$^{-1}$	R2 (mmole /sec)$^{-1}$	VLS (Fe/NP), (nm)	XRD (nm)	TEM (nm)	Saturation Magnetization (emu/g Fe)
CLIO	Cross-linked dextran	29.8*	23.1*	54.9*	8000,** 3.6	4.7	4.6 ± 1.0	62
CMD-NP	Carboxymethyl dextran	47.0 ± 4.6 ***	16.0 ± 5.8 ***	271 ± 26 ***	62000, 14.2	10.7	18.9 ± 3.8	68
CMPVA-NP	Carboxymethyl polyvinyl alcohol	37.1 ± 1.4 ***	47.3 ± 2.6 ***	119.2 ± 2.4 ***	8900, 3.7	5.1	7.2 ± 1.9	59

Table 3. Physical properties of polymer-coated superparamagnetic iron oxide nanoaprticles obtained by the screens, compared with the reference NP CLIO. *** Values shown indicate means and standard errors from at least three syntheses. * from reference 5, ** from reference 39.

The sizes of CMD-NP, CMPVA-NP and CLIO were characterized by four different methods that employ widely different physical assumptions in their calculations. They were transmission electron microscopy or TEM, X-ray diffraction or XRD, viscosity/light scattering or VLS and dynamic light scattering or DLS. DLS provides the size of NPs in solution, inclusive of the polymeric coating and independent of the size and nature of the iron oxide core, which can be polycrystalline or monocrystalline. DLS also provides information on the

distribution of sizes in solution, i.e., the polydispersity. All three NPs examined had size distributions typical of monodisperse MION and CLIO reference materials, with polydispersities less than 0.5 as calculated by the software provided on the Malvern Zetasizer DLS instrument. (An example of polydisperse NPs with widely varying sizes by light scattering is ferumoxides.[4]) XRD provides information on the chemical nature of the crystalline core and the size of the core crystals, irrespective of whether they are present as monocrystalline or polycrystalline NPs in solution. The peaks seen with XRD indicated all three cores could be either gamma ferric oxide (γ-Fe_2O_3) or magnetite (Fe_3O_4), which give similar XRD patterns with small crystals. The superparamagnetic iron oxide cores of NPs are therefore termed "non-stoichiometric magnetite," with an oxygen ratio between that of magnetite and γ-ferric oxide.[4] Crystallite size was estimated from the peak widths using the Williamson-Hall equation

$$B(2\theta) = \frac{K\lambda}{L\cos\theta}$$

where K is the Scherrer constant, λ is the wavelength of the X-rays, and L is the peak width, while deconvoluting broadening effects due to the instrumental profile and microstrain.

TEM provides a measure of iron oxide core size, with polycrystalline cores giving larger values than monocrystalline cores. Thus, the larger core size of the CMD-NP as determined by TEM compared to the core size as determined by XRD indicated the CMD-NP was polycrystalline. However, the width of distribution of CMP-NP (standard deviation = 3.8 nm) relative to its mean (18.9 nm) was no broader than that of the monodisperse CLIO (mean = 4.6, standard deviation = 1.0 nm). In addition, the polydispersity of CMD-NP by DLS was less than 0.5 and typical of monodisperse materials (see above). Thus, the CMD-NP featured a

polycrystalline core with size distributions by TEM and DLS typical of homogeneous, monodisperse materials.

Our viscosity/light scattering (VLS) method uses the partial volume of particles in solution from viscosity measurements and the NP volume from dynamic light scattering (DLS) to obtain the number of iron cores in solution at a given iron concentration. VLS results were first expressed as the numbers of iron atoms per NP. Then, using the assumption that the iron oxide core was magnetite (Fe_3O_4, MW =232, density = 5.21 gm/cc), and the equation for the volume of a sphere (Volume = $4/3\pi r^3$), the diameters of the iron oxide cores were determined (Table 3). Very similar diameters from the VLS method were obtained if the iron oxide was assumed to be γ-Fe_2O_3. It can be seen that the diameters from the VLS and TEM methods were comparable. Unlike TEM, VLS provides a measure of NP core size based on the behavior of NPs in solution.

A variety of screening approaches have been used to select and optimize NPs and polymers for biological applications. Our screens were designed to measure different facets of interactions of polymers with the surfaces of iron oxides, with the goal of determining an "ideal" polymeric coating for a superparamagnetic iron oxide NP. A screening approach with a similar objective, i.e. obtaining molecules that bind to an inorganic surface, employed phage display to obtain the sequences of high affinity, surface-binding peptides (this method is described in more detail in Section 4.3.1).[130, 131] Other NP- and polymer-based screening approaches employ bioactivity rather than the affinity for surfaces to evaluate their individual synthetic components. In this bioactivity-based screening approach, NPs have been modified with a variety of different functional groups, and screened for their selective interactions with different types of cells.[132] A

different bioactivity screening approach employed a library of polymers and screened for their ability to assist in gene transfection.[133]

It should be noted that our work involves optimizing the properties of NPs that are comprised solely of a polymeric coating and core of iron oxide. A variety of other approaches can be employed to obtain high R_2 NPs, such as using metals other than iron in the design of metal oxides.[123] Another approach is the use of metallic iron in the design of NPs, since metallic iron has a higher saturation magnetization than the oxides of iron. However, metallic iron is susceptible to oxidation by oxygen. Furthermore, as noted above polymer coated iron oxide NPs have a uniquely broad history of safe clinical use for a variety of applications.

5.6 Conclusion

We describe a three-step screening paradigm for obtaining potent, stable, non-crosslinked polymer coated, superparamagnetic iron oxide nanoparticles. Our screens resulted in the development of a carboxymethyl dextran coated nanoparticle (CMD-NP) that featured a high R_2 and very high stability. CMD-NP had a polycrystalline core but had a range of sizes by DLS and TEM that was typical of the monodisperse reference nanoparticle CLIO. Thus CMD-NP is an example of a highly uniform, highly stable, polycrystalline material. Its biocompatible components make it an ideal NP for biomedical applications, and its superparamagnetic nature lends itself to MR imaging applications. Its coating can provide options for bioattachment of biomolecules for targeting and reporting, but it is unclear whether the carboxy groups in the coating are interacting with the iron oxide core or are actually free for conjugation.

CHAPTER 6: BIOCONJUGATION STRATEGIES TO FERAHEME, A COMMERCIALLY AVAILABLE FDA-APPROVED SUPERPARAMAGNETIC IRON OXIDE NANOPARTICLE

6.1 Summary

The discontinuation of the widely used iron oxide nanoparticle Feridex has left many researchers without a commercially available superparamagnetic polymer-coated iron oxide nanoparticle with which to perform a wide variety of experiments, from cell labeling to targeted

in vivo imaging. In Chapter 5 it was determined that carxboxymethyl dextran is an ideal coating for iron oxide nanoparticles in order to achieve both stability and high relaxivity. The commercially available nanoparticle Feraheme is coated with a carboxymethyl dextran and has excellent magnetic properties for imaging. In this project, we outline a procedure for modifying purchased Feraheme into an amine-functionalized version of Feraheme called amino-FH, which has at least 4-6 amine groups available for bioconjugation. All of the reagents used are readily available and relatively inexpensive. Fluorescent Ferahemes introduced here include rhodamine-conjugated Feraheme FH-Rho and Cy5.5-conjugated FH-Cy5.5, each with 3-5 fluorophores/nanoparticle. The multifunctional single-attachment point (MSAP) reagent DTPA Lys(CyAl5.5)-Cys(NHS) that was developed by Garanger et al.[134] was also successfully conjugated to Feraheme.

6.2 Aims

The aim of this work was to chemically modify Feraheme into a versatile nanoparticle platform. Free amine groups are one of the most common routes for bioconjugation, and are widely used for their linkage stability and their reactivity in aqueous solutions. Furthermore, amine groups are present on proteins, and the decades of work that have been put into developing bioconjugation strategies to proteins and antibodies can be applicable to the amine-functionalized Feraheme (amino-FH). A variety of versions of Feraheme are created by conjugating ligands to amino-FH, showing that it is a versatile platform nanoparticle for a variety of applications.

6.3 Experimental

Reagents included Feraheme (AMAG Pharmaceuticals, Lexington, MA), the NHS ester of tetramethyl rhodamine (Molecular Probes, Eugene, OR), and clinical injectable protamine sulfate (American Pharmaceutical Partners, Schaumburg, IL). Other chemicals were from Sigma-Aldrich (St Louis, MO). Separations used PD-10 columns (GE Healthcare, Piscataway, NJ) and 100 kDa NMWL Amicon centrifugal filter units (Catalog # UFC910024 Millipore, Billerica, MA). Light scattering and zeta potential was measured with a Nano-ZS zetasizer (Malvern, Medford, MA). Relaxivity measurements used a 20 MHz MiniSpec (Brucker Systems Billerica, MA). DTPA Lys(CyAl5.5)-Cys(NHS) was synthesized by Dr. Hushan Yuan (Center for Translational Nuclear Medicine and Molecular Imaging, Massachusetts General Hospital).

Concentration Determination

Iron and fluorescent conjugate concentrations were determined spectrophotometrically using 94,000 L/ml-cm as the extinction coefficient for rhodamine at 555 nm,[135] 157,000 L/ml-cm as the extinction coefficient for CyAl at 674 nm, and 250,000 L/ml-cm as the extinction coefficient for Cy5.5 at 678nm.

Synthesis of amino-FH

Feraheme nanoparticles were incubated with 3.72 mol ethylene diamine per mol iron, 0.49 mol 1-Ethyl-3-[3-dimethylaminopropyl] carbodiimide hydrochloride (EDC) per mol iron, and 0.21 mol hydroxybenzotriazole (HOBT) per mol iron in 0.1M MES buffer pH 6.0 for 1.5 hours at 50°C. In a typical reaction, 6 mg Fe of FH was reacted with 1 mg EDC and 0.2 mg

HOBT, then reacted with 40 ul of 1M ethylene diamine dihidrychloride solution, and purified using a PBS PD-10 column. Amino-FH was stable at 4°C for months.

Synthesis of FH-based materials

Amino-FH was reacted with an excess of Rhodamine NHS ester, NHS Cy5.5, DTPA Lys (CyAl5.5)-Cys(NHS), overnight at 4°C, a typical reaction using 6 mg Fe of amino FH and 1 mg of Rhodamine NHS ester (0.018 mol rhodamine/mol iron). To make ProRho-FH Amino-FH (6 mg) was reacted with EDC (1 mg, 0.48 mol per mol Fe), NHS (0.2 mg, 0.21 mol per mol Fe), and an excess of ProRho (1 mg) at 70°C for 30 minutes. Unreacted reagents were removed by filtration with a 100,000 NMWL cutoff Amicon spin column, eluting with PBS several times until the eluent runs clear.

Characterization

Nanoparticles were exchanged by dialysis into 5 mM Tris buffer pH 7 and characterized by zeta potential. Light scattering and absorbance measurements were performed in PBS. R1 and R2 were determined by measuring the T1 and T2 using a 0.47 T minispec at a range of concentrations.

6.4 Results and Discussion

Polymer coated superparamagnetic iron oxide nanoparticles have served as the basis for clinically useful MR contrast agents,[13, 136-138] for the treatment of iron anemia,[116, 139] for the design of targeted pre-clinical targeted MR contrast agents,[125, 132, 140] and for ex-vivo labeling and

cell tracking by MR.[126, 141, 142] Examples of polymers employed as nanoparticle (NP) coatings include dextran, carboxymethyldextran, carboxydextran and many others. A variety of conjugation chemistries have been developed to attach biomolecules to the hydrophilic polymeric coatings of such NPs including crosslinking, amination and reductive amination.

The Feraheme nanoparticle (FH), also known as ferumoxytol (AMI-228), was recently (June 30, 2009) FDA approved for iron anemia treatment and targeted at patients with chronic kidney disease (CKD). It has a molecular weight of 731 kD and a hydrodynamic diameter of 30 nm and its chemical formula is $Fe_{5874}O_{8752}$-$C_{11719}H_{18682}O_{9933}Na_{4142}$. One of the advantages of FH over other iron oxide NP formulations is that there is very little free iron present, allowing large amounts of it to be injected (510 mg of FH has been administered safely in as little as 17 seconds for a rate of 30 mg/sec) at a rate faster than other available injectable irons. Since FDA guidelines are very stringent we consider amino-FH to be a very safe material.

The coating of FH consists of a carboxylated polymer very similar to the CMD-NP described in Chapter 5. Although the coating of the Feraheme contains a number of carboxy groups it is not initially clear how many are available for bioconjugation and how many are on the inner part of the coating, interacting with the iron oxide core. We found here that while many of these carboxy groups are interacting with the iron core and thus not exposed, there are sufficient free carboxy groups for modification.

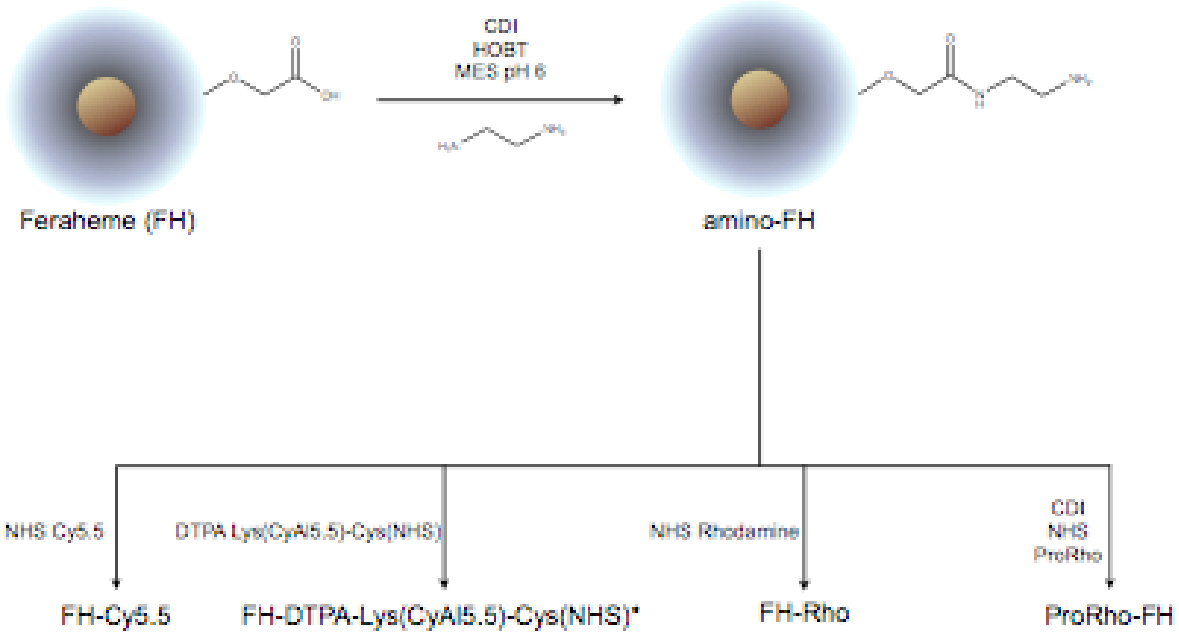

Figure 23. Schematic of synthesis of amino-FH and conjugation of various molecules to create new functionalities for FH.

Amino-FH was made by conjugating ethylene diamine to the free carboxyl groups on the Feraheme nanoparticle using CDI chemistry, and a schematic of this reaction is shown in Figure 23. The presence of amine groups was verified by conjugation to various molecules with NHS esters, and the confirmation that these amine-reactive molecules do not spontaneously associate with regular Feraheme, which does not contain amine groups. Amino-FH is highly stable, and can be stored at 4°C for months. The creation of this amine-functionalized version of Feraheme is extremely useful because it opens up many strategies for bioconjugation of a variety of amine-reactive molecules to the Feraheme nanoparticle. By modifying Feraheme to form amino-FH and using it as a versatile superparamagnetic nanoparticle platform, many types of fluorescent and multifunctional Ferahemes have been synthesized.

Nanoparticle	Source	Hydrodynamic diameter (nm)	Core diameter (nm)	Core # Fe	R1 ($mmol^{-1}$ sec^{-1})	R2 ($mmol^{-1}$ sec^{-1})	Zeta Potential (mV)	Type and # Surface Functional Groups/ NP
Feraheme (ferumoxytol)	AMAG Pharma	17-31	6.4 0.4*	5,874	32.4	62.7	-37.8 ± 3.7	>8 COOH
Amino-FH	Synthesized	15	6.4 0.4*	5,874	26.2	44.9	-29.6 ± 0.85	>8 NH_2
FH-Cy5.5	Synthesized	16.6	6.4 0.4*	5,874	23.2	47.8	-16.8 ± 1.3	2.5 Cy5.5
FH-Rho	Synthesized	16.9	6.4 0.4*	5,874	24.7	55.1	-14.5 ± 1.08	4 Rho
ProRho-FH	Synthesized	34.3	6.4 0.4*	5,874	20.6	65.2	-0.037 ± 0.84	5 ProRho
DTPA-CyAl5.5-FH	Synthesized	14.8	6.4 0.4*	5,874	21.4	35	-21.9 ± 1.65	3.5 DTPA-CyAl5.5

Table 4. Physicochemical properties of Feraheme and Feraheme-based materials.

Table 4 shows the various versions of Feraheme that have been synthesized thus far along with their physicochemical properties. FH-Rho was created by reacting NHS rhodamine with amino-FH and purifying using an Amicon spin filter unit. DTPA Lys(CyAl5.5)-Cys(NHS) is a multifunctional single attachment point (MSAP) reagent[134] obtained using diversity oriented synthesis (DOS) that contains a chelator and a fluorochrome.[143] In each case, the number of ligands attached per nanoparticle was determined using UV-vis abosrbance, and the average number of ligands for each formulation is shown in Table 4. It was verified that these ligands do not react with regular Feraheme, which only contains free hydroxyl and carboxyl groups on its surface.

There are some limitations of these conjugation strategies to NP coatings. First, in some instances it is desirable to attach targeting biomolecules that are hydrophobic (some drugs and peptides have a high density of hydrophobic amino acids) to the hydrophilic polymeric coatings of the NPs. If the density of hydrophobic targeting biomolecules is kept low, the hydrophilic

polymeric coating can endow the targeting NP with reasonable aqueous solubility. However, the conjugation of these molecules necessitates finding a solvent where both the NP (and its hydrophilic polymeric coating) and the targeting biomolecule are soluble. Although some of the reaction conditions were determined to maximize the number of ligands of the nanoparticle, others were specifically limited to prevent too many ligands from being attached. This is because we observed a decrease in long-term stability when more than ~6 ligands were attached to the FH surface.

6.5 Conclusion

There are a multitude of possible ligands that one could attach to amino-FH, from radioactive isotopes to targeting ligands to fluorophores. The chemical conjugation possibilities in combination with the superparamagnetic properties, as well as the fact that Feraheme already has FDA approval, make amino-FH an extremely useful platform nanoparticle for medical imaging applications. We discuss one possible functionalization of amino-FH and its application to cell labeling in Chapter 7.

CHAPTER 7: PROTAMINE-FUNCTIONALIZED FERAHEME AS A MAGNETOFLUORESCENT CELL LABELING AGENT

7.1 Summary

We synthesized a fluorescent cell-labeling nanoparticle by combining two commercially available, FDA-approved compounds: protamine, an arginine-rich protein with membrane translocating properties, and Feraheme (FH), a carboxymethyl dextran-coated iron oxide nanoparticle that is superparamagnetic. We have converted the free carboxyl groups on Feraheme into amino groups to make a material that we call amino-FH, a nanoparticle that is amenable to a variety of bioconjugation strategies (Chapter 6). We then synthesized a

fluorescent version of protamine by conjugating it with rhodamine, and conjugated the protamine-rhodamine compound (ProRho) to amino-FH. The resulting Feraheme-protamine-rhodamine material (ProRho-FH) is highly stable, fluorescent, superparamagnetic, and readily enters cells in short time frames. Both U87 glioma cells and MMSCs (mouse mesenchymal stem cells) internalized a high enough amount of nanoparticles to contain sufficient iron for MR detection. This work is particularly timely considering the discontinuation of Feridex, an iron oxide nanoparticle that has been used extensively for its superparamagnetic properties and for a variety of cell labeling applications. Unlike the literature on Feridex and protamine, which relies on non-covalent ionic interactions between protamine and Feridex, we show here a covalent conjugation of protamine that is reproducible and characterizable. The biocompatibility of the materials used to make ProRho-FH suggest that it could serve as a nanoparticle for labeling and tracking of cells in the clinic.

7.2 Background on Glioblastoma Multiforme

There are many potential applications for nanoparticles that can label cells for MR imaging, but one of the most promising areas is in new therapies for cancers of the central nervous system. These types of tumors are difficult to treat but new cell-based treatment strategies have shown encouraging results. For this reason we have chosen to work in the model of gliomas, which are cancers of the glial cells, most often found in the brain.

Malignant gliomas are one of the most lethal cancer types, and the median survival rate for glioblastoma multiforme (the most common type) is less than 1 year. Most glial tumors are highly invasive, making complete resection of the tumor extremely difficult,[144] and the inherent

dangers of cranial surgery make removal of the recurrent tumors problematic. In the vast majority of glioma cases (more than 95%), the tumors return after surgical resection, both in proximity to the resection cavity and at satellite sites. Often the treatment plan is an approach combining chemotherapy, radiation therapy, and surgical resection. One of the main issues in systemically treating gliomas is solving the problem of crossing the blood brain barrier. Stem cells have the ability to cross this barrier and home to tumors and other pathologies[145-147] and even to metastases distinct from the primary tumor, making them useful as imaging agents or as delivery vehicles for therapeutic agents.

7.3 Background on Cell Labeling Agents

The ability to non-invasively label and track cells in vivo is becoming increasingly useful for a variety of applications. As imaging technologies improve, it is possible to follow cell migration patterns in vivo to better understand the biological mechanisms of disease. Cell tracking is also essential for the development of cell-based therapies, a promising treatment strategy that is rapidly becoming a viable reality. The use of magnetic resonance (MR) is a particularly attractive imaging method due to its non-invasiveness and its excellent soft tissue and spatial resolution. There are a variety of contrast agents available for MR but superparamagnetic iron oxide nanoparticles have long been an obvious choice for a variety of reasons including the fact that they are extremely safe and non-toxic, are relatively inexpensive, significantly affect the T2(*) relaxation time, and have coatings that can provide many possible strategies for bioconjugation. For a more complete discussion, see section 2.3.

The goals of the current work were to develop a NP for cell labeling and tracking that would be amenable to clinical translation by virtue of the materials and chemistries used. The

discontinuation of the iron oxide nanoparticle Feridex, perhaps the most widely used nanoparticle in the cell labeling literature, makes the development of the iron oxide nanoparticle Feraheme as an effective cell labeling material particularly timely.

7.3.1 Cell Imaging and Cell-based Therapies

The use of cells for therapeutic applications has wide-ranging possibilities in a variety of diseases including cancer, cardiovascular disease, diabetes, HIV, and a variety of hereditary diseases. Below is a table showing different cell types and examples from the literature that have covered different methods used to track cells used in therapy.

Cell based therapies and Cell tracking by MRI

Cells	Cell based therapy	Recent Reviews Of Therapeutic Utility	MRI Based Cell Tracking
Dendritic cells	Cancer immunotherapy	148	149 150
T cells	Cancer immunotherapy	151 152	117, 153, 154
Stem Cells	Restore damaged myocardium	155	41, 156-158
Neuroprogenitor cells	Restore damaged CNS	159	
Islet cells	Type I diabetes	151, 160	161
Chondrocytes	Joint repair &regeneration	162	

Table 5. Brief review of imaging of cell-based therapies in the literature.

7.3.2 Transfection agents

Some cell tracking techniques use labels that attach to the cell surface and remain external to the cell; however this strategy risks the label interfering with cell surface interactions or detaching from the cell membrane.[163] We have thus chosen to engineer nanoparticles that will enter the cell. There are several routes to achieving cell internalization, the simplest being incubating cells with the nanoparticles, capitalizing on the natural mechanisms of pinocytosis and phagocytosis.[164] However, this strategy is not easily generalizable to different cell types as only certain cells are intrinsically phagocytic. It is possible to increase internalization rates by disruption of the cell membrane, which can be achieved by the addition of transfection agents in solution,[165, 166] or by techniques such as electroporation. Another strategy is to attach a molecule that facilitates internalization to the nanoparticle coating itself, such as a cell penetrating peptide like the HIV tat (trans-activator of transcription) peptide[167] to promote membrane translocation, a dendrimer to induce membrane bending and then endocytosis,[41] or an anti-transferrin receptor monoclonal antibody to promote receptor-mediated endocytosis.[168] Although these are all viable solutions, it is worth noting that the use of a monoclonal antibody for internalization could be problematic for clinical applications due to current FDA regulations.

A delicate balance of charges is necessary to maintain a dispersion of the nanoparticles in aqueous solution, and the disruption of this balance by the conjugation of transfection agents to the nanoparticle coating can sometimes lead to nanoparticle precipitation. Poly-L-lysine has been successfully complexed with Feridex nanoparticles but it can cause uncontrollable nanoparticle aggregation; furthermore, nanoparticle-poly-L-lysine complexes can bind nonspecifically to the cell surface and cause cellular aggregation.[169] Another study comparing the transfection agents protamine, poly-lysine, and lipofectamine also found that Feridex

agglomeration is a large problem.[166] The polydispersity (10-1000 nm) of Feridex further complicates its use as a labeling agent because larger diameter nanoparticles tend to remain at the cell surface and not internalize; this kind of interaction could lead to an undesirable immune response or in other ways interfere with cell surface interactions.[170] Furthermore, there has been some evidence that there are unwanted biological side effects of the poly-L-lysine-Feridex combination.[171]

Protamine sulfate, the transfection agent used in the work described here, is a low molecular weight, naturally occurring transfection agent that has already been FDA approved as a heparin antagonist and is also used as an excipient in insulin injections. It is an arginine-rich nuclear protein whose natural function is to stabilize and bind DNA into a compact form in sperm nuclei. When combined with ferumoxides it has been shown to have no effect on cell proliferation, viability, or differentiation.[172] Protamine has a higher therapeutic window and is a far more effective transfection agent than poly-L-lysine,[173] and it has a similar or even superior membrane-translocating ability to the HIV tat peptide.[126] Another advantage of protamine is that it has a single reactive amine at the N-terminus and a single carboxyl group at the C-terminus, facilitating bioconjugation strategies. It is commercially available as a clinical injectable agent, benefiting from the large-scale pharmaceutical production and quality control, and is inexpensive. For these reasons, protamine was chosen as the transfection agent to attach to Feraheme as a cell internalization agent.

Although the exact mechanism of cell internalization is not completely understood, it is thought that arginine-rich peptides such as protamine and HIV tat are membrane-permeable[174] and able to shuttle cargo into cells. Some studies have shown that this process is not the result of an endocytotic mechanism,[175] although there are conflicting opinions. Protamine is known to

interact with the highly negatively-charged glycosaminogycan heparin, and is used in the clinic for this very purpose. It also interacts with extracellular and cell-surface glycosaminoglycans,[176] and probably the lipid bilayer itself.[177] However, it is not clear what the affect of conjugation to a large nanoparticle will have, and it is possible that internalization is the result of a combination of factors.

7.4 Aims

In this chapter we describe how to make a cell labeling and tracking agent that is the chemical combination of two commercially available, FDA-approved drugs. There is a lack of consistency in the cell labeling literature when it comes to the protocols used for cell labeling, making it difficult to compare across studies. Ideally, a cell labeling method should be biocompatible, biodegradable, and have little to no effect on cellular function. In this study we create and fully characterize a long-circulating, non-toxic nanoparticle that can be used as a contrast agent to image cells non-invasively using magnetic resonance (MR) imaging.

Based on these criteria a simple, reproducible chemical approach was developed to yield stable iron oxide nanoparticles attached to protamine via an amide linkage. Protamine (about 4 kDa) is more than 75% arginine and endows NPs with membrane translocating activity. Feraheme (FH, a full list of abbreviations used in this work is shown in

Table 6) is an carboxylated polymer-coated iron oxide nanoparticle that is commercially available as an injectable solution. This work describes how to chemically combine two FDA-approved compounds, protamine and Feraheme, to yield a magnetofluorescent cell labeling nanoparticle that can be stored at 4°C indefinitely and used to label a variety of types of cells.

7.5 Experimental

Feraheme (AMAG Pharmaceuticals, Lexington, MA) and protamine sulfate (American Pharmaceutical Partners, Schaumburg, IL) were from the MGH pharmacy. The NHS ester of tetramethyl rhodamine was from Molecular Probes (Eugene, OR). Other chemicals were from Sigma-Aldrich (St Louis, MO). Separations used PD-10 columns (GE Healthcare, Piscataway, NJ) or 100 kDa Amicon spin concentrator (Catalog # UFC910024 Millipore, Billerica, MA). Light scattering and zeta potentials were measured with a Nano-ZS zetasizer (Malvern, Medford, MA). Relaxivity was determined on a 20 MHz MiniSpec at 40°C (Brucker Systems Billerica, MA). Flow cytometry was on a BD FACSCaliber (BD Biosciences, Mansfield, MA). Mass Spectrometry was performed at the Tufts University Core Facility (Boston, MA). Microscopy was performed on an Olympus IX51 inverted research microscope (Center Valley, PA). Cell lines were obtained as a generous gift from Dr. Khalid Shah (Molecular Neurotherapy and Imaging Laboratory, Harvard Medical School). Cells were counted using a Reichert brightline hemocytometer (Hausser Scientific, Hersham, PA). Fluorescent images of the agar phantoms was obtained using a KODAK In-Vivo Multispectral System FX (Carestream Health, Rochester, NY). MR imaging was performed on a 40-cm bore Bruker Advance 4.7T scanner for the agar phantom imaging and a 4.7T Bruker Pharmascan MRI scanner (Bruker Biosciences, Billerica, MA) for the in vivo imaging.

Concentration Determination

Iron, rhodamine and ProRho concentrations were determined spectrophotometrically[5] using 94,000 L/ml-cm as the extinction coefficient for rhodamine at 555 nm.[135]

Cell culture

U87 cells were grown in DMEM fortified with 10% fetal bovine serum and 1% pen-strep. MMSCs were cultured in DMEM mixed with 10% fetal bovine serum, 1% l-glutamine, 10% Horse Serum, 1% antibiotic-antimycotic. Cells were split from 75 cm^2 flasks into 24 well plates and grown to 90% confluency.

Synthesis of amino-FH

Feraheme nanoparticles were incubated with 3.72 mol ethylene diamine per mol iron, 0.49 mol 1-Ethyl-3-[3-dimethylaminopropyl] carbodiimide hydrochloride (EDC) per mol iron, and 0.21 mol hydroxybenzotriazole (HOBT) per mol iron in 0.1M MES buffer pH 6.0 for 1.5 hours at 50°C. In a typical reaction, 6 mg Fe of FH was reacted with 1 mg EDC and 0.2 mg HOBT, then reacted with 40 ul of 1M ethylene diamine dihidrychloride solution, and purified using a PBS PD-10 column. Amino-FH was stable at 4°C for months.

Synthesis of FH-Rho

Amino-FH was reacted with an excess of Rhodamine NHS ester overnight at 4°C, a typical reaction using 6 mg Fe of amino FH and 1 mg of Rhodamine NHS ester (0.018 mol rhodamine/mol iron). Unreacted rhodamine was removed by filtration with a 100,000 NMWL cutoff Amicon spin column, eluting with PBS several times until the eluent runs clear.

Synthesis of ProRho

This synthesis was described in detail in.[126] Briefly, rhodamine NHS ester (0.5 mg) was dissolved in 100 μL DMSO and added to 5 mg (0.5 mL) protamine and 100 μL PBS. The solution was allowed to react overnight at room temperature, then the protamine was precipitated with ethanol. The precipitate was resuspended in water and purified by HPLC reverse phase C18 (flow conditions) to produce protamine-rhodamine (ProRho), which was characterized by MALDI-MS. ProRho was lyophilized and could be stored at -20°C indefinitely.

Synthesis and Characterization of ProRho-FH

Amino-FH (6 mg) was reacted with EDC (1 mg, 0.48 mol per mol Fe), NHS (0.2 mg, 0.21 mol per mol Fe), and an excess of ProRho (1 mg) at 70°C for 30 minutes, and unreacted ProRho and other reagents were removed with a 100 kDa NMWL Amicon spin column using repeated additions of PBS. Longer reaction times can lead to more ProRho per nanoparticle, and more than 4-6 ProRho/NP can lead to precipitation. The resulting ProRho-FH formulations were characterized by light scattering, absorbance, zeta potential, and dilutions of the nanoparticle were measured for T1 and T2 to determine relaxivities.

Covalent Binding of ProRho to Amino-FH Using Heparin Ion Exchange Affinity Column

A heparin affinity column was purchased (HiTrap Heparin HP, GE Healthcare, Piscataway, NJ) and different formulations of ProRho-FH were exchanged into binding buffer (10 mM phosphate buffer pH 7) and flowed through the column using binding buffer as well as elution buffer ((10 mM phosphate buffer pH 7 + 1 or 2 M NaCl). Fractions were collected and analyzed spectrophotometrically for iron (absorbance at 300 nm) and rhodamine (absorbance at 555 nm).

Cell labeling

U87 and mouse mesenchymal stem cells (MMSCs) were grown to approximately 90% confluency in 24-well plates. Cells were incubated with ProRho-FH at varying concentrations in modified DPBS for two hours to measure concentration dependence, or for a varying time period to examine uptake kinetics. Cells were washed three times with DPBS, then either detached in sheath fluid for FACS analysis or lysed with 1% triton X-100 in PBS for relaxivity analysis. Standards for the relaxivity experiments were made by spiking lysates of untreated cells with ProRho-FH. One well was trypsinized and the cells counted with a hemocytometer to normalize uptake data to a per cell basis. Microscopy was performed by treating the cells as described above, washing with heparinized PBS (15 mg/ml), and then adding Hoechst stain to visualize cell nuclei. All experiments controlled for basal uptake by each cell line by concurrently doing each experiment with FH-Rho, the fluorescent version of the Feraheme nanoparticle that does not have a membrane translocating moiety. The optimal labeling conditions were determined to be 25 ug/ml Fe for 2 hours at 37°C.

Iron Stain

Cells were fixed in 4% paraformaldehyde in PBS and then incubated with 2% potassium ferrocyanide and 3.7% hydrochloride acid (Prussian Blue staining, a.k.a. Perl's Reagent) for 30 minutes. For diaminobenizidine-enhanced staining (DAB-enhanced), after Prussian Blue staining cells were incubated with DAB solution (Sigma, St. Louis, MO) for 10 minutes and washed with PBS.

Toxicity

ProRho-FH was assayed for toxicity with three different methods. Cells were incubated with varying concentrations of ProRho-FH and then assessed by trypan blue exclusion. Cells were also assessed by flow cytometry and Sytox dead cell staining. A positive control was obtained by disrupting cell membranes using repeated cycles of freezing and thawing. Finally, Cytotox-One, a homogenous membrane integrity assay measuring the release of lactate dehydrogenase (LDH) fluorometrically, was performed 24 hours after cell loading. A lysed cell control was used to calculate percent cytotoxicity.

MR Phantom Imaging

ProRho-FH was loaded into U87s and MMSCs by incubating them for 2 hours at 37°C in a solution of 25 ug/ml Fe of ProRho-FH in modified DPBS. Loaded cells and unloaded controls were embedded in 1% agar at a range of densities from 150,000 cells/ml to 15,000,000 cells/ml in a 384-well format. The phantom sample was placed in a 40-cm bore Bruker Avance 4.7 T MRI scanner equipped with a 10 cm inner diameter birdcage resonator radiofrequency coil and 26 G cm^{-1} triple axis gradients, and imaged using a T_2-weighted pulse sequence with echo time (TE) of 180 ms and repetition time (TR) of 4000 ms at ambient temperature. Phantom samples were also imaged by fluorescence using a Kodak In-Vivo Multispectral Imaging System.

In vivo MR Imaging

ProRho-FH was loaded into MMSCs by by incubating them for 2 hours at 37°C in a solution of 25 ug/ml Fe of ProRho-FH in modified DPBS. Cells were implanted stereotactically into brains of female nude mice at a range of cell concentrations. MR imaging was performed

with a mouse brain coil under respiration-monitored isofluorane gase anaesthesia on a 4.7T Bruker Pharmascan MRI scanner (Bruker Biosciences, Billerica, MA). T2-weighted images TR = 3500, TE = 75.1, matrix size 192 x 192, field of view 2.5 x 2.5 cm^2, slice thickness 0.7 mm and 16 sections were acquired.

7.6 Results and Discussion

A list of abbreviations used in this chapter is shown here:

Material	Abbreviation
Feraheme	FH
Feraheme with its carboxyl groups converted to amine groups	Amino-FH
Protamine	Pro
Rhodamine	Rho
Protamine covalently conjugated to Rhodamine (at the N terminus)	ProRho
Feraheme covalently conjugated to Rhodamine	FH-Rho
Feraheme covalently conjugated to protamine that has been conjugated to rhodamine (ProRho)	ProRho-FH
Feraheme non-covalently (electrostatically) associated with protamine conjugated to rhodamine (ProRho)	ProRho+FH

Table 6. List of abbreviations used.

As described in Chapter 6, Feraheme is an FDA-approved material that can be injected in large amounts for iron anemia treatment. We consider FH used for cell imaging and tracking to be a very safe material, since the doses used for iron anemia treatment far exceed the doses that would be used to track cells in cell-based therapies. Protamine, the other major component of

the cell labeling agent described here, is also an FDA-approved material that is most often used as a heparin antagonist. It consists of mostly arginine (60-70%) and has a molecular weight of about 4,200 daltons. Its characteristics as a transfection agent are described in more detail in Section 7.3.2.

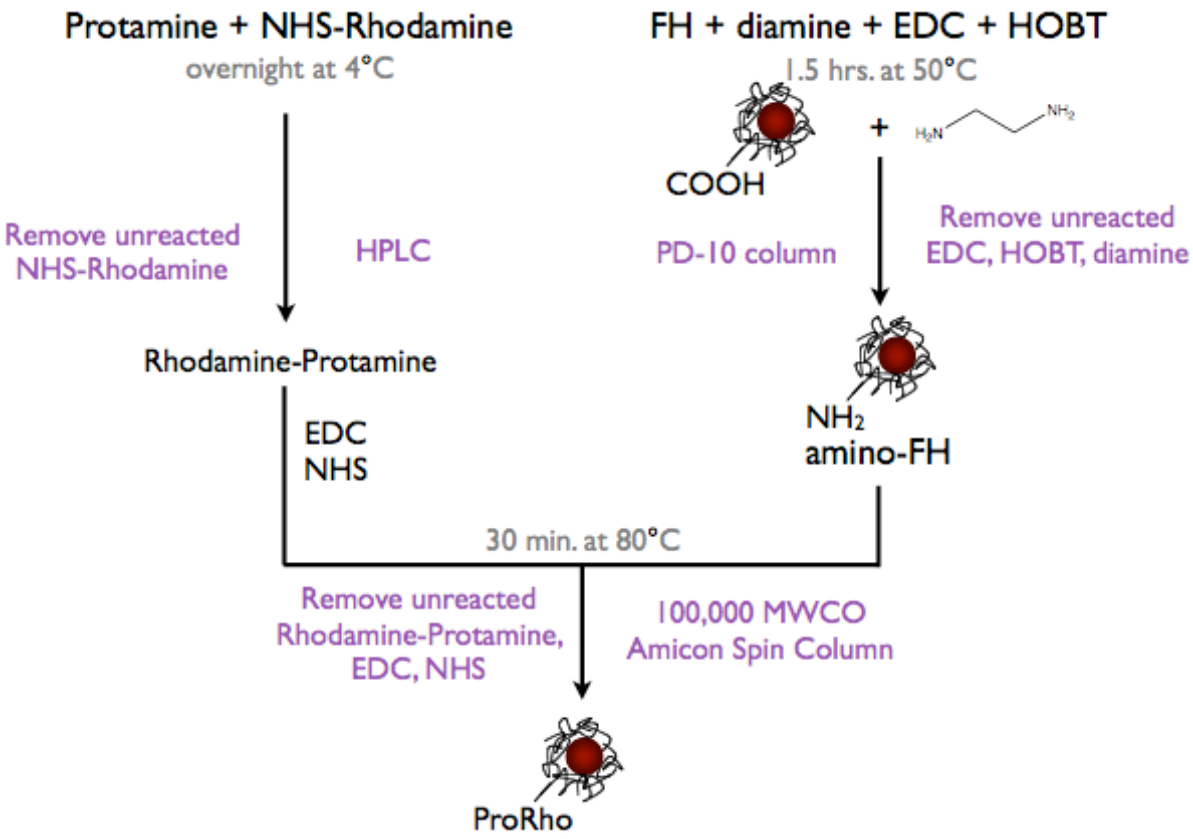

Figure 24. Schematic of synthesis of ProRho-FH. Protamine and Feraheme (FH) are both commercially-available, FDA-approved drugs.

To create the protamine-rhodamine conjugate ProRho, protamine was reacted with NHS-rhodamine as described previously.[126] The product was purified using HPLC and the creation of the ProRho was verified using mass spectrometry. The carboxy groups on the FH NP were converted to amines using EDC chemistry and ethylene diamine to make amino-FH as described

in Chapter 6. Two types of nanoparticles were then made for the in vitro and in vivo experiments: a control nanoparticle consisting of only rhodamine attached to the polymer coating (FH-Rho), and a cell-internalizing nanoparticle consisting of protamine and rhodamine attached to the polymer coating (ProRho-FH). The control nanoparticle was used in various experiments to ensure that the cell internalizing behavior of ProRho-FH was not inherent to the Feraheme nanoparticle itself but a behavior conferred to it by the cell translocating agent protamine. A schematic of these two nanoparticles is shown in Figure 25.

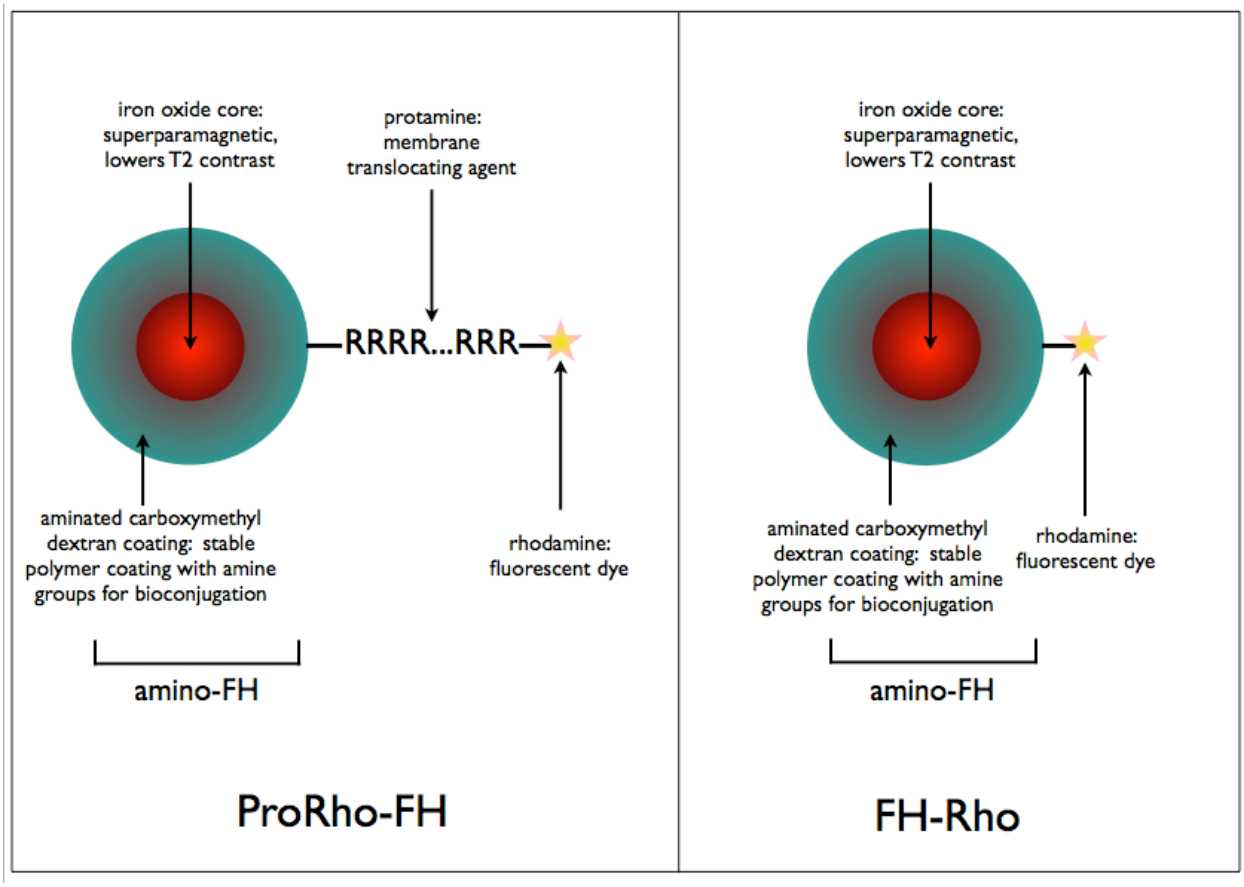

Figure 25. Schematic of the two nanoparticles used in the uptake studies. Left: ProRho-FH is the cell labeling nanoparticle. Right: FH-Rho is the fluorescent Feraheme used as a control.

To achieve an amide bond between the amine on the amino-FH and the carboxy terminus of the protamine on the ProRho, CDI chemistry was used to form an amide linkage (Figure 23).

Table of Physicochemical Properties					
Material	Size (dynamic light scattering) [nm]	Ligands/NP	R1 [$mmol^{-1}/sec^{-1}$]	R2 [$mmol^{-1}/sec^{-1}$]	Zeta Potential [mV]
Feraheme	18.2 ± 1.21	>8 COOH*	32.4 $R^2 = 0.9999$	62.7 $R^2 = 0.9976$	-37.8 ± 3.7
Amino-FH	12.2 ± 0.7	>8 NH_2*	26.2 $R^2 = 0.9994$	44.9 $R^2 = 0.972$	-29.6 ± 0.85
FH-Rho	15.23 ± 1.46	3.96 ± 0.27 Rho	24.7 $R^2 = 0.9974$	55.1 $R^2 = 0.9817$	-14.5 ± 1.08
ProRho-FH	45.7 ± 1.99	4.99 ± 0.87 ProRho	20.6 $R^2 = 0.9978$	65.2 $R^2 = 0.9962$	-0.037 ± 0.84
ProRho-FH + trypsin	18.2 ± 1.8	n/a	nd	nd	nd

Table 7. Table of physicochemical properties of nanoparticles used in this Chapter.

ProRho-FH was characterized by light scattering for size, by UV-Vis to determine the number of ProRho molecules per nanoparticle, and by relaxometry to determine the magnetic properties of the nanoparticle (Table 7). The number of ProRho molecules per nanoparticle affected the long-term stability of ProRho-FH, so the synthesis was optimized to yield approximately 4-6 ProRho molecules/nanoparticle, which was enough to provide significant membrane translocating effects and fluorescence but not so many that the ProRho molecules affected the solubility and thus the stability of the ProRho-FH. The attachment of ProRho to the nanoparticle was also verified using trypsin and light scattering measurements. Trypsin is a serine protease that hydrolyzes the protamine so that the size of the ProRho-FH shrinks back to nearly the size of the original nanoparticle FH (Figure 26).

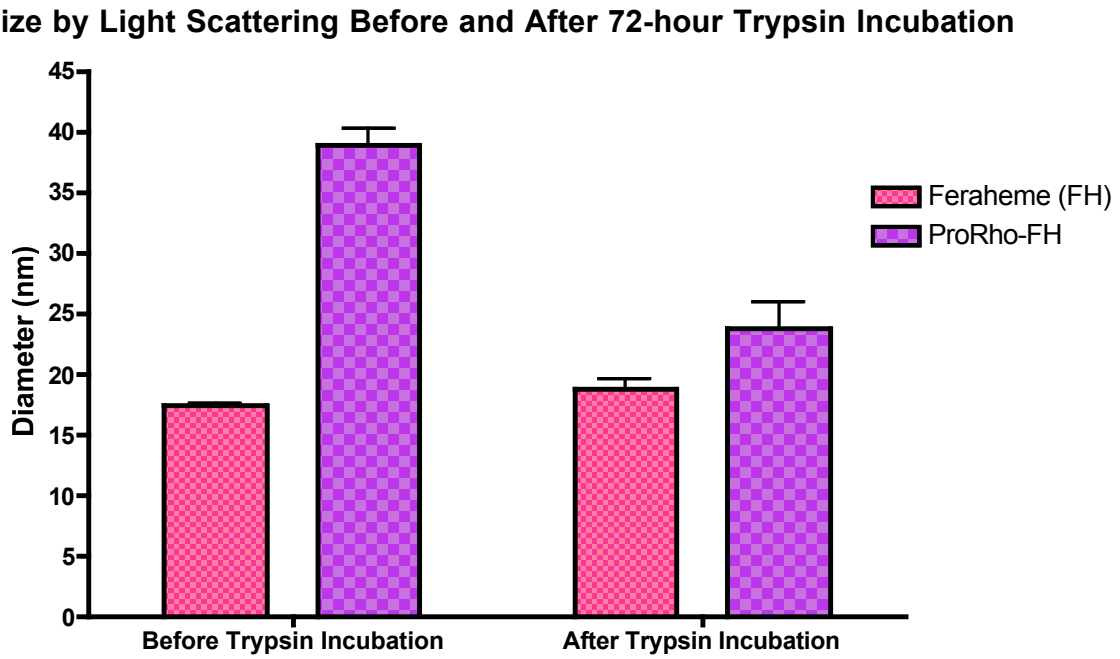

Figure 26. Difference in hydrodynamic size due to conjugation of ProRho to Feraheme, and the reduction in size due to digestion of protamine by trypsin. Measurement was performed using dynamic light scattering.

ProRho is a highly positively charged molecule due to the guanidino functional groups in the protamine, which is essentially a poly-arginine molecule. The carboxymethyl dextran coating on the FH is slightly negatively charged and has a zeta potential in 5mM Tris pH 7 of -38 mV (Table 7). Protamine and dextran have an attractive ionic interaction that has been exploited for a variety of applications.[178] Indeed, many researchers have used a non-covalent protamine complex with polymer-coated iron oxide nanoparticles as a cell labeling material. To address whether it would be sufficient to simply non-covalently associate protamine to the Feraheme nanoparticle using ionic interactions, a series of experiments were performed with a heparin ion exchange affinity column. Protamine complexes strongly with heparin, thus this column was a useful tool for assessing the tightness of binding between the FH and the ProRho. The

experiment was performed using three different formulations each of covalently bound ProRho-FH and non-covalently associated ProRho+FH, and typical results are shown in Table 1.

Initial tests of the heparin column were performed with amino-FH only and ProRho only. The amino-FH was immediately eluted with the binding buffer in the low-salt fraction because it has no attractive interaction with heparin. In contrast, the ProRho bound tightly with the binding buffer and did not come off with the addition of 1M NaCl to the buffer; it was only eluted with the addition of 2M NaCl. Formulations of covalently bound ProRho-FH and non-covalently associated ProRho+FH were prepared and run through the heparin column. The A300 bars correlate with the presence of iron (i.e., FH), and the A555 bars correlate with the presence of Rhodamine (i.e., ProRho). It is obvious in the case of the covalent version of ProRho-FH that since FH is retained almost entirely until elution with 2M NaCl, eventually coming out around the same time as the ProRho, that the FH is tightly bound to the ProRho. In other words, FH and ProRho co-elute in the case of the covalent ProRho-Fh. For the noncovalent case, most of the iron is eluted with the binding buffer and only a small amount is retained and eluted with 2M NaCl, showing that there is some minimal association of iron to the ProRho but not to a great extent. Additionally in the noncovalent case, although most of the ProRho elutes at the salt concentration required to elute ProRho alone (2M NaCl), a significant amount of ProRho elutes earlier than usual (binding buffer, 1M NaCl), suggesting that a portion of the ProRho is associating with the FH and is dragged out by the nanoparticle. In other words, it is possible that some of the ProRho is not retained in the column due to complexation and aggregation effects with the FH.

These results seem to show that ProRho covalently bound to FH has a much tighter binding interaction than the non-covalent association between ProRho and FH. Nevertheless, it

is true that even in the covalent case it is likely that both covalent and non-covalent associations are present at the same time.

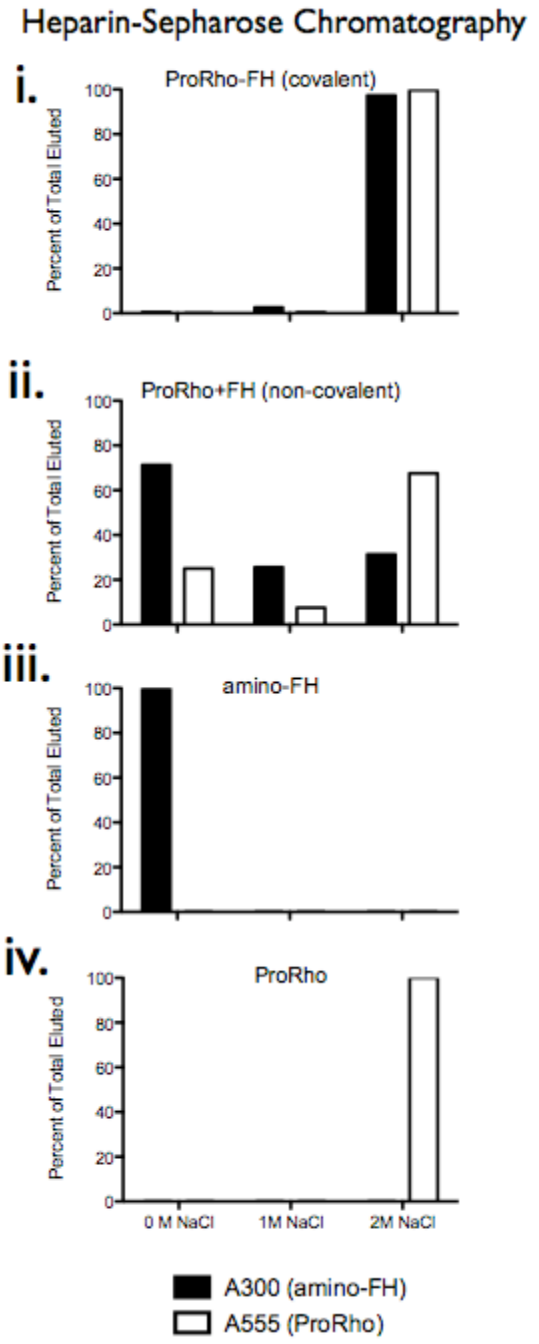

Table 8. The covalent interaction between ProRho and amino-FH was demonstrated using heparin-sepharose chromatography. Percentage of total eluted shown in black (iron absorption) and white (Rhodamine absorption). ProRho-FH (covalent) maintained its association (integrity) with heparin-sepharose chromatography, with ProRho and amino-FH co-eluting primarily in the high salt (2M NaCl) fraction (i). On the other hand, ProRho + FH (non-covalent) dissociated on the column, with much of the iron eluting at low salt (PBS) conditions (ii). The elution of ProRho (iv) and amino-FH (iii) by themselves were also obtained as controls. Binding Buffer consists of 10 mM phosphate buffer at pH 7.

Another confirmation of the necessity of covalent interaction was determined by measuring cellular uptake by relaxometry. Tracking fluorescence by flow cytometry or microscopy would not be of use here because these methods follow the fluorescent ProRho and not the iron. Uptake of covalent and non-covalent ProRho-FH nanoparticles were compared in a series of in vitro relaxometry experiments. It is clear from Figure 27 that there is significant concentration-dependent uptake for the covalently bound ProRho-FH and little to no uptake of iron into the cells when incubated with non-covalent ProRho+FH.

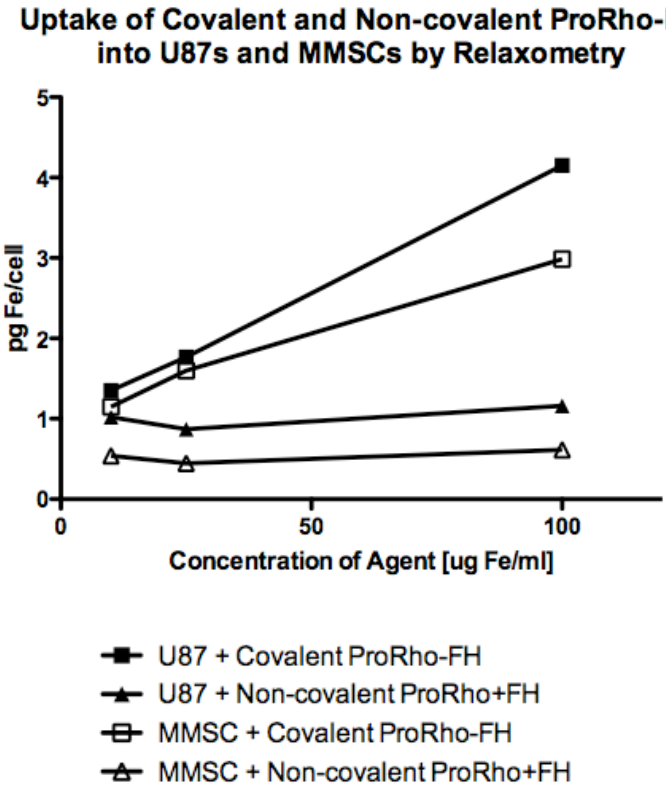

Figure 27. Covalent binding between ProRho and Feraheme is necessary for uptake into cells, as shown by relaxometry data of iron uptake covalent and non-covalent ProRho-FH. Cells were incubated with covalently bound ProRho-FH and non-covalently associated ProRho-FH for 2 hours at 37°C, then washed and lysed and measured by relaxometry. Relaxation times were compared to standards.

Purification of the nanoparticles had to be meticulous and thorough due to the charged nature of the ProRho. Both ProRho and rhodamine alone were filtered through an Amicon centrifugal filter unit in order to prove that both molecules flow freely through the filter; this was achieved by verifying using UV-Vis that the retentate and eluent had the same concentration of material after filtration. The rhodamine was able to flow freely through the 50,000 NMWL filter unit, while protamine-rhodamine required the larger-pored 100,000 NMWL filter unit due to noncovalent associations between ProRho molecules.

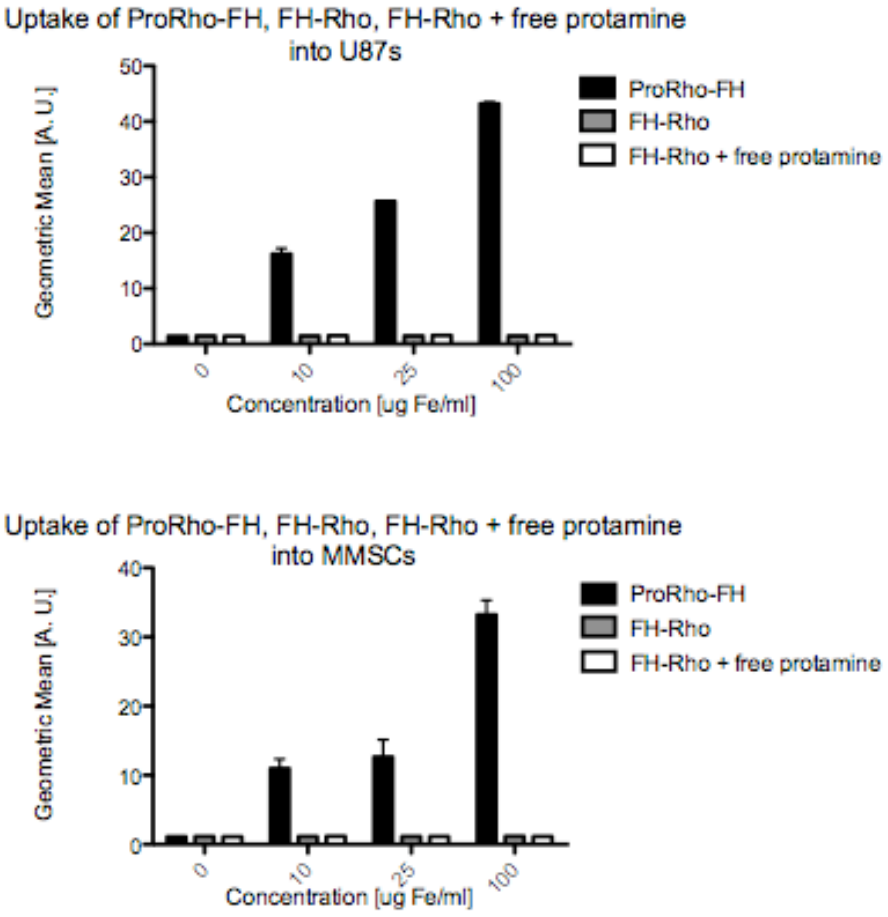

Figure 28. Concentration dependence of uptake of ProRho-FH into U87s (top) and MMSCs (bottom) as determined by flow cytometry. FH-Rho with and without the addition of free protamine were used as a control. Cells were incubated with ProRho-FH for 2 hours at 37°C at a range of concentrations. Experiment was performed in triplicate. Concentration dependence of ProRho-FH uptake appears to be exponential. Covalent attachment of protamine to the nanoparticle is necessary for uptake, since no significant uptake is observed with FH-Rho with and without incubation with free protamine.

Although the nanoparticle is superparamagnetic and can be visualized by MR, it is very useful to enable fluorescent tracking of the nanoparticle as well and this is achieved by conjugating rhodamine to the protamine. Fluorescent microscopy and flow cytometry are useful in vitro methods of characterization of uptake. A schematic of the cell labeling nanoparticle ProRho-FH as well as the control fluorescent nanoparticle without protamine is shown in Figure 25. Cell loading as a function of cell type and concentration as assessed by flow cytometry is displayed in Figure 28. Cell loading increases with increasing concentration of agent, and does not exhibit a dose-response curve that would be typical of a receptor-ligand interaction. Neither FH-Rho (the fluorescent FH nanoparticle without the protamine) nor FH-Rho plus free protamine were taken up by cells at all, suggesting that protamine bound to the FH nanoparticle is necessary for transfection into cells. Time dependence of uptake is shown in Figure 29.

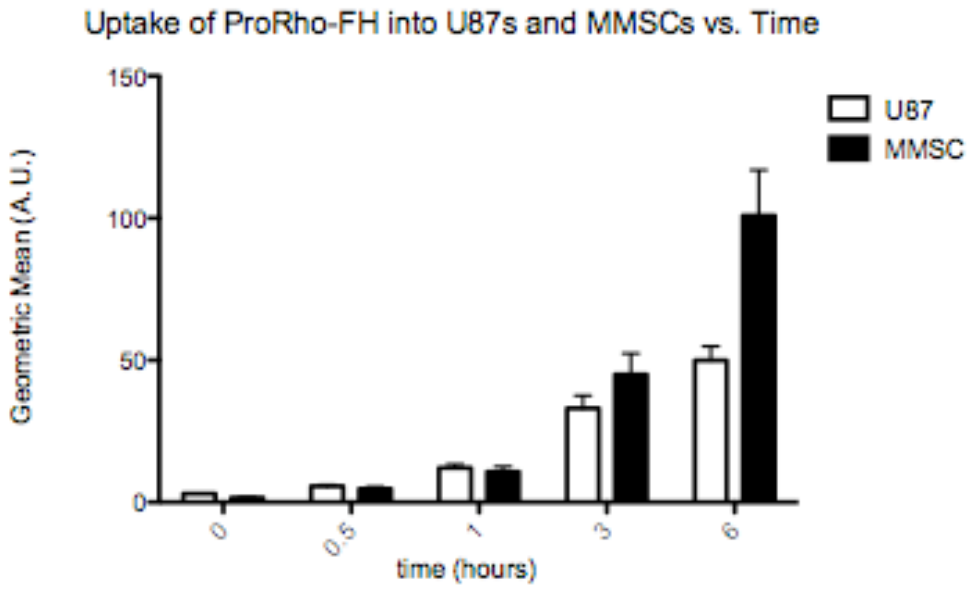

Figure 29. Time dependence of uptake of ProRho-FH into U87s and MMSCs by flow cytometry. Cells were incubated with 10 µg Fe/ml ProRho-FH in DPBS for a range of times, washed and then assessed for fluorescence by flow cytometry.

Although there is appears to be a continuous increase in uptake with time, a balance must be found between ease of experimentation, the amount of nanoparticle agent used, and the cells' tendency to deadhere over very long incubations in DPBS. A 2-hour incubation was chosen based on the effectiveness of labeling as well as literature values.

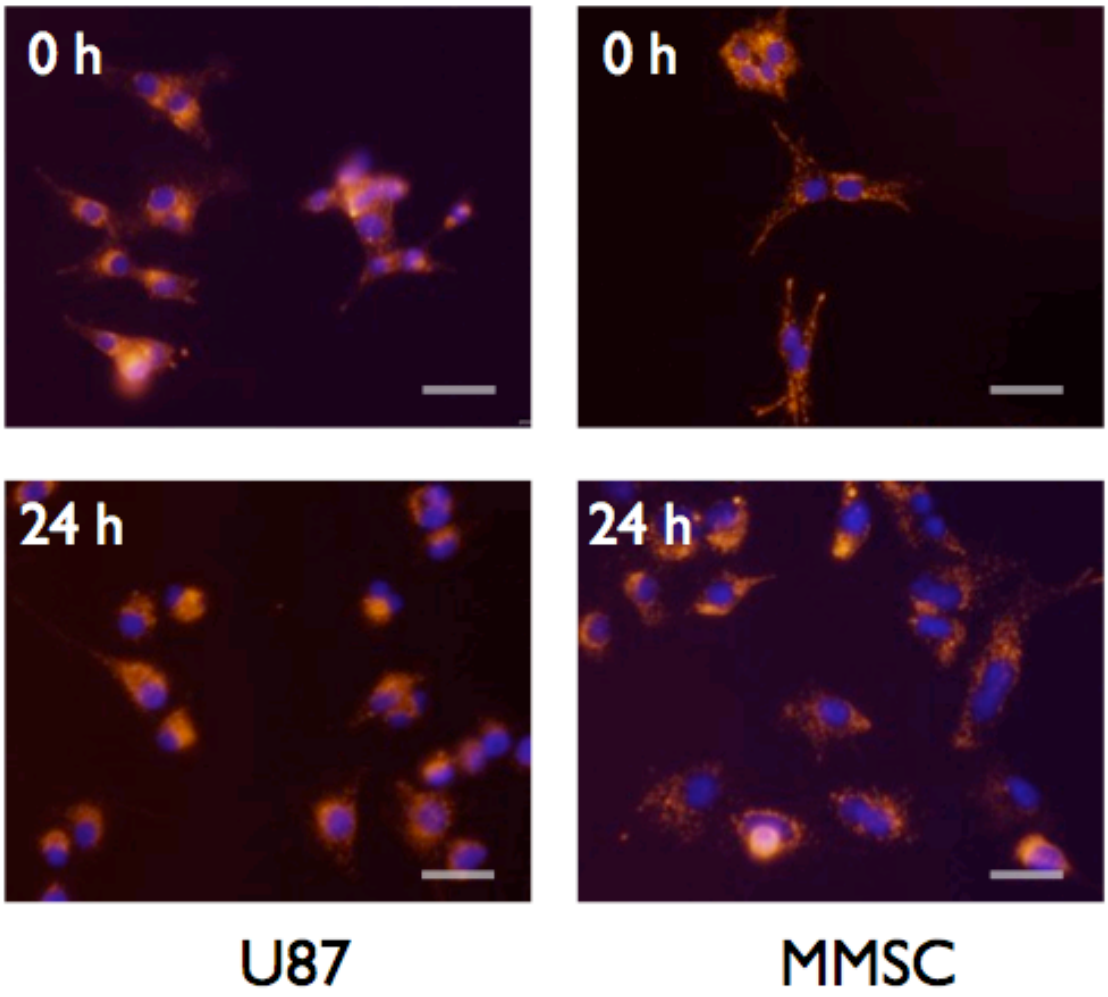

Figure 30. Fluorescence microscopy of U87 and MMSC after loading with ProRho-FH. The cells have been incubated with 25 ug/ml Fe of ProRho-FH for 2 hours at 37°C. Nuclei were visualized using Hoescht staining. Top: Cells were imaged using fluorescence microscopy immediately after the 2 hour incubation. Bottom: After the 2 hour incubation cells were washed 3 times, allowed to proliferate in media for 24 hours, then re-imaged. Scale bar = 50 μm.

Uptake of ProRho-FH into U87s and MMSCs was also visualized using light microscopy (Figure 30). The nanoparticles reside within vesicles of the intracellular compartment and are excluded from the nuclear compartment, and appear to remain in the endosomes even after 24 hours. The slight difference in intracellular distribution of ProRho-FH from ProRho alone[126] could be due to the fact that it is conjugated to the large, slightly negatively-charged FH nanoparticle. When acid is added to the cells, the pattern of fluorescence switches to the nucleoli and nuclei (results not shown), indicating that the amide bond between the ProRho and the FH has been hydrolyzed and the ProRho is acting alone.

Uptake of ProRho-FH into U87s and MMSCs by Relaxometry

Cell Type	Fe/cell [pg]	Fe Conc./cell [g/L]	Cellular Fe [mM]	Cellular T2 [msec]
U87	9.66 ± 0.45	4.02 ± 0.19	72.09 ± 3.4	0.0095 ± 0.011
MMSC	3.1 ± 0.93	1.29 ± 0.38	23.11 ± 6.91	0.00352 ± 0.0026

Table 9. Uptake of ProRho-FH into U87s and MMSCs by Relaxometry. Cells were incubated with 25 ug/ml ProRho-FH for 2 hours at 37°C. Cell volume was estimated to be 2.4 pl.

The superparamagnetic nature of FH allows uptake to be assessed by relaxometry as well (Figure 27, Table 9). The concentration dependence of uptake shows a similar curve when assessed by relaxometry as when assessed by flow cytometry. Incubation with 25 ug/ml Fe of ProRho-FH at 37°C yields cells with approximately 3-10 picograms of iron per cell, which is

sufficient for MR detection as it has been shown that only subpicomole quantities of iron are required for detection by micro-MRI.[179]

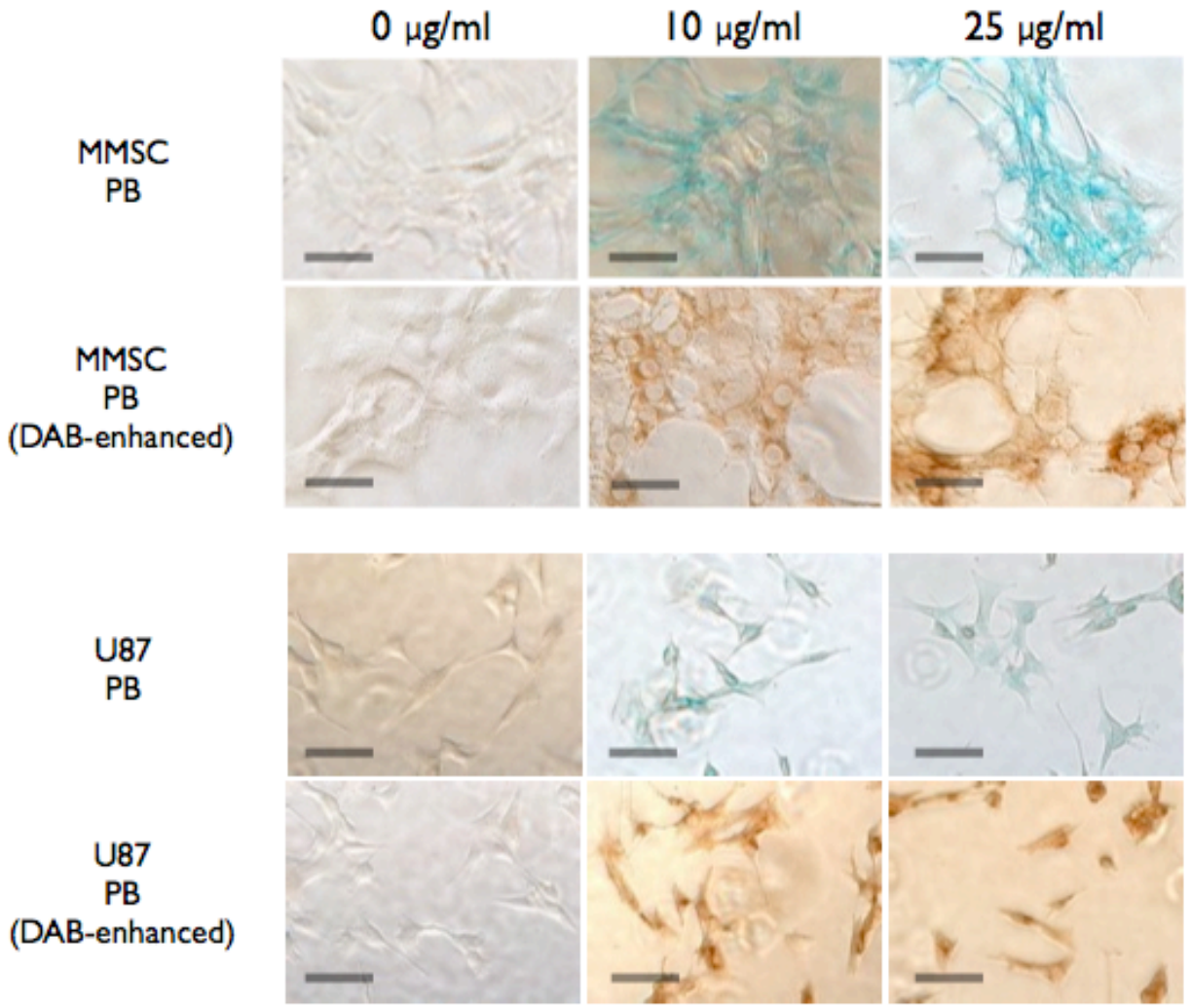

Figure 31. Staining for iron in U87s and MMSCs using Prussian Blue (DAB-enhanced and non-DAB enhanced). Cells were incubated for 2 hours at 37°C with 0 ug/ml, 10 ug/ml, and 25 ug/ml of ProRho-FH and then stained with Prussian Blue with (rows 2 and 4) and without DAB enhancement (rows 1 and 3). Scale bar = 50 µm.

Cells were also stained for iron using non-DAB enhanced and DAB-enhanced Prussian Blue staining. Formation of an insoluble precipitate in the presence of Perl's Reagent occurred to a much lesser extent for ProRho-FH than for FH, most likely because the protamine chelates the

iron (results not shown). Nevertheless, cells labeled with ProRho-FH were stained with Prussian Blue even though the assay may have been somewhat inhibited by the presence of the protamine. Cells that were not incubated with ProRho-FH showed no staining while cells that were incubated with ProRho-FH showed intense staining with nearly 100% of cells being labeled.

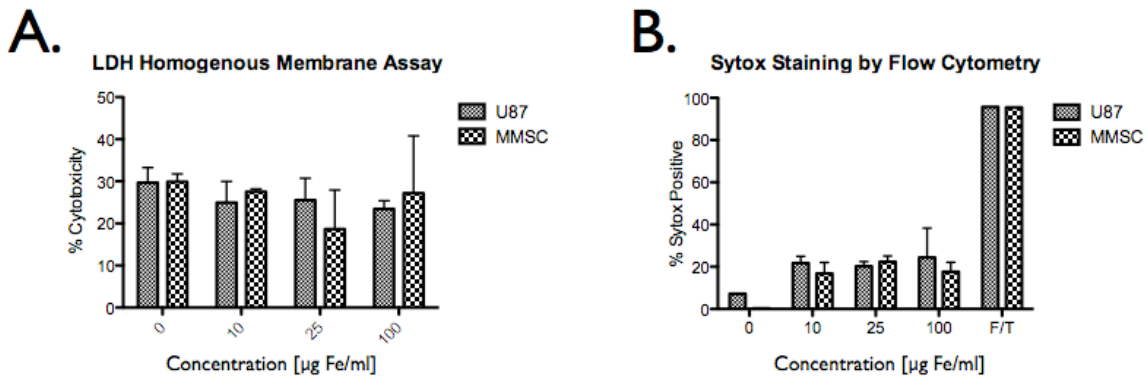

Figure 32. Toxicity assays of ProRho-FH into U87s and MMSCs. A. Cells were loaded with ProRho-FH at varying concentrations, washed and assayed for lactate dehydrogenase release 24 hours later. B. Cells were loaded with ProRho-FH at varying concentrations, and assessed for sytox staining by flow cytometry 24 hours later. A freeze-thaw control is shown for comparison.

It is important that the materials used for cell labeling minimally affect the cells they are attempting to label. We have assessed toxicity of ProRho-FH using trypan blue exclusion, flow cytometry using Sytox staining, and using an LDH membrane integrity assay (Figure 32). After incubation with ProRho-FH cells were trypsinized and then analyzed by trypan blue to test cell viability. No increase in the number of cells stained by trypan blue was found for cells incubated in 25 ug/ml Fe nor 100 ug/ml Fe of ProRho (data not shown). For the Sytox staining assessment cells were incubated in a range of concentrations of ProRho-FH for 2 hours at 37°C and stained by Sytox. There was a small increase in Sytox staining by flow cytometry from unlabeled cells but a part of that could be due to imperfect compensation of the rhodamine from the Sytox FL1

channel. There seems to be little evidence of concentration-dependent toxic response. Toxicity was also assessed using an LDH homogenous membrane assay. LDH is an enzyme found in cell cytoplasm and is released from the cell if the cell membrane is damaged. The release of LDH into the surrounding media is detected by the conversion of resazurin to the fluorescent resorufin and is a measure of cell membrane integrity and cell viability. There was no statistical difference in cytotoxicity between control cells and cells loaded with ProRho-FH. Nevertheless, we chose 25 µg/ml as the optimal concentration for subsequent cell loading experiments, since there was effective loading at that concentration without toxicity.

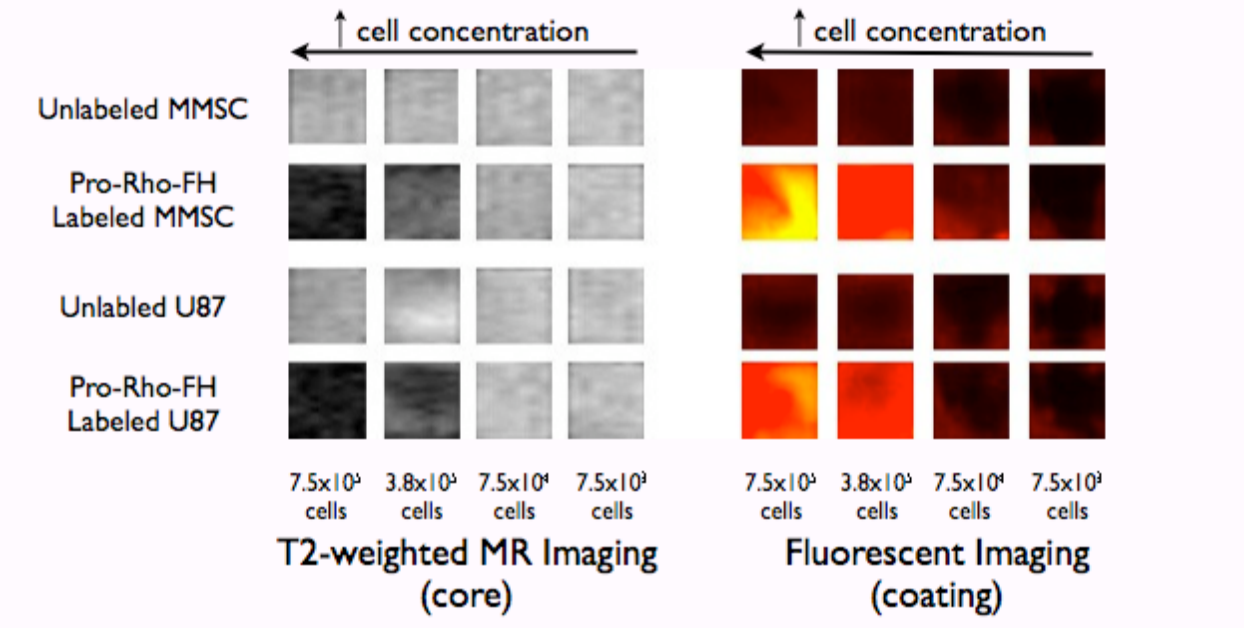

Figure 33. MR and fluorescence imaging of an agar phantom. An agar phantom was prepared with varying densities of loaded and unloaded cells. T2 darkening is observed in the T2 images using an echo time of 180 ms (left). Fluorescence is observed in the same sample in the rhodamine channel (right).

MRI *in vitro* phantom experiments were performed by preparing a range of concentrations of loaded and unloaded cells suspended in agar (Figure 33). Signal intensity reduction for MMSCs was observed for as few as $7.5x10^4$ cells/50 µl. The rhodamine on the

coating of ProRho-FH allows the agar phantom sample to be imaged using fluorescence in addition to MRI, where signal brightening indicates the presence of rhodamine.

Figure 34. In vivo MRI of ProRho-FH-loaded MMSC stereotactically implanted into a mouse brain. The white arrow indicates the location of the implantation.

MMSCs were loaded with ProRho-FH and stereotactically implanted in the brains of mice. A range of numbers of cells were used and even the lowest number of cells, 4,000 cells, are clearly visible on the MR image. Cells did not migrate after 1 week because no tropic factor was introduced (Figure 34).

7.7 Conclusion

Although Feraheme is FDA-approved for iron anemia treatment, it has superparamagnetic properties and has been used in many studies as an MR contrast agent. Its versatility as a nanoparticle has been greatly enhanced by the development of amino-FH, the amine-functionalized version of Feraheme, the production of which has been outlined in Chapter 6 of this dissertation. Amino-FH was covalently combined with protamine here to make a probe that efficiently loads a variety of cell types ex-vivo with superparamagnetic iron oxide for MRI tracking. The cell labeling material ProRho-FH consists of a carboxymethyl dextran superparamagnetic iron oxide nanoparticle with a protein-based membrane translocating agent affixed to a fluorescent dye. Both protamine and FH are FDA approved materials, and short-term acute toxicity studies of cells loaded with versions of these materials have indicated a general lack of toxicity, even at very high concentrations. Protamine was chosen as a membrane translocating agent due to its low cost, proven safety record, and availability in large quantities as GMP approved material. It has previously been reported that protamine combined with Feraheme (ferumoxytol) cannot label cells efficiently,[180] however these studies were performed without the covalent chemistry that is used here. We have also showed that although there is a non-covalent ionic association between protamine and Feraheme, it is not sufficient to shuttle

Feraheme into cells. We have also shown *in vitro* and *in vivo* that these cells can be visualized using MRI.

Although this work is situated in a glioma model because of the great promise of cell therapies in treating cancers of the central nervous system, the potential uses of ProRho-FH is far wider. In this study two commercially available, FDA-approved pharmaceuticals have been covalently coupled to form a cell labeling agent than can be used for a wide range of biological and pathological investigations as well as for the development and evaluation of any disease treatments that involve cell transplantation.

CHAPTER 8: FUTURE WORK

The SPARC-targeted aminoSPARK nanoparticle described in Chapter 4 shows that it is possible to target SPARC in vivo and differentiate between prostate cancer subtypes that are more likely or less likely to metastasize. The next step would be to alter the nanoparticle platform to a more clinically relevant nanoparticle such as Feraheme. This should be a relatively simple task given the chemical handle of the SPARC-targeting peptide and the proven chemical modification possibilities of Feraheme.

The creation of an amine-functionalized Feraheme opens up many possibilities of conjugation to a variety of amine-reactive molecules and many of these will be explored. Among those include FMT imaging using FH-Cy5.5, and combined PET-MRI with DTPA-CyAl5.5-FH. Further experiments with ProRho-FH, the cell-loading nanoparticle, include loading of cells transfected with luciferase so that both bioluminescent and MR imaging can be compared. Various experiments involving the homing properties of the mesenchymal stem cells to regions of pathology can also be carried out. ProRho-FH can play a role in biological investigations of cell migration and development of cell-based therapeutics. Potential drawbacks include the dilution of signal upon cell division, inability to determine the viability of cells from the iron label, and inability to determine whether the iron is still within the cell.

CHAPTER 9: CONCLUSIONS AND SUMMARY OF WORK

This dissertation employs several formulations of polymer-coated iron oxide nanoparticles for medical imaging applications. All nanoparticles were either synthesized in-house or purchased and then modified for specific targeting or reporting functionalities. General chemical methodologies with wide applications to nanomaterial development are presented here alongside an agent for targeting a particular biological protein, showing a large scope of work from creating broadly applicable toolkits to addressing specific clinical problems.

A wide range of medical imaging applications of polymer-coated iron oxide nanoparticles have been presented in this dissertation. Conjugation of a targeting ligand to a nanoparticle that can then find the target is shown as a way to stratify an aggressive form of prostate cancer, a major clinical need. A screening method was presented for optimizing the formulation of polymer-coated iron oxide nanoparticles for maximal relaxivity and stability given the constraints of working with raw materials that are biocompatible to achieve clinically relevant preparations of nanoparticles. The optimal nanoparticle resulting from the screen, a carboxymethyl dextran-coated nanoparticle, was similar in composition to Feraheme, a recently FDA-approved commercially available superparamagnetic polymer-coated iron oxide nanoparticle. An amine-functionalized version of Feraheme was created to facilitate bioconjugation and a variety of different Feraheme-based nanoparticles were synthesized as examples, although there are a multitude of possibilities for other amine-reactive molecules to be

attached to Feraheme. A cell-labeling nanoparticle comprised of Feraheme and protamine, another safe FDA-approved injectable drug, was synthesized. It was shown that this ProRho-FH nanoparticle readily labels cells and can be visualized by both optical methods and MR imaging. ProRho-FH is safe and effective and is an excellent replacement for Feridex-based cell labeling formulations, given that Feridex has recently been discontinued.

It is our hope that this cross-disciplinary contribution will be beneficial to physical scientists, chemists, materials scientists, biologists, medical imaging professionals, and biomedical researchers as they all strive to improve medical imaging technology. Advances in nanoparticle imaging agents will facilitate diagnoses, prognoses, aid in the development of new diagnostic and therapeutic agents, and ultimately improve patient care.

CHAPTER 10: REFERENCES

1. Chen, S. L.; Reynolds, F.; Yu, L. T.; Weissleder, R.; Josephson, L., A screening paradigm for the design of improved polymer-coated superparamagnetic iron oxide nanoparticles. *Journal of Materials Chemistry* **2009,** 19, (35), 6387-6392.

2. Barick, K. C.; Aslam, M.; Lin, Y. P.; Bahadur, D.; Prasad, P. V.; Dravid, V. P., Novel and efficient MR active aqueous colloidal Fe3O4 nanoassemblies. *Journal of Materials Chemistry* **2009,** 19, (38), 7023-7029.

3. Balakrishnan, V. S.; Rao, M.; Kausz, A. T.; Brenner, L.; Pereira, B. J.; Frigo, T. B.; Lewis, J. M., Physicochemical properties of ferumoxytol, a new intravenous iron preparation. *Eur J Clin Invest* **2009,** 39, (6), 489-96.

4. Jung, C. W.; Jacobs, P., Physical and chemical properties of superparamagnetic iron oxide MR contrast agents: ferumoxides, ferumoxtran, ferumoxsil. *Magn Reson Imaging* **1995,** 13, (5), 661-74.

5. Wunderbaldinger, P.; Josephson, L.; Weissleder, R., Crosslinked iron oxides (CLIO): a new platform for the development of targeted MR contrast agents. *Acad Radiol* **2002,** 9 Suppl 2, S304-6.

6. Shen, T.; Weissleder, R.; Papisov, M.; Bogdanov, A., Jr.; Brady, T. J., Monocrystalline iron oxide nanocompounds (MION): physicochemical properties. *Magn Reson Med* **1993,** 29, (5), 599-604.

7. Arbab, A. S.; Bashaw, L. A.; Miller, B. R.; Jordan, E. K.; Bulte, J. W.; Frank, J. A., Intracytoplasmic tagging of cells with ferumoxides and transfection agent for cellular magnetic resonance imaging after cell transplantation: methods and techniques. *Transplantation* **2003,** 76, (7), 1123-30.

8. Alexiou, C.; Schmid, R. J.; Jurgons, R.; Kremer, M.; Wanner, G.; Bergemann, C.; Huenges, E.; Nawroth, T.; Arnold, W.; Parak, F. G., Targeting cancer cells: magnetic nanoparticles as drug carriers. *Eur Biophys J* **2006,** 35, (5), 446-50.

9. Sun, E. Y.; Weissleder, R.; Josephson, L., Continuous analyte sensing with magnetic nanoswitches. *Small* **2006,** 2, (10), 1144-7.

10. Corot, C.; Robert, P.; Idee, J. M.; Port, M., Recent advances in iron oxide nanocrystal technology for medical imaging. *Adv Drug Deliv Rev* **2006,** 58, (14), 1471-504.

11. Denkhaus, E.; Salnikow, K., Nickel essentiality, toxicity, and carcinogenicity. *Crit Rev Oncol Hematol* **2002,** 42, (1), 35-56.

12. Haynes, D. R.; Crotti, T. N.; Haywood, M. R., Corrosion of and changes in biological effects of cobalt chrome alloy and 316L stainless steel prosthetic particles with age. *J Biomed Mater Res* **2000,** 49, (2), 167-75.

13. Harisinghani, M. G.; Barentsz, J.; Hahn, P. F.; Deserno, W. M.; Tabatabaei, S.; van de Kaa, C. H.; de la Rosette, J.; Weissleder, R., Noninvasive detection of clinically occult lymph-node metastases in prostate cancer. *N Engl J Med* **2003,** 348, (25), 2491-9.

14. Krause, M. H.; Kwong, K. K.; Gragoudas, E. S.; Young, L. H., MRI of blood volume with superparamagnetic iron in choroidal melanoma treated with thermotherapy. *Magn Reson Imaging* **2004,** 22, (6), 779-87.

15. Hilger, I.; Hiergeist, R.; Hergt, R.; Winnefeld, K.; Schubert, H.; Kaiser, W. A., Thermal ablation of tumors using magnetic nanoparticles: an in vivo feasibility study. *Invest Radiol* **2002,** 37, (10), 580-6.

16. McCarthy, J. R.; Jaffer, F. A.; Weissleder, R., A macrophage-targeted theranostic nanoparticle for biomedical applications. *Small* **2006,** 2, (8-9), 983-7.

17. Jurgons, R.; Seliger, C.; Hilpert, A.; Trahms, L.; Odenbach, S.; Alexiou, C., Drug loaded magnetic nanoparticles for cancer therapy. *Journal of Physics-Condensed Matter* **2006,** 18, (38), S2893-S2902.

18. Chambon, C.; Clement, O.; Le Blanche, A.; Schouman-Claeys, E.; Frija, G., Superparamagnetic iron oxides as positive MR contrast agents: in vitro and in vivo evidence. *Magn Reson Imaging* **1993,** 11, (4), 509-19.

19. Canet, E.; Revel, D.; Forrat, R.; Baldy-Porcher, C.; de Lorgeril, M.; Sebbag, L.; Vallee, J. P.; Didier, D.; Amiel, M., Superparamagnetic iron oxide particles and positive enhancement for myocardial perfusion studies assessed by subsecond T1-weighted MRI. *Magn Reson Imaging* **1993,** 11, (8), 1139-45.

20. Bourrinet, P.; Bengele, H. H.; Bonnemain, B.; Dencausse, A.; Idee, J. M.; Jacobs, P. M.; Lewis, J. M., Preclinical safety and pharmacokinetic profile of ferumoxtran-10, an ultrasmall superparamagnetic iron oxide magnetic resonance contrast agent. *Invest Radiol* **2006,** 41, (3), 313-24.

21. Leenders, W., Ferumoxtran-10 Advanced Magnetics. *IDrugs* **2003,** 6, (10), 987-93.

22. Metz, S.; Lohr, S.; Settles, M.; Beer, A.; Woertler, K.; Rummeny, E. J.; Daldrup-Link, H. E., Ferumoxtran-10-enhanced MR imaging of the bone marrow before and after conditioning therapy in patients with non-Hodgkin lymphomas. *Eur Radiol* **2006,** 16, (3), 598-607.

23. Clement, O.; Siauve, N.; Cuenod, C. A.; Frija, G., Liver imaging with ferumoxides (Feridex): fundamentals, controversies, and practical aspects. *Top Magn Reson Imaging* **1998,** 9, (3), 167-82.

24. Schulze, E.; Ferrucci, J. T., Jr.; Poss, K.; Lapointe, L.; Bogdanova, A.; Weissleder, R., Cellular uptake and trafficking of a prototypical magnetic iron oxide label in vitro. *Invest Radiol* **1995,** 30, (10), 604-10.

25. Thorek, D. L.; Chen, A. K.; Czupryna, J.; Tsourkas, A., Superparamagnetic iron oxide nanoparticle probes for molecular imaging. *Ann Biomed Eng* **2006,** 34, (1), 23-38.

26. Riordan, M.; Rylance, G.; Berry, K., Poisoning in children 3: common medicines. *Arch Dis Child* **2002,** 87, (5), 400-2.

27. Lu, A. H.; Salabas, E. L.; Schuth, F., Magnetic nanoparticles: synthesis, protection, functionalization, and application. *Angew Chem Int Ed Engl* **2007,** 46, (8), 1222-44.

28. Tartaj, P.; Serna, C. J., Synthesis of monodisperse superparamagnetic Fe/silica nanospherical composites. *J Am Chem Soc* **2003,** 125, (51), 15754-5.

29. Babes, L.; Denizot, B.; Tanguy, G.; Le Jeune, J. J.; Jallet, P., Synthesis of Iron Oxide Nanoparticles Used as MRI Contrast Agents: A Parametric Study. *J Colloid Interface Sci* **1999,** 212, (2), 474-482.

30. Osaka, T.; Matsunaga, T.; Nakanishi, T.; Arakaki, A.; Niwa, D.; Iida, H., Synthesis of magnetic nanoparticles and their application to bioassays. *Anal Bioanal Chem* **2006,** 384, (3), 593-600.

31. Lang, X. Y.; Zheng, W. T.; Jiang, Q., Size and interface effects on ferromagnetic and antiferromagnetic transition temperatures. *Physical Review B* **2006,** 73, (22), -.

32. Brust, M.; Walker, M.; Bethell, D.; Schiffrin, D. J.; Whyman, R., Synthesis of Thiol-Derivatized Gold Nanoparticles in a 2-Phase Liquid-Liquid System. *Journal of the Chemical Society-Chemical Communications* **1994**, (7), 801-802.

33. Templeton, A. C.; Wuelfing, M. P.; Murray, R. W., Monolayer protected cluster molecules. *Accounts of Chemical Research* **2000,** 33, (1), 27-36.

34. Nakamura, K.; Kawabata, T.; Mori, Y., Size distribution analysis of colloidal gold by small angle X-ray scattering and light absorbance. *Powder Technology* **2003,** 131, (2-3), 120-128.

35. Cleveland, C. L.; Landman, U.; Schaaff, T. G.; Shafigullin, M. N.; Stephens, P. W.; Whetten, R. L., Structural evolution of smaller gold nanocrystals: The truncated decahedral motif. *Physical Review Letters* **1997,** 79, (10), 1873-1876.

36. Leff, D. V.; Ohara, P. C.; Heath, J. R.; Gelbart, W. M., Thermodynamic Control of Gold Nanocrystal Size - Experiment and Theory. *Journal of Physical Chemistry* **1995,** 99, (18), 7036-7041.

37. Lee, I.; Chan, K. Y.; Phillips, D. L., Atomic force microscopy of platinum nanoparticles prepared on highly oriented pyrolytic graphite. *Ultramicroscopy* **1998,** 75, (2), 69-76.

38. Harrell, L. E.; Bigioni, T. P.; Cullen, W. G.; Whetten, R. L.; First, P. N., Scanning tunneling microscopy of passivated Au nanocrystals immobilized on Au(111) surface. *Journal of Vacuum Science & Technology B* **1999,** 17, (6), 2411-2416.

39. Reynolds, F.; O'Loughlin, T.; Weissleder, R.; Josephson, L., Method of determining nanoparticle core weight. *Anal Chem* **2005,** 77, (3), 814-7.

40. Denizot, B.; Tanguy, G.; Hindre, F.; Rump, E.; Jacques Le Jeune, J.; Jallet, P., Phosphorylcholine Coating of Iron Oxide Nanoparticles. *J Colloid Interface Sci* **1999,** 209, (1), 66-71.

41. Bulte, J. W.; Douglas, T.; Witwer, B.; Zhang, S. C.; Strable, E.; Lewis, B. K.; Zywicke, H.; Miller, B.; van Gelderen, P.; Moskowitz, B. M.; Duncan, I. D.; Frank, J. A., Magnetodendrimers allow endosomal magnetic labeling and in vivo tracking of stem cells. *Nat Biotechnol* **2001,** 19, (12), 1141-7.

42. Wilhelm, C.; Billotey, C.; Roger, J.; Pons, J. N.; Bacri, J. C.; Gazeau, F., Intracellular uptake of anionic superparamagnetic nanoparticles as a function of their surface coating. *Biomaterials* **2003,** 24, (6), 1001-11.

43. Kellar, K. E.; Fujii, D. K.; Gunther, W. H.; Briley-Saebo, K.; Bjornerud, A.; Spiller, M.; Koenig, S. H., NC100150 Injection, a preparation of optimized iron oxide nanoparticles for positive-contrast MR angiography. *J Magn Reson Imaging* **2000,** 11, (5), 488-94.

44. Illum, L.; Church, A. E.; Butterworth, M. D.; Arien, A.; Whetstone, J.; Davis, S. S., Development of systems for targeting the regional lymph nodes for diagnostic imaging: in vivo behaviour of colloidal PEG-coated magnetite nanospheres in the rat following interstitial administration. *Pharm Res* **2001,** 18, (5), 640-5.

45. Moffat, B. A.; Reddy, G. R.; McConville, P.; Hall, D. E.; Chenevert, T. L.; Kopelman, R. R.; Philbert, M.; Weissleder, R.; Rehemtulla, A.; Ross, B. D., A novel polyacrylamide magnetic nanoparticle contrast agent for molecular imaging using MRI. *Mol Imaging* **2003,** 2, (4), 324-32.

46. Jung, C. W., Surface properties of superparamagnetic iron oxide MR contrast agents: ferumoxides, ferumoxtran, ferumoxsil. *Magn Reson Imaging* **1995,** 13, (5), 675-91.

47. Kim, D. K.; Zhang, Y.; Kehr, J.; Klason, T.; Bjelke, B.; Muhammed, M., Characterization and MRI study of surfactant-coated superparamagnetic nanoparticles administered into the rat brain. *Journal of Magnetism and Magnetic Materials* **2001,** 225, (1-2), 256-261.

48. Rydland, J.; BjOrnerud, A.; Haugen, O.; Torheim, G.; Torres, C.; Kvistad, K. A.; Haraldseth, O., New intravascular contrast agent applied to dynamic contrast enhanced MR imaging of human breast cancer. *Acta Radiol* **2003,** 44, (3), 275-83.

49. Trivedi, R. A.; JM, U. K.-I.; Graves, M. J.; Kirkpatrick, P. J.; Gillard, J. H., Noninvasive imaging of carotid plaque inflammation. *Neurology* **2004,** 63, (1), 187-8.

50. Enochs, W. S.; Harsh, G.; Hochberg, F.; Weissleder, R., Improved delineation of human brain tumors on MR images using a long-circulating, superparamagnetic iron oxide agent. *J Magn Reson Imaging* **1999,** 9, (2), 228-32.

51. LesliePelecky, D. L.; Rieke, R. D., Magnetic properties of nanostructured materials. *Chemistry of Materials* **1996,** 8, (8), 1770-1783.

52. Pankhurst, Q. A.; Connolly, J.; Jones, S. K.; Dobson, J., Applications of magnetic nanoparticles in biomedicine. *Journal of Physics D-Applied Physics* **2003,** 36, (13), R167-R181.

53. Morales, M. P.; Bomati-Miguel, O.; de Alejo, R. P.; Ruiz-Cabello, J.; Veintemillas-Verdaguer, S.; O'Grady, K., Contrast agents for MRI based on iron oxide nanoparticles prepared by laser pyrolysis. *Journal of Magnetism and Magnetic Materials* **2003,** 266, (1-2), 102-109.

54. Sjogren, C. E.; Johansson, C.; Naevestad, A.; Sontum, P. C.; Briley-Saebo, K.; Fahlvik, A. K., Crystal size and properties of superparamagnetic iron oxide (SPIO) particles. *Magn Reson Imaging* **1997,** 15, (1), 55-67.

55. Weissleder, R.; Elizondo, G.; Wittenberg, J.; Rabito, C. A.; Bengele, H. H.; Josephson, L., Ultrasmall superparamagnetic iron oxide: characterization of a new class of contrast agents for MR imaging. *Radiology* **1990,** 175, (2), 489-93.

56. Wang, Y. X.; Hussain, S. M.; Krestin, G. P., Superparamagnetic iron oxide contrast agents: physicochemical characteristics and applications in MR imaging. *Eur Radiol* **2001,** 11, (11), 2319-31.

57. LaConte, L. E. W.; Nitin, N.; Zurkiya, O.; Caruntu, D.; O'Connor, C. J.; Hu, X. P.; Bao, G., Coating thickness of magnetic iron oxide nanoparticles affects R-2 relaxivity. *Journal of Magnetic Resonance Imaging* **2007,** 26, (6), 1634-1641.

58. Jemal, A.; Siegel, R.; Ward, E.; Murray, T.; Xu, J.; Thun, M. J., Cancer statistics, 2007. *CA Cancer J Clin* **2007,** 57, (1), 43-66.

59. Kirby, R. S.; Andersen, M.; Gratzke, P.; Dahlstrand, C.; Hoye, K., A combined analysis of double-blind trials of the efficacy and tolerability of doxazosin-gastrointestinal therapeutic system, doxazosin standard and placebo in patients with benign prostatic hyperplasia. *BJU Int* **2001,** 87, (3), 192-200.

60. Bill-Axelson, A.; Holmberg, L.; Ruutu, M.; Haggman, M.; Andersson, S. O.; Bratell, S.; Spangberg, A.; Busch, C.; Nordling, S.; Garmo, H.; Palmgren, J.; Adami, H. O.; Norlen, B. J.; Johansson, J. E., Radical prostatectomy versus watchful waiting in early prostate cancer. *N Engl J Med* **2005,** 352, (19), 1977-84.

61. D'Amico, A. V.; Whittington, R.; Malkowicz, S. B.; Cote, K.; Loffredo, M.; Schultz, D.; Chen, M. H.; Tomaszewski, J. E.; Renshaw, A. A.; Wein, A.; Richie, J. P., Biochemical outcome after radical prostatectomy or external beam radiation therapy for patients with clinically localized prostate carcinoma in the prostate specific antigen era. *Cancer* **2002,** 95, (2), 281-6.

62. Delongchamps, N. B.; Singh, A.; Haas, G. P., The role of prevalence in the diagnosis of prostate cancer. *Cancer Control* **2006,** 13, (3), 158-68.

63. Sakr, W. A.; Sarkar, F. H.; Sreepathi, P.; Drozdowicz, S.; Crissman, J. D., Measurement of cellular proliferation in human prostate by AgNOR, PCNA, and SPF. *Prostate* **1993,** 22, (2), 147-54.

64. Yatani, R.; Chigusa, I.; Akazaki, K.; Stemmermann, G. N.; Welsh, R. A.; Correa, P., Geographic pathology of latent prostatic carcinoma. *Int J Cancer* **1982,** 29, (6), 611-6.

65. Sakr, W. A.; Haas, G. P.; Cassin, B. F.; Pontes, J. E.; Crissman, J. D., The frequency of carcinoma and intraepithelial neoplasia of the prostate in young male patients. *J Urol* **1993,** 150, (2 Pt 1), 379-85.

66. Thompson, I. M.; Pauler, D. K.; Goodman, P. J.; Tangen, C. M.; Lucia, M. S.; Parnes, H. L.; Minasian, L. M.; Ford, L. G.; Lippman, S. M.; Crawford, E. D.; Crowley, J. J.; Coltman, C. A., Jr., Prevalence of prostate cancer among men with a prostate-specific antigen level < or =4.0 ng per milliliter. *N Engl J Med* **2004,** 350, (22), 2239-46.

67. Hernandez, J.; Thompson, I. M., Prostate-specific antigen: a review of the validation of the most commonly used cancer biomarker. *Cancer* **2004,** 101, (5), 894-904.

68. Grimm, M. O.; Hartmann, F. H.; Schulz, W. A., [Microarrays]. *Urologe A* **2004,** 43, (6), 653-8.

69. Brekken, R. A.; Sage, E. H., SPARC, a matricellular protein: at the crossroads of cell-matrix communication. *Matrix Biol* **2001,** 19, (8), 816-27.

70. Framson, P. E.; Sage, E. H., SPARC and tumor growth: where the seed meets the soil? *J Cell Biochem* **2004,** 92, (4), 679-90.

71. Lane, T. F.; Sage, E. H., The biology of SPARC, a protein that modulates cell-matrix interactions. *Faseb J* **1994,** 8, (2), 163-73.

72. Murphy-Ullrich, J. E.; Lane, T. F.; Pallero, M. A.; Sage, E. H., SPARC mediates focal adhesion disassembly in endothelial cells through a follistatin-like region and the Ca(2+)-binding EF-hand. *J Cell Biochem* **1995,** 57, (2), 341-50.

73. Lane, T. F.; Sage, E. H., Functional mapping of SPARC: peptides from two distinct Ca+(+)-binding sites modulate cell shape. *J Cell Biol* **1990,** 111, (6 Pt 2), 3065-76.

74. Sage, E. H., Terms of attachment: SPARC and tumorigenesis. *Nat Med* **1997,** 3, (2), 144-6.

75. Goldblum, S. E.; Ding, X.; Funk, S. E.; Sage, E. H., SPARC (secreted protein acidic and rich in cysteine) regulates endothelial cell shape and barrier function. *Proc Natl Acad Sci U S A* **1994,** 91, (8), 3448-52.

76. Kelly, K. A.; Allport, J. R.; Yu, A. M.; Sinh, S.; Sage, E. H.; Gerszten, R. E.; Weissleder, R., SPARC is a VCAM-1 counter-ligand that mediates leukocyte transmigration. *J Leukoc Biol* **2007,** 81, (3), 748-56.

77. Alvarez, M. J.; Prada, F.; Salvatierra, E.; Bravo, A. I.; Lutzky, V. P.; Carbone, C.; Pitossi, F. J.; Chuluyan, H. E.; Podhajcer, O. L., Secreted protein acidic and rich in cysteine produced by human melanoma cells modulates polymorphonuclear leukocyte recruitment and antitumor cytotoxic capacity. *Cancer Res* **2005,** 65, (12), 5123-32.

78. Thomas, R.; True, L. D.; Bassuk, J. A.; Lange, P. H.; Vessella, R. L., Differential expression of osteonectin/SPARC during human prostate cancer progression. *Clin Cancer Res* **2000,** 6, (3), 1140-9.

79. Jacob, K.; Webber, M.; Benayahu, D.; Kleinman, H. K., Osteonectin promotes prostate cancer cell migration and invasion: a possible mechanism for metastasis to bone. *Cancer Res* **1999,** 59, (17), 4453-7.

80. De, S.; Chen, J.; Narizhneva, N. V.; Heston, W.; Brainard, J.; Sage, E. H.; Byzova, T. V., Molecular pathway for cancer metastasis to bone. *J Biol Chem* **2003,** 278, (40), 39044-50.

81. Fidler, I. J., The pathogenesis of cancer metastasis: the 'seed and soil' hypothesis revisited. *Nat Rev Cancer* **2003,** 3, (6), 453-8.

82. Mok, S. C.; Chan, W. Y.; Wong, K. K.; Muto, M. G.; Berkowitz, R. S., SPARC, an extracellular matrix protein with tumor-suppressing activity in human ovarian epithelial cells. *Oncogene* **1996,** 12, (9), 1895-901.

83. Lopez, M. V.; Blanco, P.; Viale, D. L.; Cafferata, E. G.; Carbone, C.; Gould, D.; Chernajovsky, Y.; Podhajcer, O. L., Expression of a suicidal gene under control of the human secreted protein acidic and rich in cysteine (SPARC) promoter in tumor or stromal cells led to the inhibition of tumor cell growth. *Mol Cancer Ther* **2006,** 5, (10), 2503-11.

84. Kerbel, R. S., Expression of multi-cytokine resistance and multi-growth factor independence in advanced stage metastatic cancer. Malignant melanoma as a paradigm. *Am J Pathol* **1992,** 141, (3), 519-24.

85. Kang, H. W.; Josephson, L.; Petrovsky, A.; Weissleder, R.; Bogdanov, A., Magnetic resonance imaging of inducible e-selectin expression in human endothelial cell culture. *Bioconjug Chem* **2002,** 13, (1), 122-7.

86. Weissleder, R.; Lee, A. S.; Fischman, A. J.; Reimer, P.; Shen, T.; Wilkinson, R.; Callahan, R. J.; Brady, T. J., Polyclonal human immunoglobulin G labeled with polymeric iron oxide: antibody MR imaging. *Radiology* **1991,** 181, (1), 245-9.

87. Weissleder, R.; Lee, A. S.; Khaw, B. A.; Shen, T.; Brady, T. J., Antimyosin-labeled monocrystalline iron oxide allows detection of myocardial infarct: MR antibody imaging. *Radiology* **1992,** 182, (2), 381-5.

88. Kelly, K. A.; Waterman, P.; Weissleder, R., In vivo imaging of molecularly targeted phage. *Neoplasia* **2006,** 8, (12), 1011-8.

89. Ruijter, E.; van Leenders, G.; Miller, G.; Debruyne, F.; van de Kaa, C., Errors in histological grading by prostatic needle biopsy specimens: frequency and predisposing factors. *J Pathol* **2000,** 192, (2), 229-33.

90. Bill-Axelson, A.; Holmberg, L.; Filen, F.; Ruutu, M.; Garmo, H.; Busch, C.; Nordling, S.; Haggman, M.; Andersson, S. O.; Bratell, S.; Spangberg, A.; Palmgren, J.; Adami, H. O.; Johansson, J. E., Radical prostatectomy versus watchful waiting in localized prostate cancer: the Scandinavian prostate cancer group-4 randomized trial. *J Natl Cancer Inst* **2008,** 100, (16), 1144-54.

91. Gandon, Y.; Heautot, J. F.; Brunet, F.; Guyader, D.; Deugnier, Y.; Carsin, M., Superparamagnetic iron oxide: clinical time-response study. *Eur J Radiol* **1991,** 12, (3), 195-200.

92. Everitt, E. A.; Sage, E. H., Overexpression of SPARC in stably transfected F9 cells mediates attachment and spreading in Ca(2+)-deficient medium. *Biochem Cell Biol* **1992,** 70, (12), 1368-79.

93. Funk, S. E.; Sage, E. H., Differential effects of SPARC and cationic SPARC peptides on DNA synthesis by endothelial cells and fibroblasts. *J Cell Physiol* **1993,** 154, (1), 53-63.

94. Funk, S. E.; Sage, E. H., The Ca2(+)-binding glycoprotein SPARC modulates cell cycle progression in bovine aortic endothelial cells. *Proc Natl Acad Sci U S A* **1991,** 88, (7), 2648-52.

95. Sage, E. H.; Vernon, R. B., Regulation of angiogenesis by extracellular matrix: the growth and the glue. *J Hypertens Suppl* **1994,** 12, (10), S145-52.

96. Hasselaar, P.; Loskutoff, D. J.; Sawdey, M.; Sage, E. H., SPARC induces the expression of type 1 plasminogen activator inhibitor in cultured bovine aortic endothelial cells. *J Biol Chem* **1991,** 266, (20), 13178-84.

97. Tremble, P. M.; Lane, T. F.; Sage, E. H.; Werb, Z., SPARC, a secreted protein associated with morphogenesis and tissue remodeling, induces expression of metalloproteinases in fibroblasts through a novel extracellular matrix-dependent pathway. *J Cell Biol* **1993,** 121, (6), 1433-44.

98. Thiery, J. P., Epithelial-mesenchymal transitions in tumour progression. *Nat Rev Cancer* **2002,** 2, (6), 442-54.

99. Tran, N. L.; Nagle, R. B.; Cress, A. E.; Heimark, R. L., N-Cadherin expression in human prostate carcinoma cell lines. An epithelial-mesenchymal transformation mediating adhesion withStromal cells. *Am J Pathol* **1999,** 155, (3), 787-98.

100. Robert, G.; Gaggioli, C.; Bailet, O.; Chavey, C.; Abbe, P.; Aberdam, E.; Sabatie, E.; Cano, A.; Garcia de Herreros, A.; Ballotti, R.; Tartare-Deckert, S., SPARC represses E-cadherin and induces mesenchymal transition during melanoma development. *Cancer Res* **2006,** 66, (15), 7516-23.

101. Clark, C. J.; Sage, E. H., A prototypic matricellular protein in the tumor microenvironment--where there's SPARC, there's fire. *J Cell Biochem* **2008,** 104, (3), 721-32.

102. Lapointe, J.; Li, C.; Higgins, J. P.; van de Rijn, M.; Bair, E.; Montgomery, K.; Ferrari, M.; Egevad, L.; Rayford, W.; Bergerheim, U.; Ekman, P.; DeMarzo, A. M.; Tibshirani, R.; Botstein, D.; Brown, P. O.; Brooks, J. D.; Pollack, J. R., Gene expression profiling identifies clinically relevant subtypes of prostate cancer. *Proc Natl Acad Sci U S A* **2004,** 101, (3), 811-6.

103. Nelson, A. R.; Fingleton, B.; Rothenberg, M. L.; Matrisian, L. M., Matrix metalloproteinases: biologic activity and clinical implications. *J Clin Oncol* **2000,** 18, (5), 1135-49.

104. Langer, R.; Wang, M.; Stepkowski, S. M.; Hancock, W. W.; Han, R.; Li, P.; Feng, L.; Kirken, R. A.; Berens, K. L.; Dupre, B.; Podder, H.; Dixon, R. A.; Kahan, B. D., Selectin inhibitor bimosiamose prolongs survival of kidney allografts by reduction in intragraft production of cytokines and chemokines. *J Am Soc Nephrol* **2004,** 15, (11), 2893-901.

105. Rhodes, D. R.; Yu, J.; Shanker, K.; Deshpande, N.; Varambally, R.; Ghosh, D.; Barrette, T.; Pandey, A.; Chinnaiyan, A. M., ONCOMINE: a cancer microarray database and integrated data-mining platform. *Neoplasia* **2004,** 6, (1), 1-6.

106. Banyard, J.; Zetter, B. R., The role of cell motility in prostate cancer. *Cancer Metastasis Rev* **1998,** 17, (4), 449-58.

107. Bangma, C. H.; Roemeling, S.; Schroder, F. H., Overdiagnosis and overtreatment of early detected prostate cancer. *World J Urol* **2007,** 25, (1), 3-9.

108. Paley, P. J.; Goff, B. A.; Gown, A. M.; Greer, B. E.; Sage, E. H., Alterations in SPARC and VEGF immunoreactivity in epithelial ovarian cancer. *Gynecol Oncol* **2000,** 78, (3 Pt 1), 336-41.

109. Iacobuzio-Donahue, C. A.; Argani, P.; Hempen, P. M.; Jones, J.; Kern, S. E., The desmoplastic response to infiltrating breast carcinoma: gene expression at the site of primary invasion and implications for comparisons between tumor types. *Cancer Res* **2002,** 62, (18), 5351-7.

110. Koukourakis, M. I.; Giatromanolaki, A.; Brekken, R. A.; Sivridis, E.; Gatter, K. C.; Harris, A. L.; Sage, E. H., Enhanced expression of SPARC/osteonectin in the tumor-associated stroma of non-small cell lung cancer is correlated with markers of hypoxia/acidity and with poor prognosis of patients. *Cancer Res* **2003,** 63, (17), 5376-80.

111. Bloomston, M.; Ellison, E. C.; Muscarella, P.; Al-Saif, O.; Martin, E. W.; Melvin, W. S.; Frankel, W. L., Stromal osteonectin overexpression is associated with poor outcome in patients with ampullary cancer. *Ann Surg Oncol* **2007,** 14, (1), 211-7.

112. Xue, L. Y.; Hu, N.; Song, Y. M.; Zou, S. M.; Shou, J. Z.; Qian, L. X.; Ren, L. Q.; Lin, D. M.; Tong, T.; He, Z. G.; Zhan, Q. M.; Taylor, P. R.; Lu, N., Tissue microarray analysis reveals a tight correlation between protein expression pattern and progression of esophageal squamous cell carcinoma. *BMC Cancer* **2006,** 6, 296.

113. Alonso, S. R.; Tracey, L.; Ortiz, P.; Perez-Gomez, B.; Palacios, J.; Pollan, M.; Linares, J.; Serrano, S.; Saez-Castillo, A. I.; Sanchez, L.; Pajares, R.; Sanchez-Aguilera, A.; Artiga, M. J.; Piris, M. A.; Rodriguez-Peralto, J. L., A high-throughput study in melanoma identifies epithelial-mesenchymal transition as a major determinant of metastasis. *Cancer Res* **2007,** 67, (7), 3450-60.

114. Cunha, G. R.; Hayward, S. W.; Wang, Y. Z., Role of stroma in carcinogenesis of the prostate. *Differentiation* **2002,** 70, (9-10), 473-85.

115. Fishbane, S.; Ungureanu, V. D.; Maesaka, J. K.; Kaupke, C. J.; Lim, V.; Wish, J., The safety of intravenous iron dextran in hemodialysis patients. *Am J Kidney Dis* **1996,** 28, (4), 529-34.

116. Wallerstein, R. O., Intravenous iron-dextran complex. *Blood* **1968,** 32, (4), 690-5.

117. Pittet, M. J.; Swirski, F. K.; Reynolds, F.; Josephson, L.; Weissleder, R., Labeling of immune cells for in vivo imaging using magnetofluorescent nanoparticles. *Nat Protoc* **2006,** 1, (1), 73-9.

118. Arbab, A. S.; Liu, W.; Frank, J. A., Cellular magnetic resonance imaging: current status and future prospects. *Expert Rev Med Devices* **2006,** 3, (4), 427-39.

119. Molday, R. S.; MacKenzie, D., Immunospecific ferromagnetic iron-dextran reagents for the labeling and magnetic separation of cells. *J Immunol Methods* **1982,** 52, (3), 353-67.

120. Wallerstein, R. O.; Hoag, M. S., Treatment with iron-dextran of iron-deficiency anemia in children. *J Am Med Assoc* **1957,** 164, (9), 962-6.

121. Ljungstrom, K. G.; Renck, H.; Strandberg, K.; Hedin, H.; Richter, W.; Widerlov, E., Adverse reactions to dextran in Sweden 1970-1979. *Acta Chir Scand* **1983,** 149, (3), 253-62.

122. Shimada, A., Adverse reactions to total-dose infusion of iron dextran. *Clin Pharm* **1982,** 1, (3), 248-9.

123. Lee, J. H.; Huh, Y. M.; Jun, Y. W.; Seo, J. W.; Jang, J. T.; Song, H. T.; Kim, S.; Cho, E. J.; Yoon, H. G.; Suh, J. S.; Cheon, J., Artificially engineered magnetic nanoparticles for ultra-sensitive molecular imaging. *Nat Med* **2007,** 13, (1), 95-9.

124. Massart, R., Preparation of aqueous magnetic liquids in alkaline and acidic media. *IEEE Trans. Magn.* **1981,** 17, (2), 1247-8.

125. Sosnovik, D. E.; Schellenberger, E. A.; Nahrendorf, M.; Novikov, M. S.; Matsui, T.; Dai, G.; Reynolds, F.; Grazette, L.; Rosenzweig, A.; Weissleder, R.; Josephson, L., Magnetic resonance imaging of cardiomyocyte apoptosis with a novel magneto-optical nanoparticle. *Magn Reson Med* **2005,** 54, (3), 718-24.

126. Reynolds, F.; Weissleder, R.; Josephson, L., Protamine as an efficient membrane-translocating peptide. *Bioconjug Chem* **2005,** 16, (5), 1240-5.

127. Funovics, M.; Montet, X.; Reynolds, F.; Weissleder, R.; Josephson, L., Nanoparticles for the optical imaging of tumor E-selectin. *Neoplasia* **2005,** 7, (10), 904-11.

128. Montet, X.; Weissleder, R.; Josephson, L., Imaging pancreatic cancer with a peptide-nanoparticle conjugate targeted to normal pancreas. *Bioconjug Chem* **2006,** 17, (4), 905-11.

129. Hong, R.; Cima, M. J.; Weissleder, R.; Josephson, L., Magnetic microparticle aggregation for viscosity determination by MR. *Magn Reson Med* **2008,** 59, (3), 515-20.

130. Sanghvi, A. B.; Miller, K. P.; Belcher, A. M.; Schmidt, C. E., Biomaterials functionalization using a novel peptide that selectively binds to a conducting polymer. *Nat Mater* **2005,** 4, (6), 496-502.

131. Whaley, S. R.; English, D. S.; Hu, E. L.; Barbara, P. F.; Belcher, A. M., Selection of peptides with semiconductor binding specificity for directed nanocrystal assembly. *Nature* **2000,** 405, (6787), 665-8.

132. Weissleder, R.; Kelly, K.; Sun, E. Y.; Shtatland, T.; Josephson, L., Cell-specific targeting of nanoparticles by multivalent attachment of small molecules. *Nat Biotechnol* **2005,** 23, (11), 1418-23.

133. Akinc, A.; Lynn, D. M.; Anderson, D. G.; Langer, R., Parallel synthesis and biophysical characterization of a degradable polymer library for gene delivery. *J Am Chem Soc* **2003,** 125, (18), 5316-23.

134. Garanger, E.; Weissleder, R.; Josephson, L., A multifunctional single-attachment-point reagent for controlled protein biotinylation. *Bioconjug Chem* **2009,** 20, (1), 170-3.

135. Josephson, L.; Tung, C. H.; Moore, A.; Weissleder, R., High-efficiency intracellular magnetic labeling with novel superparamagnetic-Tat peptide conjugates. *Bioconjug Chem* **1999,** 10, (2), 186-91.

136. Saksena, M. A.; Saokar, A.; Harisinghani, M. G., Lymphotropic nanoparticle enhanced MR imaging (LNMRI) technique for lymph node imaging. *Eur J Radiol* **2006,** 58, (3), 367-74.

137. Ros, P. R.; Freeny, P. C.; Harms, S. E.; Seltzer, S. E.; Davis, P. L.; Chan, T. W.; Stillman, A. E.; Muroff, L. R.; Runge, V. M.; Nissenbaum, M. A.; et al., Hepatic MR imaging with ferumoxides: a multicenter clinical trial of the safety and efficacy in the detection of focal hepatic lesions. *Radiology* **1995,** 196, (2), 481-8.

138. Reimer, P.; Balzer, T., Ferucarbotran (Resovist): a new clinically approved RES-specific contrast agent for contrast-enhanced MRI of the liver: properties, clinical development, and applications. *Eur Radiol* **2003,** 13, (6), 1266-76.

139. Spinowitz, B. S.; Schwenk, M. H.; Jacobs, P. M.; Bolton, W. K.; Kaplan, M. R.; Charytan, C.; Galler, M., The safety and efficacy of ferumoxytol therapy in anemic chronic kidney disease patients. *Kidney Int* **2005,** 68, (4), 1801-7.

140. McCarthy, J. R.; Kelly, K. A.; Sun, E. Y.; Weissleder, R., Targeted delivery of multifunctional magnetic nanoparticles. *Nanomed* **2007,** 2, (2), 153-67.

141. Arbab, A. S.; Yocum, G. T.; Kalish, H.; Jordan, E. K.; Anderson, S. A.; Khakoo, A. Y.; Read, E. J.; Frank, J. A., Efficient magnetic cell labeling with protamine sulfate complexed to ferumoxides for cellular MRI. *Blood* **2004,** 104, (4), 1217-23.

142. Lewin, M.; Carlesso, N.; Tung, C. H.; Tang, X. W.; Cory, D.; Scadden, D. T.; Weissleder, R., Tat peptide-derivatized magnetic nanoparticles allow in vivo tracking and recovery of progenitor cells. *Nat Biotechnol* **2000,** 18, (4), 410-4.

143. Garanger, E.; Blois, J.; Hilderbrand, S. A.; Shao, F.; Josephson, L., Divergent oriented synthesis for the design of reagents for protein conjugation. *J Comb Chem* 12, (1), 57-64.

144. Grossman, S. A.; Batara, J. F., Current management of glioblastoma multiforme. *Semin Oncol* **2004,** 31, (5), 635-44.

145. Thu, M. S.; Najbauer, J.; Kendall, S. E.; Harutyunyan, I.; Sangalang, N.; Gutova, M.; Metz, M. Z.; Garcia, E.; Frank, R. T.; Kim, S. U.; Moats, R. A.; Aboody, K. S., Iron labeling and pre-clinical MRI visualization of therapeutic human neural stem cells in a murine glioma model. *PLoS One* **2009,** 4, (9), e7218.

146. Aboody, K. S.; Brown, A.; Rainov, N. G.; Bower, K. A.; Liu, S.; Yang, W.; Small, J. E.; Herrlinger, U.; Ourednik, V.; Black, P. M.; Breakefield, X. O.; Snyder, E. Y., Neural stem cells display extensive tropism for pathology in adult brain: evidence from intracranial gliomas. *Proc Natl Acad Sci U S A* **2000,** 97, (23), 12846-51.

147. Wu, X.; Hu, J.; Zhou, L.; Mao, Y.; Yang, B.; Gao, L.; Xie, R.; Xu, F.; Zhang, D.; Liu, J.; Zhu, J., In vivo tracking of superparamagnetic iron oxide nanoparticle-labeled mesenchymal stem cell tropism to malignant gliomas using magnetic resonance imaging. Laboratory investigation. *J Neurosurg* **2008,** 108, (2), 320-9.

148. Tacken, P. J.; de Vries, I. J.; Torensma, R.; Figdor, C. G., Dendritic-cell immunotherapy: from ex vivo loading to in vivo targeting. *Nat Rev Immunol* **2007,** 7, (10), 790-802.

149. Mani, V.; Adler, E.; Briley-Saebo, K. C.; Bystrup, A.; Fuster, V.; Keller, G.; Fayad, Z. A., Serial in vivo positive contrast MRI of iron oxide-labeled embryonic stem cell-derived cardiac precursor cells in a mouse model of myocardial infarction. *Magn Reson Med* **2008,** 60, (1), 73-81.

150. Verdijk, P.; Scheenen, T. W.; Lesterhuis, W. J.; Gambarota, G.; Veltien, A. A.; Walczak, P.; Scharenborg, N. M.; Bulte, J. W.; Punt, C. J.; Heerschap, A.; Figdor, C. G.; de Vries, I. J., Sensitivity of magnetic resonance imaging of dendritic cells for in vivo tracking of cellular cancer vaccines. *Int J Cancer* **2007,** 120, (5), 978-84.

151. Dove, A., Cell-based therapies go live. *Nat Biotechnol* **2002,** 20, (4), 339-43.

152. Rosenberg, S. A.; Restifo, N. P.; Yang, J. C.; Morgan, R. A.; Dudley, M. E., Adoptive cell transfer: a clinical path to effective cancer immunotherapy. *Nat Rev Cancer* **2008,** 8, (4), 299-308.

153. Kircher, M. F.; Allport, J. R.; Graves, E. E.; Love, V.; Josephson, L.; Lichtman, A. H.; Weissleder, R., In vivo high resolution three-dimensional imaging of antigen-specific cytotoxic T-lymphocyte trafficking to tumors. *Cancer Res* **2003,** 63, (20), 6838-46.

154. Smirnov, P.; Lavergne, E.; Gazeau, F.; Lewin, M.; Boissonnas, A.; Doan, B. T.; Gillet, B.; Combadiere, C.; Combadiere, B.; Clement, O., In vivo cellular imaging of lymphocyte trafficking by MRI: a tumor model approach to cell-based anticancer therapy. *Magn Reson Med* **2006,** 56, (3), 498-508.

155. Melo, L. G.; Pachori, A. S.; Kong, D.; Gnecchi, M.; Wang, K.; Pratt, R. E.; Dzau, V. J., Molecular and cell-based therapies for protection, rescue, and repair of ischemic myocardium: reasons for cautious optimism. *Circulation* **2004,** 109, (20), 2386-93.

156. Arbab, A. S.; Frank, J. A., Cellular MRI and its role in stem cell therapy. *Regen Med* **2008,** 3, (2), 199-215.

157. Bulte, J. W.; Arbab, A. S.; Douglas, T.; Frank, J. A., Preparation of magnetically labeled cells for cell tracking by magnetic resonance imaging. *Methods Enzymol* **2004,** 386, 275-99.

158. Amsalem, Y.; Mardor, Y.; Feinberg, M. S.; Landa, N.; Miller, L.; Daniels, D.; Ocherashvilli, A.; Holbova, R.; Yosef, O.; Barbash, I. M.; Leor, J., Iron-oxide labeling and outcome of transplanted mesenchymal stem cells in the infarcted myocardium. *Circulation* **2007,** 116, (11 Suppl), I38-45.

159. Goldman, S., Stem and progenitor cell-based therapy of the human central nervous system. *Nat Biotechnol* **2005,** 23, (7), 862-71.

160. Bertuzzi, F.; Marzorati, S.; Secchi, A., Islet cell transplantation. *Curr Mol Med* **2006,** 6, (4), 369-74.

161. Evgenov, N. V.; Medarova, Z.; Dai, G.; Bonner-Weir, S.; Moore, A., In vivo imaging of islet transplantation. *Nat Med* **2006,** 12, (1), 144-8.

162. Fodor, W. L., Tissue engineering and cell based therapies, from the bench to the clinic: the potential to replace, repair and regenerate. *Reprod Biol Endocrinol* **2003,** 1, 102.

163. Bulte, J. W.; Kraitchman, D. L., Monitoring cell therapy using iron oxide MR contrast agents. *Curr Pharm Biotechnol* **2004,** 5, (6), 567-84.

164. de Vries, I. J.; Lesterhuis, W. J.; Barentsz, J. O.; Verdijk, P.; van Krieken, J. H.; Boerman, O. C.; Oyen, W. J.; Bonenkamp, J. J.; Boezeman, J. B.; Adema, G. J.; Bulte, J. W.; Scheenen, T. W.; Punt, C. J.; Heerschap, A.; Figdor, C. G., Magnetic resonance tracking of dendritic cells in melanoma patients for monitoring of cellular therapy. *Nat Biotechnol* **2005,** 23, (11), 1407-13.

165. Frank, J. A.; Miller, B. R.; Arbab, A. S.; Zywicke, H. A.; Jordan, E. K.; Lewis, B. K.; Bryant, L. H., Jr.; Bulte, J. W., Clinically applicable labeling of mammalian and stem cells by combining superparamagnetic iron oxides and transfection agents. *Radiology* **2003,** 228, (2), 480-7.

166. Montet-Abou, K.; Montet, X.; Weissleder, R.; Josephson, L., Transfection agent induced nanoparticle cell loading. *Mol Imaging* **2005,** 4, (3), 165-71.

167. Zhao, M.; Kircher, M. F.; Josephson, L.; Weissleder, R., Differential conjugation of tat peptide to superparamagnetic nanoparticles and its effect on cellular uptake. *Bioconjug Chem* **2002,** 13, (4), 840-4.

168. Bulte, J. W.; Brooks, R. A.; Moskowitz, B. M.; Bryant, L. H., Jr.; Frank, J. A., Relaxometry and magnetometry of the MR contrast agent MION-46L. *Magn Reson Med* **1999,** 42, (2), 379-84.

169. Arbab, A. S.; Yocum, G. T.; Wilson, L. B.; Parwana, A.; Jordan, E. K.; Kalish, H.; Frank, J. A., Comparison of transfection agents in forming complexes with ferumoxides, cell labeling efficiency, and cellular viability. *Mol Imaging* **2004,** 3, (1), 24-32.

170. Montet-Abou, K.; Montet, X.; Weissleder, R.; Josephson, L., Cell internalization of magnetic nanoparticles using transfection agents. *Mol Imaging* **2007,** 6, (1), 1-9.

171. Kostura, L.; Kraitchman, D. L.; Mackay, A. M.; Pittenger, M. F.; Bulte, J. W., Feridex labeling of mesenchymal stem cells inhibits chondrogenesis but not adipogenesis or osteogenesis. *NMR Biomed* **2004,** 17, (7), 513-7.

172. Arbab, A. S.; Jordan, E. K.; Wilson, L. B.; Yocum, G. T.; Lewis, B. K.; Frank, J. A., In vivo trafficking and targeted delivery of magnetically labeled stem cells. *Hum Gene Ther* **2004,** 15, (4), 351-60.

173. Sorgi, F. L.; Bhattacharya, S.; Huang, L., Protamine sulfate enhances lipid-mediated gene transfer. *Gene Ther* **1997,** 4, (9), 961-8.

174. Suzuki, T.; Futaki, S.; Niwa, M.; Tanaka, S.; Ueda, K.; Sugiura, Y., Possible existence of common internalization mechanisms among arginine-rich peptides. *Journal of Biological Chemistry* **2002,** 277, (4), 2437-2443.

175. Ter-Avetisyan, G.; Tuennemann, G.; Nowak, D.; Nitschke, M.; Herrmann, A.; Drab, M.; Cardoso, M. C., Cell Entry of Arginine-rich Peptides Is Independent of Endocytosis. *Journal of Biological Chemistry* **2009,** 284, (6), 3370-3378.

176. Ziegler, A., Thermodynamic studies and binding mechanisms of cell-penetrating peptides with lipids and glycosaminoglycans. *Advanced Drug Delivery Reviews* **2008,** 60, (4-5), 580-597.

177. Herce, H. D.; Garcia, A. E.; Litt, J.; Kane, R. S.; Martin, P.; Enrique, N.; Rebolledo, A.; Milesi, V., Arginine-Rich Peptides Destabilize the Plasma Membrane, Consistent with a Pore Formation Translocation Mechanism of Cell-Penetrating Peptides. *Biophysical Journal* **2009,** 97, (7), 1917-1925.

178. Hiller, S.; Leporatti, S.; Schnackel, A.; Typlt, E.; Donath, E., Protamine assembled in multilayers on colloidal particles can be exchanged and released. *Biomacromolecules* **2004,** 5, (4), 1580-7.

179. Heyn, C.; Ronald, J. A.; Ramadan, S. S.; Snir, J. A.; Barry, A. M.; MacKenzie, L. T.; Mikulis, D. J.; Palmieri, D.; Bronder, J. L.; Steeg, P. S.; Yoneda, T.; MacDonald, I. C.; Chambers, A. F.; Rutt, B. K.; Foster, P. J., In vivo MRI of cancer cell fate at the single-cell level

in a mouse model of breast cancer metastasis to the brain. *Magnetic Resonance in Medicine* **2006,** 56, (5), 1001-1010.

180. Wu, Y. J.; Muldoon, L. L.; Varallyay, C.; Markwardt, S.; Jones, R. E.; Neuwelt, E. A., In vivo leukocyte labeling with intravenous ferumoxides/protamine sulfate complex and in vitro characterization for cellular magnetic resonance imaging. *Am J Physiol Cell Physiol* **2007,** 293, (5), C1698-708.

ACKNOWLEDGMENTS

Thank you to everyone who made this work possible:

My thesis committee for their guidance and inspiration.

My parents, Tien and Chang-Lee Chen, for being the most supportive and amazing parents a person could possibly have. I could not even begin to describe how grateful I am to them.
My brother, Kevin Chen, for inspiring me with his talents, intelligence and success, all while maintaining a wicked sense of humor.

Mat Laibowitz for his love and support, for believing in me, and for being all-around super.

Hootan Farhat, Alfonso Reina Cecco, and Federico Villapando Paez for sharing beers and laughs and always keeping me grounded. We made it guys.

My dance family for providing creative physical release to balance long hours in the lab.

Joe Blois, Fred Reynolds, Elisenda Rodriguez, Martin Etzrodt, David Alcantara Parra, Virna Cortez-Remano, Andita Newton, Hushan Yuan, Jayeeta Bhaumik, Fangwei Shao, Elisabeth Garanger, and the other current and former members of CMIR who were not only generous with their scientific knowledge but also with their potlucks and friendships.

Grace Kim, Catherine Tweedie, and David Nguyen for their wise words, mentorship, and advice, and for somehow managing to be both great friends and great role models.

Victor Lelyveld and Liz Zhang for their imaging expertise.

Caroline Jones and the staff of the List Visual Arts Center for challenging and exercising a different part of my brain, allowing me to look at my research differently.

All of my other friends and family for their support and for all the good times. I look forward to many good times to come.